Award Number: W81XWH-12-2-0038

TITLE: Prevention of Blast-Related Injuries

PRINCIPAL INVESTIGATOR: Albert I. King

CONTRACTING ORGANIZATION: Wayne State University
Detroit, MI 48201

REPORT DATE: September 2017

TYPE OF REPORT: Final Report

PREPARED FOR: U.S. Army Medical Research and Materiel Command
                            Fort Detrick, Maryland 21702-5012

DISTRIBUTION STATEMENT: Approved for Public Release;
                                          Distribution Unlimited

REPORT DOCUMENTATION PAGE			*Form Approved* *OMB No. 0704-0188*
Public reporting burden for this collection of information is estimated to average 1 hour per response, including the time for reviewing instructions, searching existing data sources, gathering and maintaining the data needed, and completing and reviewing this collection of information. Send comments regarding this burden estimate or any other aspect of this collection of information, including suggestions for reducing this burden to Department of Defense, Washington Headquarters Services, Directorate for Information Operations and Reports (0704-0188), 1215 Jefferson Davis Highway, Suite 1204, Arlington, VA 22202-4302. Respondents should be aware that notwithstanding any other provision of law, no person shall be subject to any penalty for failing to comply with a collection of information if it does not display a currently valid OMB control number. **PLEASE DO NOT RETURN YOUR FORM TO THE ABOVE ADDRESS.**			
1. REPORT DATE September 2017	**2. REPORT TYPE** Final		**3. DATES COVERED** 15 June 2012 - 30 June 2017
4. TITLE AND SUBTITLE Prevention of Blast-Related Injuries			**5a. CONTRACT NUMBER**
			5b. GRANT NUMBER W81XWH-12-2-0038
			5c. PROGRAM ELEMENT NUMBER
6. AUTHOR(S) Albert King, John Cavanaugh, King Yang, Liying Zhang, Xin Jin E-Mail: king@eng.wayne.edu			**5d. PROJECT NUMBER**
			5e. TASK NUMBER
			5f. WORK UNIT NUMBER
7. PERFORMING ORGANIZATION NAME(S) AND ADDRESS(ES) Wayne State University 5700 Cass Ave., Suite 4900 Detroit, MI 48202-3692			**8. PERFORMING ORGANIZATION REPORT**
9. SPONSORING / MONITORING **AGENCY NAME(S) AND ADDRESS(ES)** U.S. Army Medical Research and Materiel Command Fort Detrick, Maryland 21702-5012			**10. SPONSOR/MONITOR'S ACRONYM(S)**
			11. SPONSOR/MONITOR'S REPORT NUMBER(S)
12. DISTRIBUTION / AVAILABILITY STATEMENT Approved for Public Release; Distribution Unlimited			
13. SUPPLEMENTARY NOTES			

14. ABSTRACT

This report covers work done on blast testing of live anesthetized swine and on unembalmed cadavers. A detailed histological study of blast-exposed swine brain showed that there was damage to both the axons and the neuron cell bodies in the form β-APP immunoreactivity and other tests, suggesting that the mechanism of injury may be different from that of blunt impact. We have also developed computer models of the swine and human brain and have partially validated them against the acquired experimental data. It is proposed that future research concentrate on seeking injury mechanisms to brain cells caused by a pressure wave.

15. SUBJECT TERMS

Keywords: Blast-related brain injury, Open field testing of swine and PMHS, Computer modeling of swine and human brain, brain injury mechanisms

16. SECURITY CLASSIFICATION OF:			**17. LIMITATION OF ABSTRACT**	**18. NUMBER OF PAGES**	**19a. NAME OF RESPONSIBLE PERSON** USAMRMC
a. REPORT U	**b. ABSTRACT** U	**c. THIS PAGE** U	U	116	**19b. TELEPHONE NUMBER** (include area code)

TABLE OF CONTENTS

INTRODUCTION

This research project is designed to determine if primary blast wave can cause mild traumatic brain injury and, if possible, to determine the cause(s) of mild traumatic brain injury due to blast overpressure. It consists of an experimental portion in which 12 swine and 6 post-mortem human subjects (PMHS) are to be exposed to blast. The experimental effort is supplemented by a computer modeling section which can extend the results of the tests to blast scenarios not easily achievable experimentally. In this report, we report the completion of our swine and PMHS testing and results of our histological findings in the swine brains. We have also completed our modeling effort to simulate the response of the swine and human brain to blast overpressure and have provided evidence of the validity of the models by comparing model results with the experimental data that were acquired under this project.

STATEMENT OF WORK

The Statement of Work (SOW) for this project is as follows:

I.   Perform open field blast testing on 6 anesthetized minipigs to obtain biomechanical data and on 12 anesthetized minipigs to obtain pathohistological data
II.   Perform open field blast testing on 6 unembalmed post-mortem human subjects (PMHS) also known as cadavers to obtain biomechanical data
III. Develop and validate a computer model of the pig brain simulating the effects of a blast over-pressure
IV.   Develop and validate a computer model of the human brain simulating the effects of a blast over-pressure

Each task is a separate report with its own figures, tables and list of references.

TASK I REPORT

Task I - Perform open field blast testing on 6 anesthetized minipigs to obtain biomechanical data and on 12 anesthetized minipigs to obtain pathohistological data

In this task, there were three separate work items:

1. Blast testing of instrumented swine to characterize the biomechanical responses of the swine brain subjected to free-field blasts;
2. Blast testing of non-instrumented swine to determine the extent of brain injury using histological methods
3. Correlation of results between biomechanical responses and histological findings.

1   Blast Testing of Instrumented Swine

a)   Summary of Test Methodology

It should be mentioned at the outset that the research protocol used in this project was reviewed and approved by both the Institutional Animal Care and Use Committee (IACUC) of Wayne State University and the USAMRMC Animal Care and Use Research Office (ACURO). Yucatan swine aged 6-8 months and weighing 50 to 60 kg were used. All swine were acclimated to their new housing conditions for 6-8 days prior to testing. An ambulance was used to transport the animal to the test site while it was under anesthesia (ketamine 20mg/kg and xylazine 2mg/kg, both administered intramuscularly).

The principal biomechanical parameter of interest is the intracranial pressure in an anesthetized swine developed in the brain due to blast. Before conducting the free-field testing, techniques for the installation of miniature pressure sensors into the brain were developed using an expired swine, subjected to blast in a laboratory shock tube. The location of the brain in the swine head is shown in Figure 1. Incisions in the scalp at anterior-superior and posterior regions were made to expose the skull. Small holes, 1/4 inch in diameter, were made in the frontal bone, on the anterior portion of the parietal bone (P) at the midline, and on the occipital bone 1 cm from the midline (Figure 2A). The holes were drilled using a drill bit with a stop collar. The length of drill bit going through the skull was 8 mm for the parietal bone, 15 mm for occipital bone and 10 mm for the frontal bone. A tapered cutting thread was used to make threads in the holes. A 1/4-inch diameter threaded copper hollow fitting, equipped with a threaded cap (Dorman, Colmar, PA) was screwed into each threaded hole. Then a cannula 1/8 inch in diameter was inserted into the brain to guide the pressure sensor into location. The pressure sensor cable passed through a rubber ring in which there was a hole of the same diameter as that of the Kulite pressure sensor cable. The rubber ring was placed between the fitting and its cap. By tightening cap onto the fitting, the hole was sealed by the rubber ring.

Figure 1. Anatomy of a   Figure 2 (A) Location of screws installed
swine brain   (B) Screws installed with pressure transducers

Additional biomechanical data were obtained by installing an accelerometer package on the occipital bone of the skull. The package consisted of a triaxial linear accelerometer and a set of triaxial angular velocity or rate sensors. Strain in the skull was measured by four sets of strain gauge rosettes, two mounted on the frontal bone and the other two on the occipital bone. The installation procedure is shown in Figure 3A while the locations of the strain gauge rosettes are shown in Figure 3B. The locations of the Kulite pressure sensors are shown in Figure 4.
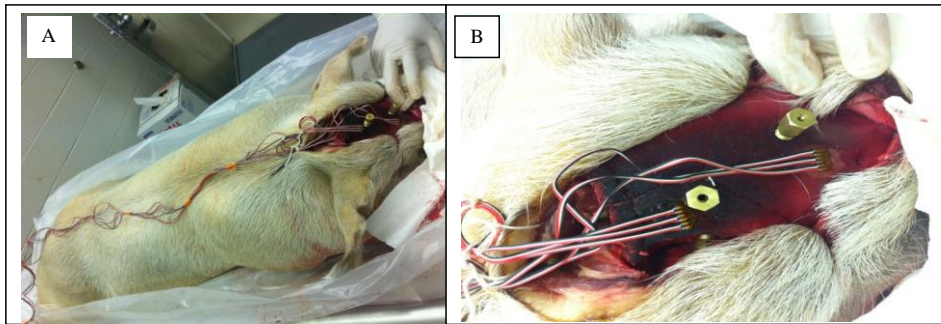

Figure 3. (A) Installation of strain gauges and pressure sensors. (B) Location of strain gauges on the skull.
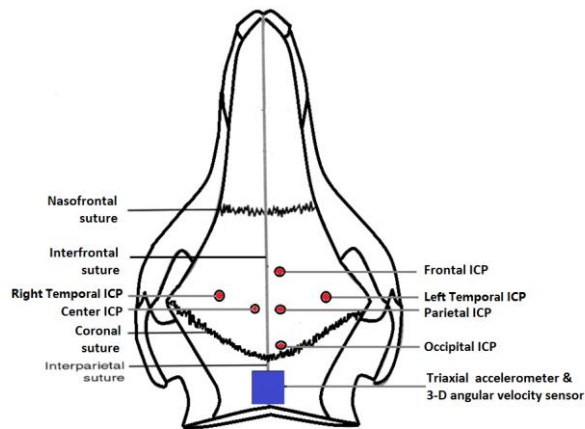
Figure 4. Top view of the location of ICP sensors relative to the skull of the swine

Data from all sensors were sent through a DEWETRON data acquisition which conditioned and digitized data in real time. Since the shock tube tests were successful, open field blast tests were carried out in Port Clinton, OH, at the facilities of ARES, Inc. This site is approximately 90 miles from the Wayne State University campus. Its area is about 30 m square with a concrete surface. A typical test set-up is depicted in Figure 5. In this figure, the swine is being exposed to a frontal blast as the 3.6 kg of C4 explosive. is to the left, denoted by (A). Pencil transducers (B) were used to measure the incident overpressure (IOP). The head of the animal is denoted by (C) and the location of high speed cameras is denoted by (D). The swine was placed in a lead-covered sling, hanging from a metal bean which was attached to two A-frames

Figure 5. Experimental test setup for a frontal blast test (See text for explanation of the items identified by the letters (A) through (D).

We have completed open field blast testing of six anesthetized swine to obtain biomechanical data of brain response due to blast overpressure. Data from one animal were lost due to malfunction of the DEWETRON data acquisition system. The target incident overpressures (IOP) were nominally 150 kPa (low), 300 kPa (medium) and 450 kPa (high). The range for the nominal low level blasts (150 kPa) was between 148 kPa to 161 kPa; while that for the nominal medium level blasts (300 kPa) was between 218 kPa to 341 kPa; and that for the nominal high level blasts (450 kPa) was between 341 kPa to 552 kPa. Within each group, the pig head was oriented to the blast wave in three different directions: front and rear, or side. A detailed analysis was conducted on the mechanical data from frontal blasts. All the data were grouped into three incident overpressure levels according to recorded incident pressure by the pencil transducer located next to the head of the swine.

(b) Frontal blast data analysis: We have completed analysis of the frontal blast data and have published a paper in Frontiers in Neurology (Ke et al, 2016), reporting on 19 frontal blast tests on five swine. Plots of a typical set of IOP and ICP curves are shown in Figure 6. The peak IOP, duration, and IOP impulse of each test are summarized in

Table 1. Baseline noise was filtered out but the pressure data retained at least 90% of their original values. In our study, peak IOPs ranged from 143 to 461 kPa. The impulses ranged from 156 to 239 Pa-s. The test results were then divided into three pressure level groups based on the IOP results (Table 2). The average peak IOP values were 149, 279, and 409 kPa for the low, medium, and high blast levels respectively. The average peak ICP at various locations of the brain were in the range of 79-144 kPa at the low blast level, 209-282 kPa at the medium blast level, and 312-415 kPa at the high blast level.
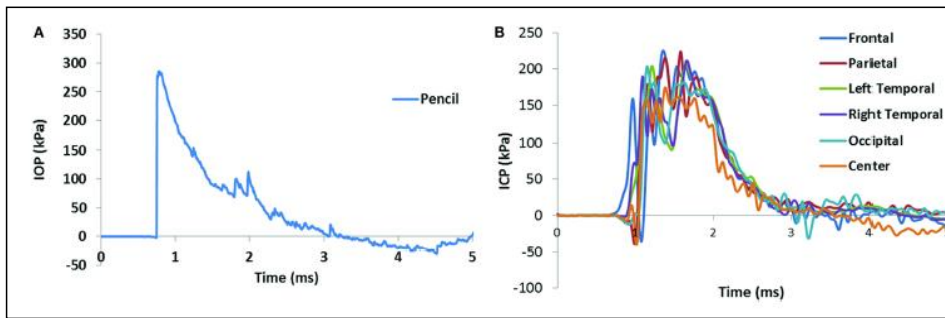

Figure 6. (A) Incident over pressure (IOP) as measured by a pencil transducer (B) Intracranial pressures due to the IOP in (A).

Table 1. IOP peaks, durations and impulses for the 19 frontal exposures

Test ID	Peak incident pressure (kPa)	Duration (ms)	Impulse (Pa s)
1[a]	150.3	2.8	170.3
2[a]	142.7	2.9	155.7
3	150.3	2.9	158.3
4	148.2	2.9	160.3
5	152.4	3.1	161.0
6	218.0	2.1	193.9
7	253.4	2.2	195.7
8	255.2	2.0	194.9
9	324.2	2.3	194.1
10[a]	285.5	2.3	207.7
11[a]	284.1	2.1	198.1
12	285.4	2.0	196.4
13	325.4	2.0	204.0
14	366.0	1.6	205.4
15[a]	441.3	1.7	225.2
16[a]	413.7	1.6	229.6
17[a]	460.6	1.7	239.2
18[a]	341.3	2.4	228.8
19	432.3	2.4	222.9

[a]Indicates tests in which swine had already expired during testing.

Table 2. ICP peaks generated by three levels of IOP

Test	Biomechanical responses, ICP peak values, mean $\pm$ SE						
	IOP	Frontal	Parietal	Left temp	Right temp	Occipital	Center
Low	148.8 ± 1.7	97.6 ± 19.7	144.2 ± 18.0	142.8 ± 0.0	147.9 ± 0.0	78.9 ± 13.4	93.7 ± 17.0
Medium	278.9 ± 13.9	236.5 ± 30.7	276.0 ± 62.4	281.6 ± 35.0	253.1 ± 46.8	209.1 ± 34.5	228.1 ± 29.5
High	409.2 ± 18.9	311.7 ± 29.1	414.6 ± 0.0	386.4 ± 7.1	325.5 ± 8.6	328.2 ± 26.7	327.2 ± 17.0

Scatter plots show that peak ICPs increased with peak IOP at every instrumented location (Figure 7). More specifically, ICP peak values correlated well with peak IOP in all the three blast pressure levels using linear regression models. The overall ICP responses were close or lower than its IOP at each blast level. This result is not unreasonable because the sensors were not at the brain/skull junction where the ICP is expected to be higher due to impedance mismatch. At the low blast level, peak ICP

10

responses in the occipital and center regions were significantly lower than the peak IOPs (paired *t-test, p < 0.05*), with no significant differences in other regions of the brain (paired *t-test*, p > 0.05). At the medium blast level, no significant difference was found between peak ICP responses and peak IOP (paired *t-test, p > 0.05*). At the high blast level, peak, the ICPs were not significantly different from the peak IOPs (paired *t-test, p > 0.05*), except that in the center regions where the peak ICPs were significantly lower compared with the peak IOPs (paired *t-test, p < 0.05*) (Figure 8). This means that ICP drops as it traverses the brain but the drop is not significant. There was no statistically significance difference in peak ICPs between various locations at the low, medium and high levels (ANOVA, *p > 0.05*). The frontal ICP at the low blast level was significantly lower than that at the medium and the high blast level (ANOVA, PostHoc LSD, *p < 0.05*). However, there was no significant difference of the peak frontal ICPs between the medium and the high blast level (ANOVA, PostHoc LSD, *p > 0.05*). Similarly, the occipital ICP at the low blast level was lower than that at the medium and the high blast level (ANOVA, PostHoc LSD, *p < 0.05*). For the occipital ICPs, no significant difference was found between the medium and high blast levels (ANOVA,
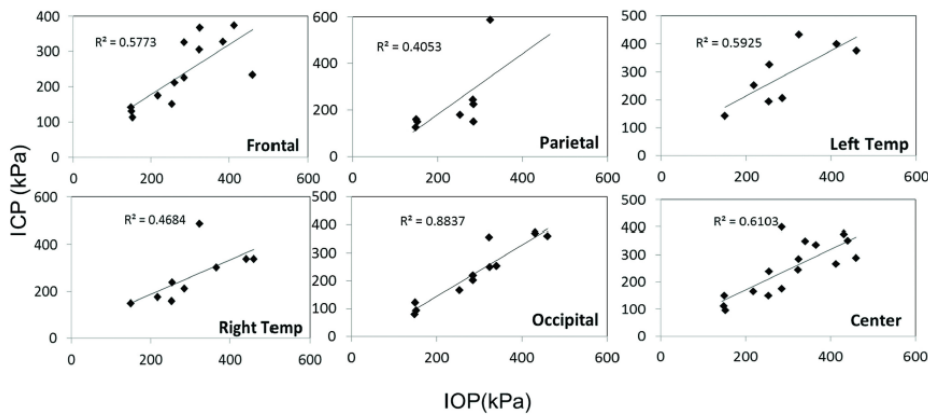

Figure 7. Scatter plots of ICP vs. IOP at different locations of the brain. The abscissa is the IO and the ordinate is the ICP. The units of pressure are kPa. A linear regression model and R^2 values are shown in each plot.
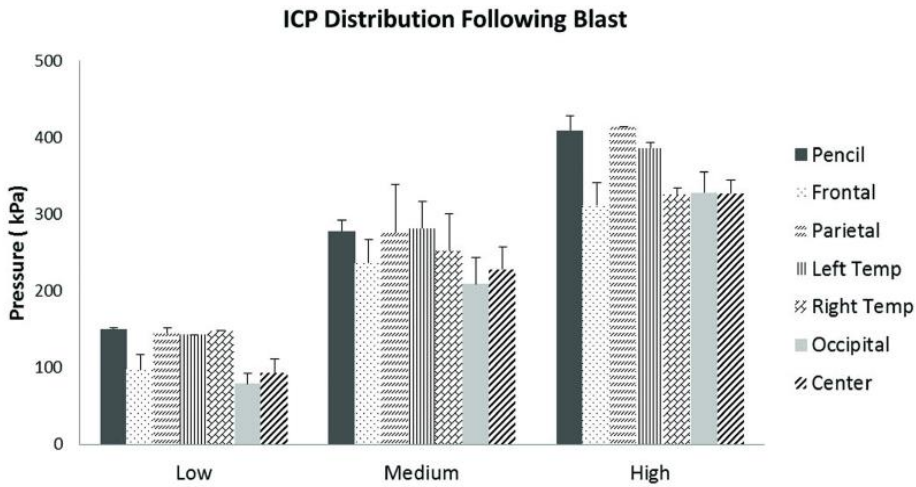
ICP Distribution Following Blast

Figure 8. Peak ICP values at different blast levels. Peak ICP's in different regions of the brain were not statistically different from each other.'
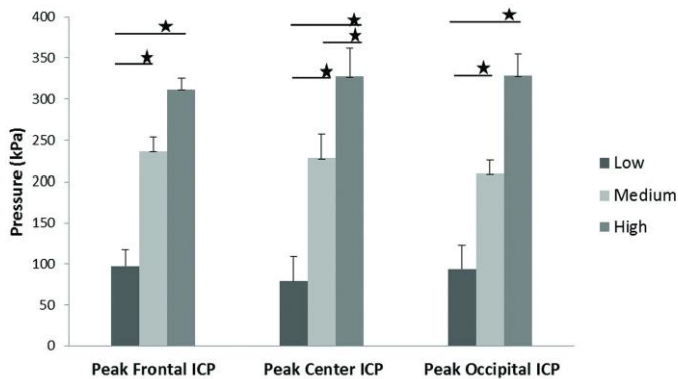

Figure 9. ICP peak values in the frontal, central and occipital regions of the brain show a significant increase with increasing blast levels. Student's t-tests showed a significant difference between blast levels (* $p < 0.05$) PostHoc LSD, $p > 0.05$).

The peak center ICP values at the medium and the high blast levels were both significantly higher than that at the low blast level (ANOVA, PostHoc LSD, $p < 0.05$). Statistical analysis also showed significant differences in the peak ICP between the medium and the high blast levels (ANOVA, PostHoc LSD, $p < 0.05$) (Figure 9), indicating that changes in the ICP are larger at higher IOP levels.
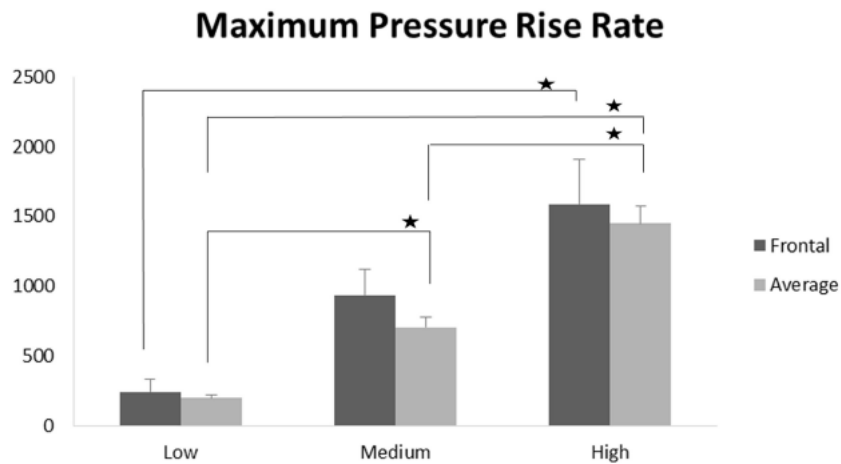
Maximum Pressure Rise Rate

Figure 10. Maximum pressure rise rates were significantly increased with increasing blast levels, both in the frontal region and when averaged across all five locations (* $p < 0.05$).

The average maximum pressure rise rate increased significantly with blast levels. A similar trend was observed in the frontal region where the maximum pressure rise rates were higher (Figure 10). That is, the pressure rise rate is a function of the magnitude of the pressure and this observation should be relatable to the observed injuries in the brain. Average peak ICP peak values in each test correlated well with peak IOPs. Average ICP impulses of each test were also correlated with IOP impulses (Figures 11A and B).
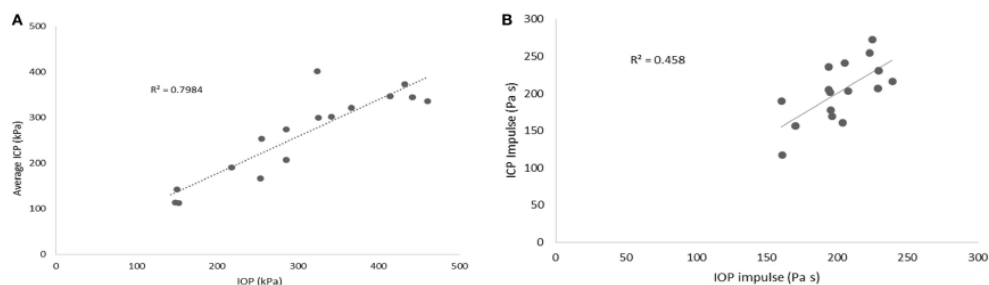

Figure 11. (A) Scatter plot of average ICP peak values at different locations vs. IOP. (B) Average ICP impulse at different locations vs. IOP impulse.

Head kinematics

In this study, we characterized the head motion with its linear acceleration and angular velocity. Typical histories of the three linear accelerometers and the three angular rate sensors are shown in Figures 12A and 12B respectively. The resultant linear accelerations and the resultant angular velocities increased linearly with peak IOP (Figures 13A and B). They were also well correlated with IOP impulses (Figures 13C and D).
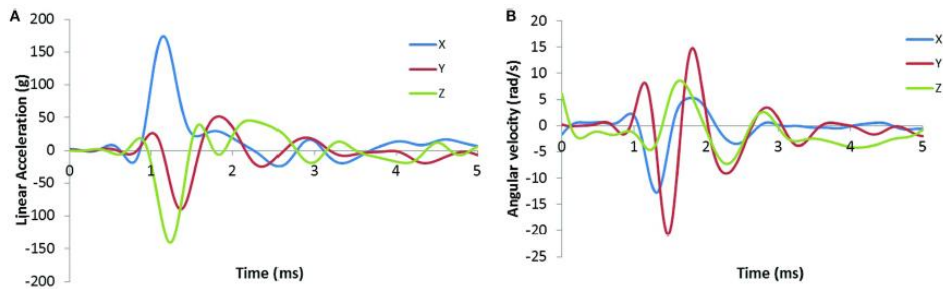

Figure 12. Typical time-history plots of linear acceleration (A) and angular velocity (B) of the swine head. The positive x-axis is directed frontally and the positive z-axis is directed vertically upward while the positive y-axis is directed horizontally to the right
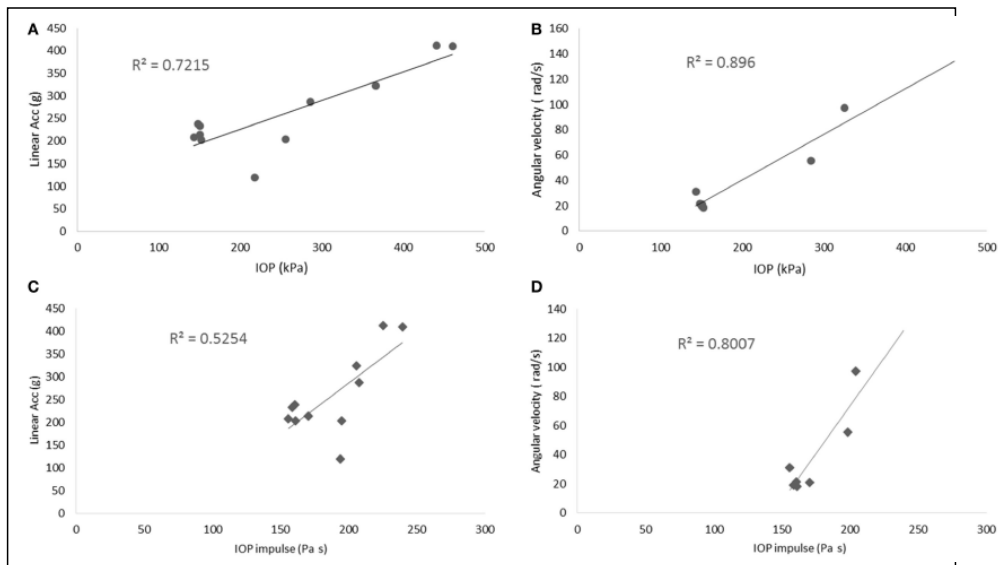
14

Figure 13. Scatter plots of head motion. The relationship of linear acceleration and angular velocity with peak IOP are shown in (A) and (B) respectively. Similarly, their relationship with IOP impulse are shown in (C) and (D) respectively.

The resultant accelerations at high blast levels were significantly higher than those at the low and medium blast levels (ANOVA, PostHoc LSD, $p < 0.05$), but there was no statistical significance between the low and the medium blast levels (ANOVA, PostHoc LSD, $p > 0.05$). The resultant angular velocity at the medium blast level was significantly higher than that at the low blast level (independent t-test, $p < 0.05$). Here again, there is a non-linear relationship between IOP and head response which increases in severity as the IOP increases. This is a factor that needs to be considered in the design of protective gear. It may not be possible to protect those in extreme environments. The durations of the linear acceleration were typically less than 3 ms, indicating that there was little translational movement of the head during primary blast. Figure 14 shows the relationship between head motion and the ICP. The arrival of the ICP is almost simultaneous with head motion. That is, head motion is due to the primary wave. The blast wind arrived at 7.5 ms and caused a slight increase in linear acceleration and angular velocity but the magnitudes were much lower than those due to primary blast;

15
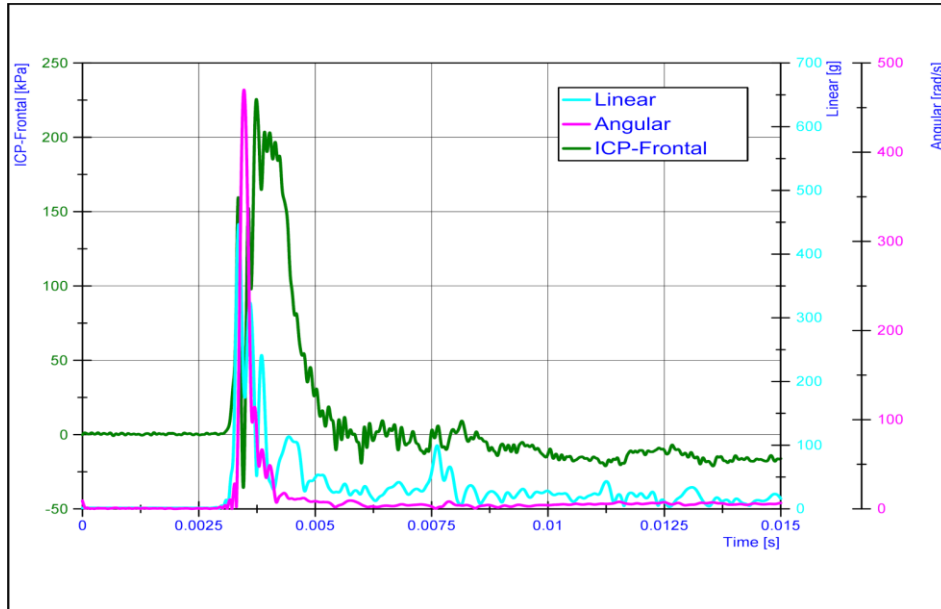
Figure 14. Relationship between ICP and head motion (head linear acceleration and angular velocity) demonstrates that primary blat imparts a severe acceleration to the head, albeit the duration is very short.

(c) Rear Blast Data Analysis:

In rear blasts, ICPs at different brain regions increased with increases in IOP with some exceptions at center brain region, as shown in Figure 15. ICP readings in the parietal region had the highest values among all the measured ICPs. The sensor located in this region was the closet one to the blast while frontal sensor was at the contrecoup location relative to the rear blast, but there was no evidence of a contrecoup pressure occurring there.
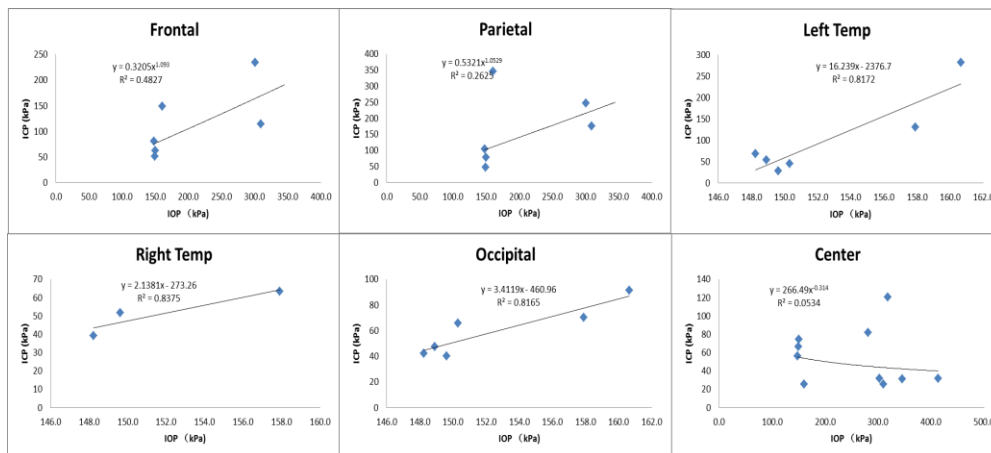
Figure 15. Scatter plots of ICP vs. IOP at different locations of the brain for rear blast tests. Linear regression model and R^2 values are shown in each plot.

Resultant linear head accelerations increased with increases in IOP in rear blast exposure of the head. Similar trends were also observed in resultant angular velocities of the head (Figure 16).
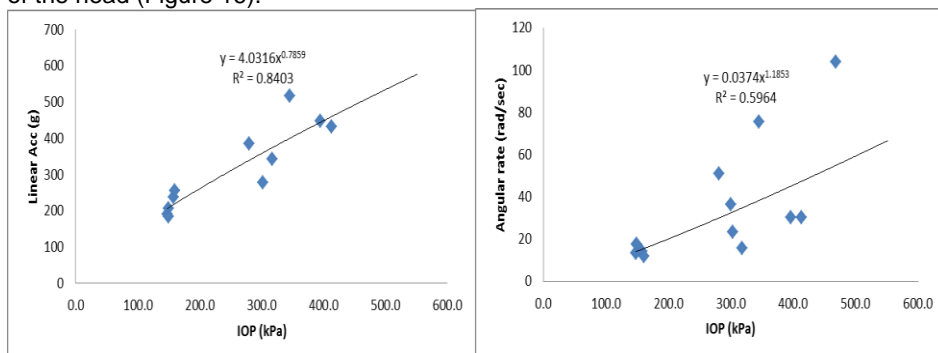
Figure 16. Scatter plots of the motion on the head in rear blasts. Resultant linear acceleration correlated well with peak IOP in a linear regression model; resultant angular velocity was minimally correlated with peak IOP in a linear regression model.

(d) Side Blast Data Analysis:

In side blast, IOP at left temporal region is in the coup location while the sensor in the right temporal region is at the contrecoup location of the blast. There was less correlation shown between peak IOP and peak ICP data (Figure 17). In some locations of the brain, the sensor readings were significantly different from each other at the

17

same blast level. This may be due to the changes made in the sensor arrays in 2014 and the exact cause is being investigated. Resultant linear and angular motions of the head were highly consistent with the IOP levels in side blasts (Figure 18).
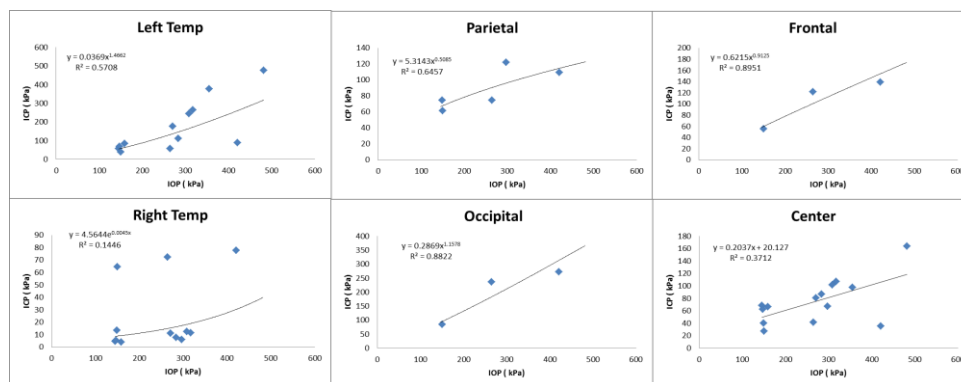
Figure 17. IOP vs. ICP at various regions of the brain in side blasts
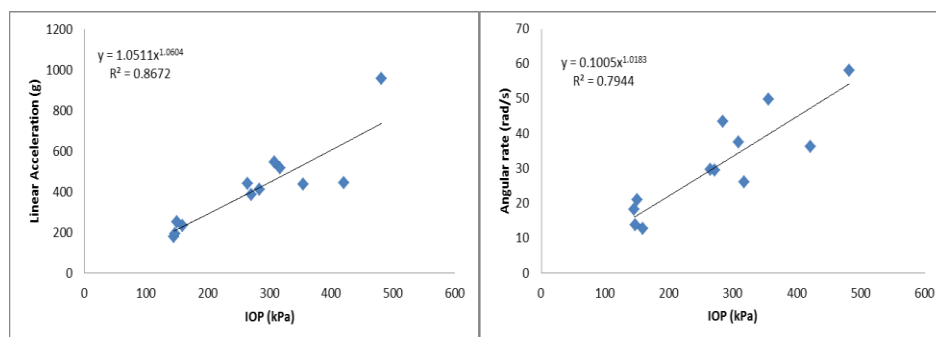
Figure 18. Relationship between ICP and head motion in side blasts (head linear acceleration and angular velocity) demonstrates that primary blast imparts a high acceleration to the head although the duration is short.

(e) Quantitative electroencephalography in a swine model of blast-induced brain injury

Electroencephalography (EEG) is a commonly used method to study cerebral function. EEG is particularly attractive for field use because the recording device is portable, relatively inexpensive and requires relatively short recording durations [1]. Analysis of EEG data is usually performed qualitatively and routine EEG lacks sufficient sensitivity and specificity for diagnosing mTBI [2-4]. Quantitative analysis of EEG data reduces the amount of data to be recorded and produces results that are readily interpreted [5]. Quantitative EEG (qEEG), together with advanced analyses methods, shows promise

for clinical applications. qEEG has been reported to be sensitive in the diagnosis of mild traumatic brain injury (mTBI) in the civilian setting and consistently yielded interesting research results in studies of concussed athletes and patients with mTBI [4, 6, 7-9], suggesting that qEEG measures can detect brain changes both early after sustaining mTBI and over a period of time post-injury. Among patients with mTBI at chronic phase, qEEG detection of mild TBI showed a sensitivity of 96.59% with a specificity of 89.15% [6]. However, most qEEG studies have evaluated individuals from civilian settings and individuals who have not been exposed to blast forces. Only a few peer-reviewed studies have examined EEG-recorded brain activity following blast-related injury among soldiers [10, 11], and these did not investigate brain activity in the early acute phase [10-12]. A few animal blast studies found waveform amplitude changes using routine EEG without showing diagnostic values [13, 14], however, these data are not sufficient to support the widespread clinical use of qEEG to diagnose blast-related mTBI. Early detection of blast-induced brain injury would allow early screening and assessment of brain abnormality in soldiers to enable timely therapeutic intervention.

The current study reports on the use of qEEG in blast-induced brain injury using a swine model. The purposes are to determine if qEEG can detect brain activity abnormalities early after blast exposure, to develop qEEG data analysis protocols, and to determine the parameters that are of most interest in assessing the neuronal effects of blast exposure.

Methods

EEG recording was performed at 15 min before blast, and 15, 30, 120 min, 1, 2, and 3 days post-blast using a Biopac data acquisition system (MP-36, Biopac, Goleta, CA). Non-invasive surface recording electrodes (Model# 502, Biopac, Goleta, CA) were placed on the skin over both frontal and parietal areas of the skull (Figure 19). Acknowledge software (Version 4.2, Biopac, Goleta, CA) was used for EEG data analysis. Raw EEG data was extracted into different bands including alpha-, beta-, theta-, delta-, gamma-bands. EEG parameters included over all frequency analysis and root mean square (RMS) analysis of alpha band using tools provided by Acknowledge software. Power of analysis (V^2/Hz/Min) of raw data and individual bands were analyzed and compared between pre-blast and post-blast using power spectral density (PSD) function in the software.

Experimental protocol:
Six swine were exposed to blast overpressure with a peak ranging from 420-450 kPa. All tests were performed in an open field test facility of ARES. Inc. The anesthetized swine was positioned 3.2 m from the center of the blast which was generated by 3.6 kg of C4 charge. The pressure levels measured at the head of the swine were 420-450 kPa at the location of the head of the swine. The swine wore a protective foam-lined lead vest that protected the torso from physical injury.

qEEG analysis

A personal computer system was used for the recording of the EEG signal using a Biopac data acquisition system, at 0.53–70 Hz (−3 dB) and a sensitivity of 70 μV/ms. Four pairs of non-invasive surface recording electrodes (model #502 of electrodes, with a diameter of 35 mm) were placed on the skin at the locations corresponding to C3, C4, P3, P4 with a common ground placed at the front of the head (Figure 19) [15]. Offline qEEG analysis was performed using Acknowledge software (Version 4.2, Biopac, Goleta, CA).
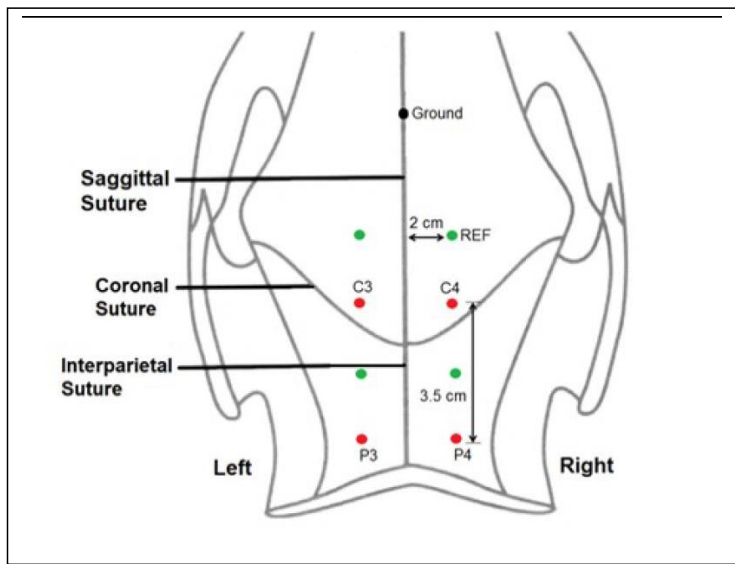
Figure 19. Position of the EEG electrodes is related to the crossing of coronal and sagittal sutures (bregma point). Nomenclature of electrodes (C_3, C_4, P_3, P_4) corresponds with the international 10–20 system, distances are adapted to fit the swine skull.

EEG signals were bandpass filtered using a zero-phase 6th order Butterworth filter with cut-off frequencies 0.5 and 30 Hz. A Hamming window was applied before performing a fast Fourier transform of each EEG epoch (2 s of EEG, using Welch's method) [15]. EEG parameters including frequency, root mean square (RMS) of the alpha band, and the power (V^2/Hz/Min) of the delta, theta, alpha, and beta bands were analyzed to determine the changes pre-blast and post-blast and at different recording locations. The qEEG parameters of mean amplitude (MAMP), and 90% spectral edge frequency (SEF90) were also calculated.

MAMP was calculated for each epoch by averaging the mean of the absolute value of the EEG from each channel using Fast Fourier Transform (FFT) function. The estimate of the power spectral density was calculated using Welch's method with an epoch length of 2 s and 25% overlap resulting in a spectral resolution of 0.5 Hz. SEF90 was calculated as the frequency below which 90% of the power between 0.5 and 20 Hz was contained [16].

Statistical analysis

SPSS 17.0 (SPSS Inc., Chicago, IL) software was used for data analysis. Significance of differences between recording locations and time points was analyzed using general linear model (GLM) univariate analysis and LSD was used in PostHoc analysis. Paired t tests were performed for selected two time points between the pre-blast versus a post-blast time point. Paired t-tests were used when LSD analysis demonstrated a *p* value slightly greater than 0.05. *P*<0.05 was considered as a significant difference.

Results

qEEG analysis showed that the power (V^2/Hz) of delta band increased significantly at the 15-minute post-blast time point recorded at left and right parietal locations (GLM univariate, PostHoc LSD, p=0.027) (Figure 20), the delta band power appeared to return to the baseline (the pre-blast level) at 30 minutes after blast and later on at various recording locations. Compared with pre-blast time point, delta band power increased significantly at the 15th minute after blast at P_3 and P_4 locations. Delta band power also increased at the 30th minute and 120th minute at the right central location (C_4) after blast, as well as 15th and 120th minute at the left central location (C_3) (Paired t test, p<0.05) (Figure 20). The power of other bands including alpha, beta, theta bands only increased slightly after blast without statistical significance (GLM univariate, PostHoc LSD, p>0.5).
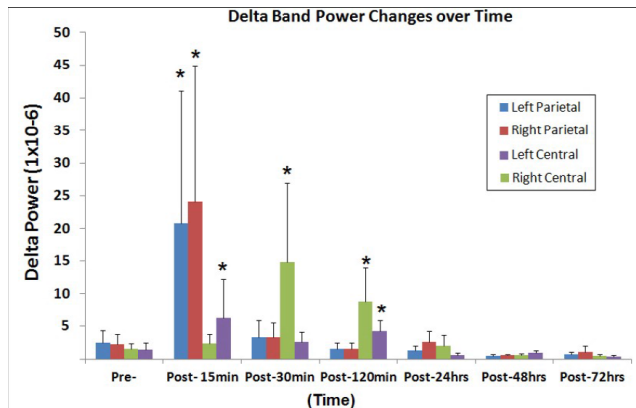
Figure 20 shows the delta band power recorded at different time points and 4 locations from the skull surface. Delta band power (Mean ±SD) increased significantly 15 minutes after blast at left and right parietal (P_3 and P_4) locations (GLM univariate, PostHoc LSD, $p < 0.05$, pre-injury versus 30th minute, asterisk *), 30th minute and 120th minute after blast at right central location (C_4) (Paired t tests, $p < 0.05$, versus pre-injury, stars) and 15th and 120th minute at the left central location (C_3) (Paired t tests, $p < 0.05$, versus pre-injury, stars).
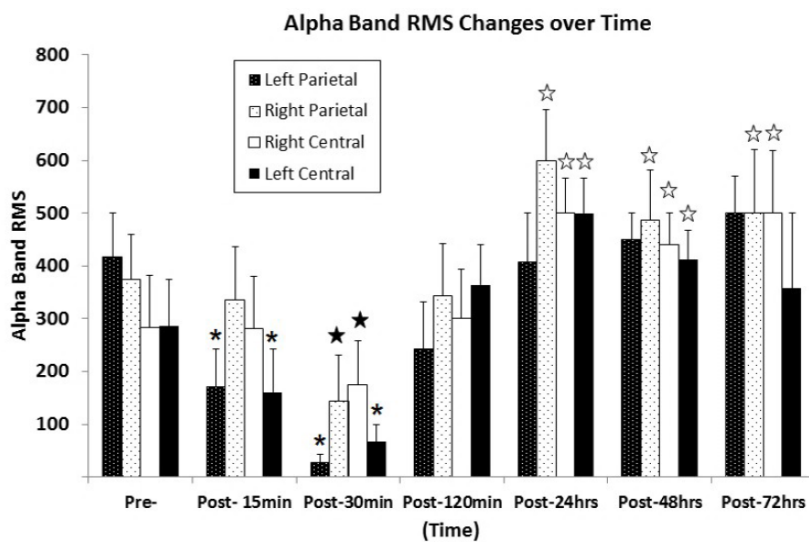
Figure 21 shows the alpha band root mean square (RMS) recorded at different locations and time points. Alpha band RMS (Mean ±SD) decreased after blast at the 15th minute (GLM univariate, postHoc LSD, $p < 0.05$, versus pre-injury, asterisk*) and

30th minute at left parietal and left central locations (GLM univariate, postHoc LSD, p<0.01, versus pre-injury, asterisk *), as well as at right parietal and right central locations at the 30th minute (Paired t test, p<0.05, versus pre-injury, stars). Alpha band RMS increased 24 hours after blast at some recording locations compared with pre-blast time point, Paired t test, p<0.05, versus pre-injury, hollow stars). Hollow stars indicate significant increase of alpha RMS, black stars indicate significant decrease of alpha RMS.

MAMP appeared to decrease at the time points of the 15th minute (GLM univariate, PostHoc, LSD, p=0.06), 24th hour (GLM univariate, postHoc, p=0.08), 48th hour (GLM univariate, postHoc, p=0.07) and the 72nd hour (p=0.13) post-blast (Figure 22), demonstrating that MAMP decreased after blast except for the time point of the 30th minute. Two time point comparison between pre- and post-blast showed statistical differences (Paired t test, p<0.05).

The spectral edge frequency at 90% margin (SEF_{90}) decreased significantly the 15th minute (GLM univariate, PostHoc LSD, p=0.02) and the 48th hour (GLM univariate, PostHoc LSD, p=0.01) after blast (Figure 23), indicative of power spectrum density shift to the left (low frequency domain). SEF90 also decreased at different locations and post-blast times compared to the pre-blast level (Paired t test, p<0.05).
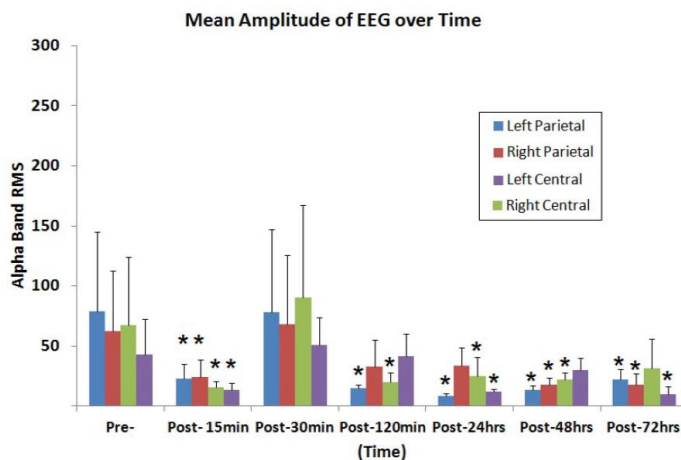

Figure 22 shows the mean amplitude (MAMP) (Mean ±SD) of EEG raw data recorded at different time points. Compared with pre-blast, MAMP decreased after blast except for the time point of the 30th minute time point (Paired t test, p<0.05, versus pre-injury, stars).

90% Spectral Edge Frequency Changes over Time
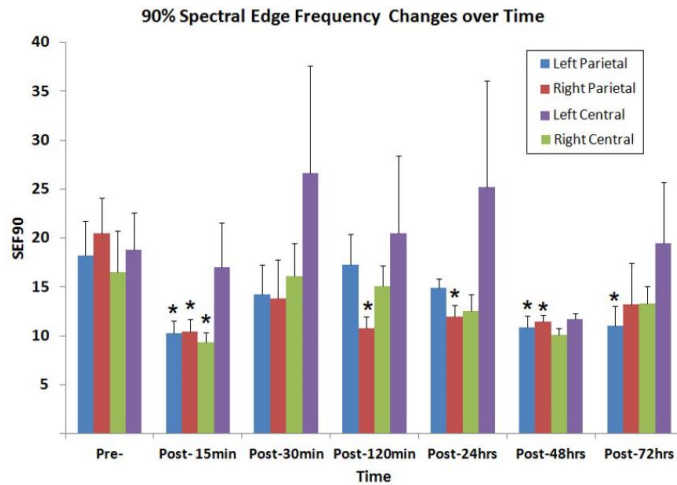
Figure 23 shows the spectral edge frequency at 90% margin (SEF_{90}) (Mean ±SD) recorded at different locations and time points. SEF_{90} decreased significantly in 15 minutes (GLM univariate, postHoc LSD, $p<0.05$, asterisk*) and other time points at different locations after blast (Paired t test, $p<0.05$, stars).

(f) Discussion

In this study, we chose the Yucatan pig as their body mass and skull thickness are closer to those of the human than small animals. Also, with a larger animal, biological tolerance level of air-filled organs to blast is believed to be higher.

This study exposed live swine subjects to free-field blast loading at various pressures and durations by changing the standoff distance between the charge and the swine. Of the six swine tested, data from one swine were lost due to equipment failure, two expired just before the blast testing, and one died during the tests. This resulted in 8 of the 19 blasts being performed on expired animals. However, the ICP responses showed little difference between expired animals and live animals. The potential causes of death could be related to complications from anesthesia and surgical procedure to insert ICP sensors. Additionally, a parallel group of non-instrumented animals were subjected to a single blast exposure (range 222 kPa-403 kPa). Observation of the brain harvested after perfusion performed after 3 days of survival showed no gross injury. Initial histological results from the frontal sections of the blast showed evidence of neuronal injury in the form of beta amyloid precursor protein immunoreactive zones in the gray and white matter. Neuronal injury was also supported by neurofilament light chain immunohistochemistry. Furthermore, an obvious increase in the number of astrocytes and microglia was also observed in the blast exposed sections compared to

sham sections. We hypothesize that there is direct correlation between ICP and brain injuries. Our histological studies will be testing this hypothesis.

We analyzed the ICP in different regions of the brain at various blast IOP levels. All previous studies have addressed the mechanical responses of the brain to blast with post-mortem human subjects (PMHS),[17] rats,[18; 19; 20, 21; 22] and swine [23, 24, 25, 26] models using compressed-gas shock tubes in a laboratory environment or blast tube. Although some of these models provided crucial information on the correlation between IOP levels and injury responses, challenges with shock tube tests still exist, including animal positioning, orientation, and interpretation of the effect of the relatively longer duration of the blast.[27] One previous animal model placed the animal head right outside of shock tube.[24] It brought dramatic changes to the IOP characteristics including the formation of a strong vortex flow and elevated dynamic blast pressure and impulse, which deviated significantly from the free-field blast scenario. Data from rat blast models tested in shock tubes recorded positive phase durations in the range of 4-18 ms, [18, 19, 20, 22] which is longer than blasts in the real world. Without sound scaling laws developed between species of bTBI models, shock tube test results need to be carefully investigated and compared with free-field explosive detonations. In this study, all experiments were performed in an open field blast environment. To minimize multiple waveforms from ground reflections, we placed the animal below the triple point and exposed it to the Mach stem. The IOPs were typical free-field Friedlander blast waves in the Mach stem region based on our analysis of the IOP data.

This study provided detailed ICP response in the swine brain subjected to free-field blasts. Historically, some animal tests have been designed and carried out in an attempt to investigate the mechanism of shock wave transmission to the brain, but only a few animal studies recorded direct pressure within the brain tissue during exposure to blast.[18, 19; 24; 26] In our study, the results have demonstrated that ICP followed a trend of increasing magnitude with increased blast severity.

The relationship between ICP and IOP has been determined in several animal blast studies. We showed that, at different locations in the brain, peak ICP values were close to or lower than the IOP. A similar observation was made by another group investigating the mechanical response of the swine brain subjected to left-sided blasts in a shock tube.[8] The peak IOPs ranged from 110 to 740 kPa with scaled durations from 1.3 to 6.9 ms. ICPs ranged from 80 to 390 kPa and were lower than the IOPs and notably lower than the reflected pressures of 300-2830 kPa. Another swine study by Bauman was performed in both a blast tube and in a simulated building with frontal blasts.[23] The recorded IOP data showed that the test animal was exposed to multiple shock waveforms. Fiber-optic pressure transducers were used to record pressure from within the forebrain, thalamus, and hindbrain of the swine without specifying details related to the locations of transducers. The ICP results showed that for IOP levels of 100-250 kPa, the peak ICP values at the three locations were lower than the IOPs.[26] In addition to swine, smaller animals like rats have also been used. In a rat study, an optic fiber pressure sensor was used to record shock tube generated ICPs. The animals were exposed to a low level blast of about 40 kPa and the recorded peak ICPs

were close to but lower than the IOP in both the frontal and lateral regions of the brain.[18] However, this study only used one ICP sensor in each test, and the results of the study were not statistically analyzed. There were also some discrepancies between findings in the peak ICP values compared to the peak IOP values in rat models. Leonardi et al. reported that peak ICPs in rats were larger than the peak IOPs and suggested that skull flexure due to an immature skull suture could be the source of the pressure increase.[3] One recent study with cadaver rats also showed a higher peak ICP compared to the peak IOP values at different IOP levels.[28] However, the location of the ICP sensor in the brain was not described, and the torso was not properly shielded from the shockwave. Also, the impulse produced in this study was in the range of 165- 497 Pa-s, larger than what we used in this study (160-240 Pa-s).

Blast studies have also been performed on PMHS. In one PMHS study, using a shock tube, four fiber optic sensors were implanted in the right frontal cortex, right lateral ventricle, right parietal lobe and right occipital lobe with the respective depths of the tip of the sensors from the outer surface of the skull being 30, 30, 65, and 30 mm.[17] At each IOP level, the peak ICP values in the frontal lobe were higher than its peak IOP value. This observation was not seen at other locations of the brain. Also, most of the computer models indicated higher peak ICP compared with IOP readings.[26, 29, 30, 31, 32, 33].

The discrepancy between measured and model predicted ICP and IOP readings could be due to several causes. One would be the highly nonlinear relationship between the ICP at various locations and the IOP wave.[26] Due to the impedance mismatch between the skull and the brain, ICP peak values tend to be higher at the boundaries and lower in the central region.[34] With respect to the location of transducers, computer models can precisely pinpoint the coup and countrecoup regions of the brain. The location of the ICP sensors in animal experiments was limited by surgical techniques. The depths of sensors below the skull in all experimental tests were different or not described in detail. Therefore, the ICP readings varied in the published literature as described above. Another reason for ICP differences seen in rats and pig is possibly due to the morphological differences between species. Compared to rats, pigs have a much thicker skull with a complex diploe layer that is full of voids. Computer models, on the other hand, may have oversimplified the skull and yielded predictions that did not match experimental data.

Both linear and angular motions of the head were acquired in our tests. The arrival of the ICP wave was almost simultaneous with head motion. Thus, the head motion was due to the primary blast wave (Figure 14). However, the duration of the motion was relatively short (1-2 ms), which resulted in the maximum head displacement around 2 mm. Similar observations were made by Shridharani et al. who also used swine subjects.[8] They found strong correlations ($R^2 = 0.9$) between peak resultant acceleration and peak IOP in the range of 110 to 740 kPa in a linear model. Their positive phase duration was around 3 ms, and the maximum head displacement was 7.5 mm. Thus, the observed acceleration in these two studies was likely due to the primary shock wave. Well after the passage of the shock wave, we observed inertial

global head movement but the head acceleration due to the blast wind was not significant compared to the initial acceleration due to the primary shock wave. In this study, we have deliberately avoided using HIC as an injury measure because HIC was developed for blunt impact with much longer durations and its validity for acceleration pulses lasting only a few milliseconds is questionable.

It is interesting to note that there is good evidence of blast-induced injury to the brain, based on the quantitative EEG data collected from swine shortly after they were exposed to free-field blasts. However, qEEG data cannot pinpoint the areas of the brain injured by the blast.

The data reported here were acquired from live, anesthetized swine exposed to primary blast waves. This is the first large animal model exposed to free-field blasts in which detailed internal pressure measurements were made at various locations. Head motion due to primary blast waves was also measured. The mechanical responses of swine need to be scaled to the human head to determine human response. However, due to the morphological differences between the two species, scaling laws can be difficult to develop. The direct translation can only be done by finite element modeling to develop tissue level response correlates for swine brain. This tissue level response threshold can be then directly translated to the human brain model enabling the development of blast injury threshold for human. Also, the limited sample size should also be taken into consideration. Due to time limitations to complete nine blast tests on a single animal in 8 hours and failure of the data acquisition system on one occasion, data were available from only 19 tests on 5 animals. Additional testing of more animals should improve the statistical significance of the results.

In terms of the results of the qEEG study, although routine EEG lacks sufficient sensitivity and specificity for diagnosing mTBI, qEEG together with advanced analyses methods, may show promise for clinical applications. It has been reported that qEEG has consistently yielded interesting research results in studies of concussed athletes and patients with mTBI [35]. Novel methodologies for EEG feature extraction are also emerging that may detect subtle brain functional abnormalities and deficits in absence of any clinical mTBI symptoms. Methods such as EEG-wavelet entropy measures [36] and Shannon entropy of the peak frequency shifting [37] can be complementary to current existing qEEG measures for multiple-variable measures and EEG signals classifier using a support vector machine [38]. Multiple qEEG parameters were studied in blast brain injury research. In this study, in addition to traditional EEG bands, SEF90 was also studied. Delta band power, alpha band RMS, MAMP, SEF90 were found to be changed in a swine model after blast exposure.

qEEG abnormalities can persist over time, reflecting the effects of multiple mTBI exposures and recovery of function. Increase of delta band power was referred to subcortical lesions, diffuse lesions, metabolic encephalopathy hydrocephalus and deep midline lesions [39, 40]. qEEG abnormalities can appear early after injury and the clinical utility of qEEG can detect abnormal brain functioning in the acute phase of sport-related concussion [41, 42]. Early EEG research in 300 patients clearly

demonstrated the slowing of major frequency bands and focal abnormalities within 48 hours post-injury [7]. EEG recordings performed during the immediate post-concussion period demonstrated a large amount of "diffusely distributed slow-wave potentials," which were markedly reduced when recordings were performed 6 weeks after injury [43]. The EEG changes found in our study are concordant to these clinical findings. After blast wave exposure, increase delta band power indicates increased amount of slow-wave potentials, decrease of SEF90 indicates the slowing of major frequency bands. A shift in the mean frequency in the alpha (8–10 Hz) band toward lower power was reported in patients suffering from mTBI [44], while decrease of RMS of alpha band with increase of delta power was found earlier after blast exposure in our study.

Only two peer-reviewed studies have examined EEG-recorded brain activity following blast-related injury among soldiers at chronic phase, and neither of these investigated brain activity in the early post-injury phase [10, 11]. Both studies found EEG abnormalities in individuals who were exposed to blast. Acute EEG abnormalities were found in 36% of participants with blast injury and 12% of participants without blast injury [11]. The most common observation was hypersynchronous, discontinuous or irregular brain activity with increased theta activity. At 1-year follow-up, persistent alterations were found in 30% of participants with blast injury and 4% of participants without blast injury. These two studies concluded that conventional EEG data are not sufficient to support the widespread clinical use of qEEG to diagnose blast-related mTBI [10, 11]. Two animal blast studies investigated EEG changes caused by blast exposure. A transient flattening of the electroencephalogram (EEG) was seen immediately after the 237 kPa blast exposure among four of seven (57.1%) swine [14], no more EEG abnormality was reported in this study. In another study in which goats were exposed to 555 - 913 kPa overpressures, decrease of EEG frequency and increases of slow wave percentage were found. Among these goats, 88-89% was burned accompanied with bloody fluid emission from the nose and the mouth. Subarachnoid hemorrhage on the frontal lobe, mesencephalon, and brainstem was found in these goats indicative of severe brain injury [13]. In our study, swine were exposed to 420-450 kPa overpressure and qEEG demonstrated changes indicative of brain injury. Brain dissections did not find any hemorrhage or hematoma, but histological studies found neuronal and glia alternation indicative of brain injury [45]. These outcomes indicated that 420-450 kPa overpressures may cause mild to moderate brain injury. In terms of EEG changes, more qEEG parameters including delta band power, alpha RMS, MAPM, and SEF90 were found to be changed after blast, demonstrating more changes in EEG in our swine than the swine exposed to 237 kPa blast overpressure. Decrease of EEG amplitude was reported in two other blast brain injury researches using a large animal model [13, 14]. These concordant results, indicate that non-invasively obtained qEEG variables could diagnose and predict brain damage and may, thus, be of clinical value.

Previous studies have found the following qEEG changes in mTBI in civilian settings, including reduction in mean alpha frequency [44, 46-48], increased theta activity [43, 49], increased theta-alpha ratios (TAR) based on power [46, 50] and decreased alpha delta ratios (ADR) [16, 51]. This study found that increased delta power 15 minutes after blast was recorded at P_3, P_4 parietal regions in the swine, with decreased alpha

RMS in all 4 recording locations 15 minutes (p<0.05) and 30 minutes (p<0.01) after blast. We also examined TAR and ADR, but we did not find statistically significantly changes. This indicates that blast-induced brain dysfunction may be different from mTBI in the civilian setting [52].

Blast induced brain damage can be caused by direct mechanical insults to brain cells [53-55] and blood network [56-59]. Blast wave produces shear forces on brain tissue [55], even low-amplitude shear forces may induce biochemical processes that yield serious pathology hours and days later [60-62]. Long term blood perfusion deficits have been found in the rats (up to 72 hours) following low level (117 kPa) shock wave exposure [59]. Intracranial pressure was measured to be 312–420 kPa at the various brain locations in our non-survival swine using the same blast setting [63]. Computer simulation demonstrated a high possibility of brain injury under such pressure [64]. Ischemia in the brain was not investigated in the current study. SEF90 has been used in cerebral ischemia research [65, 66], general slowing of the EEG is described which is reflected by a decrease in high frequency (alpha) and an increase in low frequency (delta) activity, resulting in a decrease of SEF90. In the present study, decreased SEF90 was found in the swine 15 minutes after blast exposure. However, whether a blood circulation disturbance occurs following blast exposure at 420-450 kPa overpressure resulting in qEEG abnormalities requires further investigation in the future study.

Our experiments were performed under general anesthesia with propofol and ketamine. The former two substances are known to induce dose-dependent changes in EEG pattern, mostly consisting of decrease in high-frequency activity and increase in low-frequency activity [65]. Ketamine can induce an active EEG signal with increase in theta and beta activity [66]. During the perfusion period of propofol, an increase in the power of the alpha band (10% to 40%) and a decrease in the delta band was noticed [67]. Ketamine and propofol are antagonistic to each other in their interaction [68]. In the current study, ketamine was used to induce initial anesthesia, following by intravascular (IV) induction of propofol and IV maintenance of propofol. Hence under the same maintenance dose of anesthesia, parameters of qEEG should keep stable or delta band power should decrease with alpha band RMS increased. However, after blast exposure, delta power increased with alpha RMS decreased. Hence delta band power decreased and alpha band RMS decreased 15 minutes after blast suggests that these changes are the result of blast exposure rather than from the effects of anesthesia.

This qEEG study has some limitations. Sham group study was not performed in this study. If funds are available, we will perform a sham group in our future studies to better understand qEEG measures in anesthetized blasted swine. Histological studies of brain tissue are underway in the animals that underwent blast and the qEEG study but a correlation of injured brain tissue with qEEG findings has not been made. Finally, implantable telemetry techniques can be used to measure qEEG in a subacute and chronic awake swine model in the future.

(g) Conclusions

The data reported here were acquired from live, anesthetized swine exposed to primary blast waves. This is the first large animal model exposed to free-field blasts in which detailed internal pressure measurements were made at various locations. Head motion due to primary blast waves was also measured. The mechanical responses of swine need to be scaled to the human head to determine human response. However, due to the morphological differences between the two species, scaling laws can be difficult to develop. Also, the limited sample size should also be taken into consideration. Due to time limitations to complete nine blast tests on a single animal in 8 hours and failure of the data acquisition system on one occasion, data were available from only 19 tests on 5 animals. Additional testing of more animals should improve the statistical significance of the results.

In summary, the results of this study provided a set of detailed biomechanical response data of swine skull and brain during exposure to primary blast waves, with the peak IOPs ranging from 143 to 461 kPa, and the impulses ranging from 156 to 239 Pa-s. The overall ICP responses were closer to or lower than its IOP at each blast level. More specifically, peak ICP values at the frontal, parietal, and temporal were statistically the same as the corresponding IOP values. Peak ICP values at the frontal, central, and occipital regions were significantly elevated at the medium and high blast levels compared with the low blast levels. Furthermore, only at the central location, was the ICP significantly different between the medium and high pressures tests. Both the linear acceleration and the angular velocity increased with blast levels. Although the head acceleration was high, its duration was less than 2 ms. It is unlikely that the brain would be able to respond mechanically to this type of acceleration input. These experimental data can be used to validate computer models.

The results of the qEEG study demonstrated that blast induced qEEG changes shortly after blast exposure, including decrease of mean amplitude (MAMP), increase of delta band power, decrease of alpha band root mean square (RMS), and decrease of SEF90. This study demonstrated that qEEG is sensitive for cerebral injury. The changes of qEEG immediately following a blast exposure indicate the potential of utilizing multiple parameters of qEEG for diagnosis of blast-induced brain injury. Early detection of blast induced brain injury can lead to early screening and assessment of brain abnormalities in blast victims to enable timely therapeutic intervention.

2.   Blast Testing of Non-Instrumented Swine

Operations Iraqi Freedom (OIF) and Enduring Freedom (OEF) have highlighted the emergence of Blast Induced Neurotrauma (BINT) and the associated mild traumatic brain injury (mTBI) as the signature wound in returning service members [69,70]. Shell shock and post-concussive syndrome had a similar prominence during World Wars I and II [71]. With much of these injuries more recently sustained following exposure to an improvised explosive device, basic understanding of the mechanisms and pathological changes in the central nervous system following an open field blast

exposure still remains an area of intense research focus. What is still not well studied is whether exposure to primary blast wave causes changes in the gyrencephalic brain. Understanding the pathological changes in the brain following an open field exposure is important considering the complex neurological problems reported in the exposed service members. For example, the history of blast related mTBI has been significantly associated with post-traumatic stress disorder (PTSD) and other physical problems in veterans from OIF [72] as well as those from OEF and Operation New Dawn [73,74]. In addition, the number of exposures also appears to be contributing to the neuropsychological sequelae with increased symptom reporting, as revealed by significant Neurobehavioral Symptom Inventory (NSI) scores in veterans with increased blast exposures [75]. There were also reports of abnormal hormonal levels in one or more pituitary axes [76] in those affected by blast mTBI. Visual dysfunction [77,78] and co-occurrence of auditory, visual and vestibular impairment referred to as multisensory impairment (MSI) was also reported [79] in blast victims. In a sample assessment of veterans, a diagnosis of non-epileptic seizures was suspected in 44% of the samples studied and PTSD was confirmed in 81% of these samples studied. Exposure to blast was considered as the mechanism of the TBI [80] in these samples. In fact, TBI independent of an injury mechanism (blast or non-blast) has been described as a primary driver of adverse outcomes in an analysis of US military personnel [81].

The pathological basis of blast-induced changes is still not well understood. A diffusion tensor imaging analysis of service members revealed that blast mTBI was associated with a pattern of lower white matter integrity, with a larger number of low fractional anisotropy (FA) voxels in those with more than one blast mTBI than in individuals with a single blast injury [82]. Others, albeit using a limited number of blast exposed soldiers also reported abnormalities consistent with cerebellar white matter injury in 3 of 4 subjects studied using diffusion tensor imaging [83]. Compared to control subjects, veterans with blast mTBI also showed neurometabolic changes with significant reductions in the ratio of N-acetylaspartate to choline (NAA/Ch) and N-acetyl aspartate to creatine (NAA/Cr) in the anterior portions of the hippocampus [84].

With limitations in studying brain pathological changes in the blast victims, several animal models using a shock tube system to simulate blast overpressure exposure have gained prominence. Behaviorally, transient anxiety-like behavior in an open field arena was reported in mice subjected to 172-276 kPa blast overpressure with symptoms becoming prominent in those exposed to 345-414 kPa [85]. In rats exposed to blast waves with peak reflected overpressures of either 100 or 450 kPa (39 or 110 kPa incident pressure respectively), FA revealed significant brain abnormalities as evidenced by greater numbers of significant voxels in animals exposed to high-blast compared to low-blast. The decreased FA was observed prominently in the cortex, thalamus and ipsilateral ventral hippocampus [86]. In mice exposed to blast overpressure via a shock tube, Huber et al reported elevated phospho and cleaved-tau species in neurons, as well as elevated manganese superoxide-dismutase levels by 24 hours with the aberrant tau species persisting for at least 30 days post-exposure in the hippocampus [87]. Electrophysiolgically, recordings from the corpus callosum of rat brain slices exposed to blast in the range of 28 kPa indicated greater deficits in

unmyelinated fibers relative to myelinated fibers. There was a reduced compound action potential amplitude at 14 days post-injury [88]. Mice subjected to open field explosion (35 and 17 kPa), demonstrated behavioral changes with increased blood brain barrier permeability, increased FA and decreased radial diffusivity that correlated with sites of up-regulation of manganese superoxide dismutase 2 in neurons and CXC-motif chemokine receptor 3 around blood vessels in the fiber tracts [89].

Histologically, in rats subjected to sub-lethal open field blast overpressure (49 kPa or 77 kPa), darkened and shrunken cortical neurons were observed one day after blast with signs of recovery by 4 and 7 days after blast [88]. They also reported increased number of cells with amyloid precursor protein staining in the white matter [90] with some reporting multi focal axonal injury in the cerebellum, corticospinal tract and optic tract in mice subjected to a static blast pressure of 68 kPa using a shock tube [91]. Blast induced swollen neurons and myelin debris in the hippocampus [92] and accumulation of phosphorylated neurofilament-heavy chain (pNF-H) in neuronal perikarya of the cortex attributed to a disturbed axonal transport machinery was also reported [93]. Using a silver impregnation technique, investigators have also shown axonal pathology in the cortex and cerebellum of swine exposed to blast pressures of 379 or 538 kPa [94] and in deep cerebellar white matter tracts and various brainstem regions of rats with body shielding exposed to a single 241 kPa blast wave [95]. Others showed cytoskeletal damage in the cortex and hippocampus 7 days after blast exposure using neurofilament immunohistochemistry [96]. With the evidence of axonal injury potentially in the form of impaired axoplasmic transport (IAT) in various blast models, it was reasoned that immunostaining for beta amyloid precursor protein (β-APP) and neurofilament light chain, the markers of traumatic axonal injury [97, 98] may offer valuable clues on the extent of neuronal injury in the swine brain following blast exposure.

Glial alterations are another key component of blast induced injury changes in the brain [99]. Alterations related to astrocytes in the brain were prominently shown by several investigators using glial fibrillary acidic protein immunohistochemistry [100-105]. Current research also supports profound microglial activation following blast [106-113] in various animal models. However, studies aimed at understanding changes related to axonal injury and glial proliferation and their quantification in a gyrencephalic brain after a primary blast exposure are limited. Thus, the purpose of this study was to assess neuronal and glial reactivity changes in brains from male Yucatan swine subjected to a single open field blast exposure. Our results from analyses of sections encompassing the frontal lobe of the brain show neuronal and glial injury changes in the gray and white matter regions following open field blast exposure.

Materials and Methods

All procedures were approved by the Institutional Animal Care and Use Committee (IACUC, Wayne State University, Detroit, MI) and the United State Army Medical Research and Materials Command Animal Care and Use Review Office (USAMRMC ACURO). All animals (male Yucatan swine 50-60 kg, 13.4±1.3 months Sinclair Bio Resources LLC, Columbia, MO 65205) were allowed to acclimate to their new housing conditions in the animal quarters prior to any test procedure. On the day of the test, each animal was sedated by an initial intramuscular injection of Ketamine (10 mg/kg once) and xylazine (2 mg/kg once) or ketamine (10 mg/kg once), dexmedetomidine (0.04 mg/kg IM) and acepromazine (0.1 mg/kg IM) in the case of animals subjected to high blast overpressure in the open field blast. Animals subjected to high blast overpressure were also administered buprenorphine sustained release (0.12-0.24 mg/kg; subcutaneous) prior to blast exposure.

Following the initial anesthesia, the animal was intubated and was allowed to breathe spontaneously. Additional ventilatory support was given by an Ambu bag as needed. In animals exposed to medium blast overpressure open blast and sham procedures, anesthesia was maintained by an intravenous infusion of Propofol (12-20 mg/kg). In animals subjected to high blast overpressure, anesthesia was further maintained by intravenous injection of ketamine (5-10 mg/kg/hr) and dexmedetomidine (0.005-0.018 mg/kg). Supplemental intravenous (IV) fluids were administered (Lactated Ringer's Solution 5-10 ml/kg/hour IV) via an intravenous catheter placed in an ear vein. All the animals were transported in an emergency medical services (EMS) vehicle to a test site (ARES Inc., Port Clinton, OH) for open field blast exposure. After blast exposure, the animals were returned to their housing location and monitored till they recovered from the influence of anesthesia. All animals received trained veterinary care throughout their survival period. A total of 17 animals were tested as part this study. In our experience, no animal died prematurely or needed to be euthanized during these tests. Based on the experimental design, all animals were allowed to survive for a period of 3 days.

Animal preparation

All the blast tests were performed on days with no rain or snow. Open field blast overpressure was generated by detonating 3.6 kg of a spherical composition-4 (C4) charge. To attain a single Friedlander waveform, the height of burst was determined to be 0.8 -0.9 m and was achieved by suspending the C4 from a metal chain. The animal with abdominal and thoracic lead shielding (39 kg/sq m) was suspended prone in a canvas harness. The harness was further supported by a steel frame which was suspended from a metal beam (3.7 m off the ground) mounted on two A-frames, as shown in Figure 5. The height of the triple point as a function of the horizontal distance from charge was calculated for the given height of the burst. To expose the animal's head below the triple point, the animal was suspended 0.9 m above the ground. The snout of the animal also was supported by two webbing straps to minimize head motion. The eye level was at 0.9 m (3 ft) above the ground with the head facing the

direction of the wave propagation (Figure 5). After proper alignment of the head with respect to the center of the C4 charge, the steel frame was further tied to four hooks cemented to the concrete ground with straps to prevent excessive motion during the blast exposure.

The intensity of the two blast exposures (medium versus high) was achieved by changing the stand-off distance between the animal's head and the center of the C4 charge (Table 3). The actual side-on overpressure was measured by a pencil probe (PCB137A24, PCB Piezotronics, Depew, New York 14043) mounted on a metal frame that was bolted to the ground and placed next to the animal's head at the same height (0.9 m). The blast pressure data were acquired at a sampling rate of 1 MHz using the SIRIUS HS-ACC MODULE (DEWESoft, Slovenia). Blast animals were divided into two groups that were exposed either to a single medium blast overpressure (stand-off distance = 3.6 m, n=7) or high blast overpressure (stand-off distance = 3.1 m, n=5; Figure 24). Sham animals (n=5) were exposed to identical test conditions but were not subjected to blast exposure.

Stable heart rate with no jaw tone, palpebral reflex, and limb withdrawal reflex were used as indicators of adequate depth of anesthesia. Immediately before/during/after blast, SpO2 and heart rate were monitored by pulse oximetry. Body temperature was monitored continuously by a rectal thermometer. At lower ambient temperatures, supplemental heat (water circulating heating pad or Thermacare Heat Wraps) was provided to maintain body temperature.

Table 3. This table shows the number of animals studied for each group and the recorded open field blast overpressure.

Sham	Medium Blast Overpressure	High Blast Overpressure
Swine 1	Swine1: 223.5 kPa	Swine1: 359.9 kPa
Swine 2	Swine 2: 332.3 kPa	Swine 2: 359.9 kPa
Swine 3	Swine 3: 305.4 kPa	Swine 3: 403.3 kPa
Swine 4	Swine 4: 222 kPa	Swine 4: 403.3 kPa
Swine 5	Swine 5: 262.7 kPa	Swine 5: 350.3 kPa
	Swine 6: no data	
	Swine 7: 290.3 kPa	

Brain tissue processing

All animals were allowed to survive for 3 days after blast or sham procedures. At the end of their survival period, each animal was first injected with Heparin followed by an overdose of sodium pentobarbital and prepared for transcardial perfusion by 4% paraformaldehyde. After ensuring that there was no noxious and palpebral response, the animal was placed supine on a surgical table. The left and right common carotid arteries were exposed and traced inferiorly to the point of their origin in the aortic arch and the connector end of an intravenous tube was inserted into the right

common carotid artery and was secured in place by a suture. Each animal was perfused first with 1 liter of saline followed by 8-10 liters of 4% paraformaldehyde. The venous return was collected from the right atrium by a suction pump. Perfusion of the lower body was minimized by clamping the aorta just inferior to the heart. Following perfusion, the brain was removed and post-fixed in 4% paraformaldehyde with 20% sucrose until processing for immunohistochemical analyses.

Each harvested brain was cut into 5-mm blocks using a swine brain slicer (Zivic Instruments, Pittsburgh, PA 15237). Each block was further cryoprotected in 30% sucrose and then embedded in an optimum cutting compound. Each block was then further cut into 35-40 µm thick frozen serial sections using a cryostat. A total of twenty-four pairs of sections from each of the six blocks were collected in phosphate buffered saline-filled 2-ml vials and stored at 4°C. Then some of the designated sections were probed by various stains to assess cellular injury changes. For each stain, two sections from each block were used. Briefly, the sections were subjected to antigen retrieval by incubation in a citrate buffer (pH 6.0) at 90°C for 1 hour. Then they were immersed for 1 hour in 0.6% hydrogen peroxide to quench endogenous peroxidase activity.

For assessing axonal injury changes, individual sections were subjected to incubation in antibodies against beta amyloid precursor protein (β-APP; 1:250, Cat # 51-2700, Life Technologies, Grand Island, NY), neurofilament light chain (NF-L; 1:5000, Cat#AB9568; Millipore, Temecula CA) or neurofilament-medium chain (NF-M; 1:750; cat # 34-1000, Invitrogen, Camarillo, CA, 1:750). For assessing astrocytic changes, a set of representative sections were incubated in a solution containing antibodies against glial fibrillary acidic protein (GFAP for identifying astrocytes, cat # NE1015, Calbiochem, La Jolla, CA; 1:5000). Microglial activation was detected by incubating a separate set of sections in a solution containing antibodies against ionized calcium-binding adapter molecule 1 (Iba1, cat # 019-19741, Wako Chemicals, Richmond, VA; 1:20000). All the antibody solutions were diluted in 2% normal goat serum (Vector Laboratories, Burlingame, CA) mixed in 1% bovine serum albumin (BSA). After respective primary antibody incubation, sections were incubated in a solution containing a 1:500 dilution of respective biotinylated secondary antibody (Vector Laboratories, Burlingame, CA) followed by exposure to Vectastain Elite ABC reagent. Finally, the peroxidase activity was developed by brief incubation in 3, 3'-diaminobenzidine and hydrogen peroxide. The sections were washed, dehydrated and cover slipped using DPX (Sigma Aldrich). In control incubations, normal goat serum was substituted for primary antibody.

Quantification of β-APP immunoreactivity

The presence of neuronal injury as evidenced by β-APP reactive zones was quantified from one section of each block from sham (n= 5 animals x 6 sections per animal = 30 total sections), medium blast overpressure (n=7 animals x 6 sections per animal = 42 total sections) and high blast overpressure (n= 5 animals x 6 sections = 30 total sections) groups. In the gray matter, an immunoreactive zone was defined as the region encompassing intense β-APP-reactive cell bodies that was observed in various cortical layers including the molecular layer. In the white matter, immunoreactive zones

were defined as aggregates of intense β-APP-reactive axon-like processes, individual retraction balls, axonal swellings or intensely stained stellate-like cells. For quantification, each section (encompassing the entire left and right hemispheres) was viewed under a light microscope (Leica DMLB, Leica Microsystems Ltd, Heerburg, Switzerland) at 50x magnification defined as the high-power field. The presence or absence of β-APP immunoreactive zones in these high-power fields was investigated by a blinded investigator and the total number of gray and white matter immunoreactive zones for each section was recorded.

Quantification of astrocytic and microglial reactivity

Quantification of astrocytes and microglia was performed using separate sets of sections stained for GFAP and Iba1 respectively. For astrocytic quantification in a blinded fashion in blast and sham groups, a x5 composite panoramic image from two sections each per block (sham n= 60 sections; medium blast overpressure n= 84 sections; high blast overpressure n= 60 sections) was taken using OASIS software (Objective Imaging Inc., Kansasville, WI 53139). These panoramic images were then used as a guide to obtain a series of five x100 images per hemisphere, which in turn were used exclusively for counting the number of astrocytes. As the GFAP staining was predominantly found in the white matter tracts, representative images spaced approximately 5 mm apart encompassing the white matter regions were obtained. Then, the number of astrocytes in each such image (10 images per section; 120 images for six blocks per animal resulting in a total of 2040 images for all the 17 animals) were counted.

For quantifying microglia in blast and sham groups another x5 composite panoramic image from two sections each per block per stain (sham n= 60 sections; medium blast overpressure n= 84 sections; high blast overpressure n= 60 sections) was taken using OASIS software (Objective Imaging Inc., Kansasville, WI 53139). However, as microglia were observed in both the white and gray matter regions, using the x5 panoramic images as a guide, another set of five representative images at x100 magnification encompassing areas of both the white and gray matter were taken per hemisphere. This resulted in a total of (10 images per section; 120 images for six blocks per animal) 2040 images for all the 17 animals exclusively for counting microglia. The number of astrocytes and microglia were quantified independently from their respective images using ImageJ. Each image was inverted using the invert option which results in a reverse image similar to the negative of a photograph and enables better delineation of cells of interest from their background.

The average number of β-APP immunoreactive zones in gray and white matter, astrocytes and microglia per group was calculated and compared statistically for group-wise differences using Statistical Package for the Social Sciences (SPSS, IBM) software. One-way analysis of variance (ANOVA) was used for comparisons across study groups. Post hoc LSD tests were used for pair-wise comparisons as appropriate. A probability level of $p < 0.05$ was considered statistically significant.

Serum analyses for injury markers

Besides collecting the brain for histological analyses, serum samples were collected before and at 6 hours, 24 hours, 48 hours and 72 hours after the blast or sham procedures. These samples were assessed for temporal changes in the expression of phosphorylated neurofilament heavy chain (pNF-H Elisa Kit, Encor Biotechnology, Gainesville, FL), glial fibrillary acidic protein (GFAP; cat#NS830, EMD Millipore, Billerica, MA) and interleukin-6 (IL-6; cat# ESIL6, Life Technologies, Carlsbad, CA) by enzyme-linked immunosorbent assay (ELISA) as per the manufacturer's instructions. The ELISA data were analyzed by generalized estimating equations (GEE) with an exchangeable correlation structure and robust standard errors. Baseline biomarker data were entered as a covariate to address possible baseline imbalance.

Results

Axonal injury: β-APP immunohistochemistry

Our investigation revealed more prominent β-APP immunoreactive zones in the open field blast exposure group than in the sham group. A further analysis revealed that the number of β-APP immunoreactive zones in the gray matter of high blast overpressure group was significantly higher compared to those from both the medium blast overpressure and sham groups ($p<0.05$) with no other changes (Figure 24A). Immunoreactive zones in the gray matter were observed in various cortical layers characterized by 1-3 intensely stained cell bodies with plaque-like deposits with extended processes of the cell bodies (Figure 24E, 24F). These immunoreactive zones were also observed in the sub-pial regions of the cortex. The components of β-APP immunoreactive zones in the white matter regions were the presence of axons undergoing pathological changes. A further analysis of these white matter injuries revealed that the extent of these injuries in the high blast overpressure group was significantly higher compared to the medium blast over pressure and sham groups ($p<0.05$). Furthermore, the extent of these injuries was also significantly higher in the medium blast overpressure group compared to sham ($p<0.05;$ Figure 24B). These pathological changes were in the form of single or multiple axonal swellings, swollen axons with terminal retraction balls and retraction balls with or without tail-like profiles (Figure 24G and 24H). These axonal injury profiles were particularly predominant in the sub-cortical coronal radiations ending in various sulci, more so in the dorsal aspect of the cerebral hemispheres. Other areas that also showed injured axons were internal capsule, white matter bundles of the striatum, and white matter fibers near the vomiro nasal organ. Occasionally, axonal injury was also observed in the periventricular white matter tracts and corpus callosum. Immunoreactive zones in the white matter were also associated with stellate-like cells with their dark stained processes surrounded by retraction balls and axons showing signs of swellings (Figure 24I). Immunoreactive zones in sham sections tended to be less intense (Figure 24D) with no staining in control sections (24C).
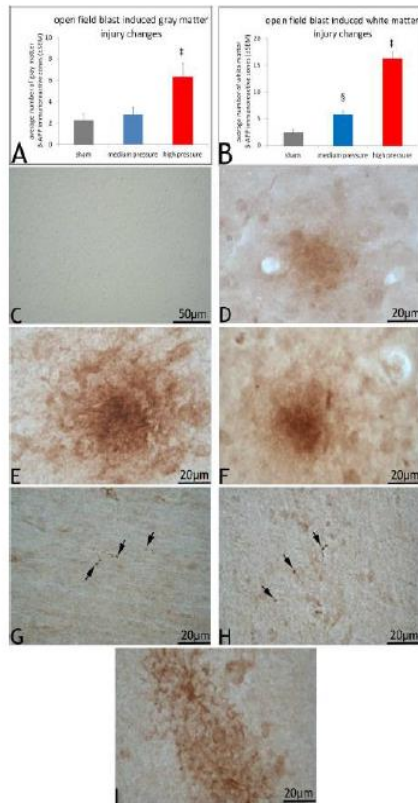
Figure 24. β-APP immunoreactivity in the blast and sham swine. 1A shows average number (± standard error of the mean, SEM) of β-APP immunoreactive zones in the gray matter of blast and sham swine sections. The number of β-APP immunoreactive zones in the gray matter of high blast overpressure sections were significantly high (‡) compared to those in sham and medium blast overpressure (*p<0.05*; LSD; One-way ANOVA). 1B shows average number (± standard error of the mean, SEM) of β-APP immunoreactive zones in the white matter of blast and sham swine sections. The number of β-APP immunoreactive zones in the white matter of high blast overpressure sections (‡) were significantly high compared to those in sham and medium blast overpressure (*p<0.05*; LSD; One-way ANOVA). Furthermore, the extent of white matter immunoreactive zones was also significantly high in the medium blast overpressure sections (§) compared to sham (*p<0.05;* LSD; One-way ANOVA). 1C shows a control section stained without the primary antibody showing no apparent immunoreaction. 1D shows a sham section showing a less intense gray matter β-APP immunoreactive region. 1E and 1F shows an intensely stained gray matter immunoreactive zone from a representative high and medium blast overpressure swine sections. 1G and 1H show representative β-APP reactive retraction balls in the cortical white matter tracts. 1I shows an immunoreactive zone with stellate-like profiles in the white matter tracts of a swine subjected to high blast overpressure.

Axonal injury: NF-L and NF-M immunohistochemistry

A limited attempt to assess axonal injury by NF-L and NF-M immunohistochemistry was performed. In brain sections from swine exposed to medium and high blast overpressure, many NF-L reactive axons with uniform caliber and well-stained axonal core were observed. However, some large caliber axons with altered morphology were also observed (Figure 25A-C). These axons tended to have membrane boundaries that appeared to be disrupted in the form of semilunar empty space or occasionally with filamentous projections originating from their membranes. Besides, some of the large caliber axons appeared to be swollen and at times with the presence of vacuoles in their axonal core. In addition, some axons with terminal retraction bulbs appearing as clubs were also observed. The location of these observed changes was predominantly in the sub-cortical white matter tracts. In the corpus callosum, no such prominent observations could be made considering the predominant nature of small fiber axons in its population. Qualitatively, in sections from sham animals, NF-L reactive axons running for extended lengths in the white matter tracts were observed. These axons appeared to have uniform caliber with well stained NF-L reactive core (Figure 25D). Axonal injury changes assessed by NF-M immunohistochemistry revealed putative axons that appeared to be linear with occasional swollen regions (arrow) and vacuolations (Figure 26). These limited findings need to be further validated.
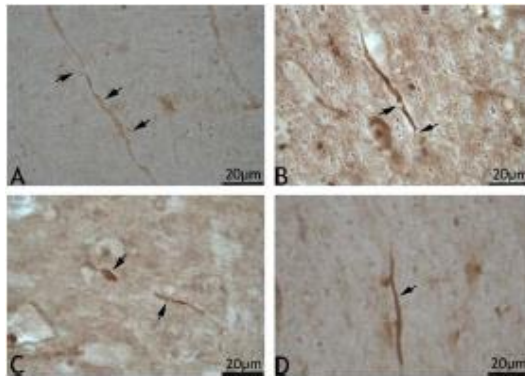

Figure 25. NF-L immunoreactive large caliber nerve fibers in blast and sham sections. 2A shows an axon with swollen regions (arrows) in a brain section from the medium blast overpressure group. 2B and 2C show swollen axons with apparent vacuolations and retraction balls in a section from the high blast overpressure group. 2D shows a normal appearing axon in a section from the sham group.

Astrocytic reactivity changes

In all the sections from the six blocks of the frontal lobes, the astrocytes were almost exclusively localized to the white matter tracts (Figure 27) and thus images were exclusively obtained from the white matter tracts for the purpose of quantification. Although astrocytes in other areas of the cortex and sub-pial regions were observed they were less prominent than in white matter tracts. Quantification of images revealed a significantly high number (p<0.05; Figure 28A) of GFAP reactive astrocytes in sections from both the medium and high blast overpressure groups compared to those from sham (Figure 28B). Furthermore, astrocyte counts in sections from high blast overpressure group were also significantly higher compared to those from medium blast overpressure (p<0.05). Astrocytes in the blast group tended to be intensely stained by GFAP with numerous processes (Figure 28C and 28D). In addition, astrocytes in the blast groups appeared to undergo morphological changes with enlarged cell bodies (Figure 28D).

Microglial reactivity changes

In the case of microglia, they were observed throughout the layers of the cortex, sub cortical white matter tracts and other structures with no specific distribution pattern. The number of microglia in both the blast groups was higher than in sections from sham group (p<0.05; Figure 29A). Unlike astrocytes, the microglial counts in the medium blast overpressure blast group were significantly higher than in the high blast overpressure group (p<0.05). Compared to sham (Figure 29B), microglia in the blast group (Figure 29C and 29D) tended to be more oval in shape with limited number of processes.
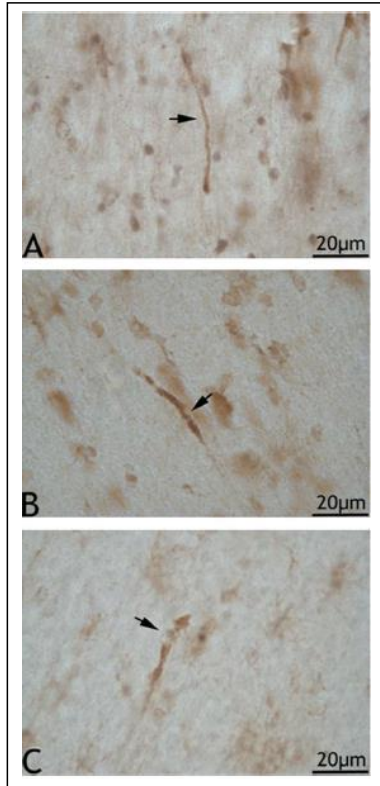
Figure 26. NF-M immunoreactive large caliber axons in the cortical radiations. 3A
shows normal looking axon in a sham brain section. 3B and 3C show apparently
reactive axons. 3B shows an axon with an apparent vacuole like (arrow) presence in a
section from medium blast overpressure group. 3C shows a large caliber axon with a
terminal putative enlargement preceded by vacuolated appearance (arrow) in a section
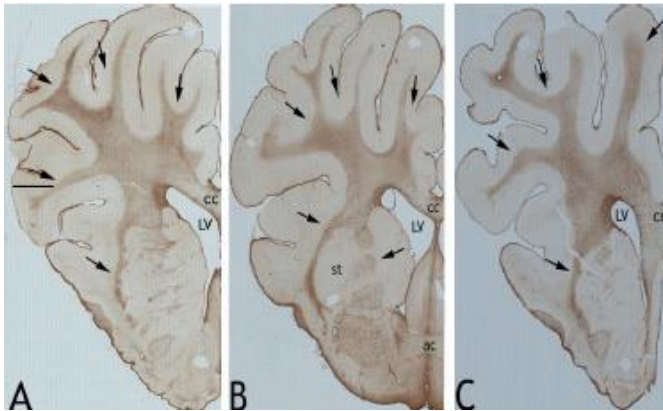from a high blast overpressure group.

Figure 27. Astrocytic reactivity in the white matter tracts. Representative panoramic images of sections of GFAP stained left hemispheres from a typical sham (A), medium (B) and high (C) blast overpressure exposed swine. Arrows indicate white matter radiations into the cortex and other tracts that appeared to be clearly delineated from the gray matter. Note the intense staining of the neuropile. (CC= corpus callosum; LV= lateral ventricle; st = striatum; ac = anterior commissure)
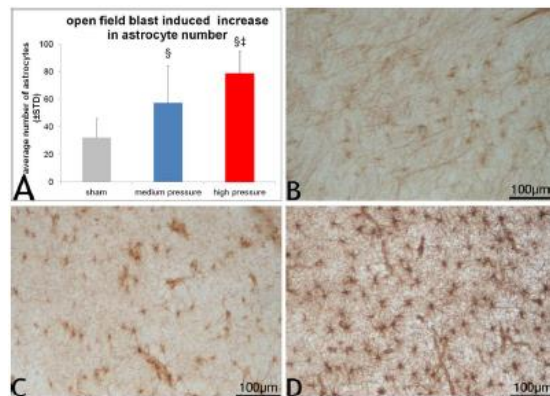

Figure 28. Quantification of open field blast induced astrogliosis. 5A shows the astrocyte counts in the blast and sham groups. Astrocyte counts in sections from the high and medium blast overpressure group were significantly elevated compared to those from sham group. Astrocyte counts in the high blast overpressure group were significantly higher than in the medium blast overpressure group. 5B shows an image of lightly stained astrocytes in a representative sham section. 5C and 5D show increased astrocytic proliferation in medium and high blast overpressure exposed sections. Furthermore, astrocytes in blast sections appeared to be intensely stained with enlarged cell bodies and processes (5D).
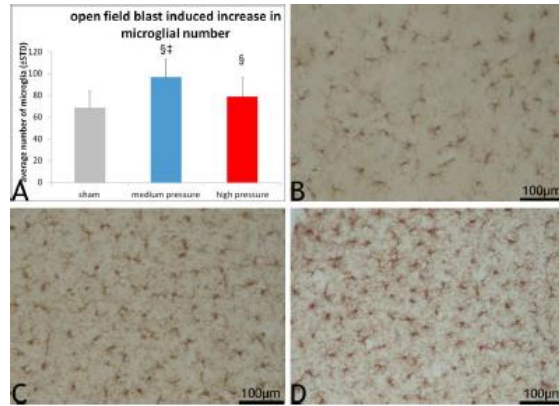
Figure 29. Open field blast induced microglial proliferation. 6A shows extent of the microglial counts in the blast and sham groups. Microglial counts in sections from the high and medium blast overpressure blast groups were significantly higher compared to those from sham group. 6B-D show representative images from sham, medium and high blast overpressure exposed sections highlighting variations in microglial proliferation. Microglia in blast sections appeared to be enlarged in size.

Serum biomarker changes

ELISA data from the three markers was compared for statistical significance using generalized estimating equations. Baseline biomarker data were entered as a covariate to address possible baseline imbalance. Of the three biomarkers analyzed, there was some evidence of higher glial fibrillary acidic protein levels in the high blast overpressure group than the sham group ($p = 0.08$). No apparent difference in glial fibrillary acidic protein levels was found between sham and medium blast overpressure group. No significant changes were observed with regard to the serum levels of phosphorylated neurofilament heavy chain and interleukin 6.

3   Correlation of results between biomechanical responses and histological findings

We can say with confidence that blast overpressure at the medium and high pressure levels resulted in injury to both the neurons and the axons in the frontal region of swine brain. However, the histological study of the rest of the brain is still in progress and we cannot arrive at any injury conclusions for the whole brain. However, our biomechanical (pressure) data indicate that the peak pressure throughout the brain was fairly uniform and no specific area of the brain was subjected unusually high pressures except perhaps at the interface of the brain with the frontal bone. We intend to publish a second paper on our histological findings upon completion of the histological studies which is being done by volunteer students under the guidance of Dr. S. Kallakuri.

Discussion

To our knowledge, this study is the first of its kind to attempt to address the fundamental question whether an open field blast exposure causes injurious changes in the gyrencephalic brain. Although there were other studies that attempted to address the same question in a gyrencephalic model using explosives, animals in those studies were exposed to a simulated open field blast by positioning the animal either in a shock tube, high mobility multipurpose wheeled vehicle surrogate or in a four-sided building with no roof using a moderate charge [94,105,114]. Another previous open field blast study (2.1 kg explosive) positioned the animal on a steel shelf mounted to the concrete wall of the bunker and studied only physiological parameters such as respiration, circulation and cortical activity but no histological analyses of brain for injury changes as in the current study [115]. Säljö et al on the other hand, offers some details on the effects of repetitive blast pressure (3 times during a 10-15 minute period) in swine exposed to low level noise produced by various weapons (a howitzer, a bazooka, an automatic rifle) or underwater explosives [116]. They reported that animals exposed to bazooka (Pmax 42 kPa) and automatic rifle (Pmax 23 kPa) showed significant increase in subarachnoidal and small parenchymal bleedings in cortical regions with occipital lobe and cerebellum being the most predominantly affected structures. Animals exposed to howitzer blasts at 30 kPa although displaying parenchymal and subarachnoid hemorrhages, were not significantly different from that of controls due to the limitations in the number of animals. Säljö et al concluded that low levels of blast causes brain edema as indicated by increased bioelectric impedance, an increase in intracranial pressure, small brain hemorrhages and impaired cognitive function [117]. In our study, the animals were exposed to higher open field blast pressure than these animals and the likelihood of such hemorrhages although possible was not investigated as the focus was to study neuronal injury and glial reactivity changes.

We studied injury changes in the brain following an open field blast in Yucatan swine suspended in a sling and positioned below the triple point and exposed to a single Friedlander wave form either at medium (range 222 kPa - 333 kPa; average 272±5 kPa) or high blast overpressure (range 350-403 kPa; average 375±3 kPa). Our lowest medium blast overpressure of 222 kPa was similar to the mean shock tube blast pressure (241±8 kPa) reported by de Lanerolle et al [86] in Yorkshire swine. Besides, the shock tube pressures reported by de Lanerolle et al ranged from 131-365 kPa [105] with their lowest pressure range far lower than in our study. In our experience, there were no mortalities in both the medium and high blast overpressure groups. These pressures were very close to those utilized by de Lanerolle et al [86] who reported shock tube and vehicular blast pressures in the range of 255-365 kPa with potentially long durations that may be a contributing factor for the observed mortality [105]. Furthermore, the medium and high blast overpressures used in our study are higher than those used by Gyorgy et al [114] who used three different blast overpressures of <152 kPa, 138-276 kPa and >276 kPa respectively on Yorkshire swine and reported time dependent changes in serum biomarkers [114].

This initial report offers data on neural, astrocytic and microglial changes from the most anterior aspect of the brain to about 30 mm posterior. Our findings suggest, that open field blast exposure causes neuronal injury and marked increase in the number of astrocytes and microglia as early as three days after blast in the cortical gray and white matter regions of the frontal lobe. Although not investigated, it is plausible that these injury changes can progressively evolve and can extend to more chronic time periods as supported by the findings from de Lanerolle et al who studied changes two weeks after blast in swine [105]. Neuronal injury in the form of beta amyloid immunoreactive cell bodies, stellate cells, axonal swellings and retraction balls in sections from blast group was observed. The axonal injury in the form of terminal retraction balls and beaded profiles was very similar to previous findings of diffuse axonal injury following traumatic brain injury induced by an impact acceleration device [118]. Furthermore, the microscopic nature of these changes may not allow them to be detected either by routine or advanced radiological assessments and may render diagnosis of blast related pathology even more difficult. The immunoreactive zones in gray matter may suggest accumulation of β-APP in the cell bodies that may be related to impaired axoplasmic transport. An increased cytoplasmic β-APP staining in the perikarya following traumatic brain injury also was previously reported [119,120]. Additionally, up-regulation of β-APP in cells including Purkinje cells and hippocampal neurons has been reported in a rodent model of cranial blast [121]. Furthermore, some of the beta amyloid stained regions in the white matter resembled glial cells with projections. For that matter, there is an increase in the number of microglia in both the gray and white matter regions of sections from the blast exposure groups compared to sham. In fact, Ryu et al recently reported APP positive axonal abnormalities in several brain sites from veterans that suffered blast injury that appeared as clusters of axonal spheroids or varicosities in a honeycomb pattern with perivascular distribution in the medial dorsal frontal white matter [122] The honeycomb appearance of immunoreactivity in their study may be related to the presence of staining around microglial cells that may be responsible for the characteristic honeycomb appearance in the white matter tracts and may need to be validated by dual labeling immunofluorescence for β-APP and microglial markers. β-APP reactive axonal profiles in the medium and high blast overpressure group were observed in sections encompassing the prefrontal and frontal lobes predominantly in the dorsal sub cortical white matter structures. These frontal lobe axonal changes were further supported by NF-L and NF-M immunoreactive axons. Axonal changes evidenced by NF-L immunoreactive swollen profiles, with vacuolations and club-like terminations were observed in various sub cortical white matter tracts. In fact NF-L immunohistochemistry was previously used to show the pathogenesis of diffuse axonal injury following traumatic brain injury [123] with others showing cell body changes evidenced by accumulation of phosphorylated neurofilament heavy chain in rats exposed to explosive blast in a shock tube [93]. Although this needs further validation, we also show some putative signs of neurofilament compaction. Neurofilament compaction is one of the components of traumatic axonal injury [124] with the other being impaired axoplasmic transport revealed by β-APP immunohistochemistry [118,124]. In fact, the predominance of β-APP reactive profiles in the blast groups supports the dominance of impaired axoplasmic transport which was reported to be localized to the thin caliber axons [125] as revealed by very thin β-APP

reactive profiles especially in the sub cortical white matter. In addition, the utility of β-APP immunohistochemistry was also reported by other investigators studying blast related changes in rodents [95,126].

The presence of a high number of GFAP reactive astrocytes delineating the white matter in the blast swine brain sections is another hallmark of this study with the number of astrocytes increasing with increasing pressure. The presence of astrocytes delineating the white matter tracts implicates and supports their strong association with ongoing neuronal injury changes in the white matter tracts and to our knowledge this type of white matter delineation was never reported in a gyrencephalic blast brain injury model. De Lanerolle et al also reported astrocytes in subpial cortex and white matter of Yorkshire swine, an observation similar to our findings. However, quantitatively, they reported significant astrocyte increase in regions of hippocampus in swine exposed to blast in a vehicle and building but not in the shock tube setting [105]. On the other hand, Bauman et al using two Yorkshire swine exposed to moderate peak pressure in a high mobility multipurpose wheeled vehicle (HMMVEE) showed astrocytosis in the ipsilateral superior corona radiata (exposed side) of the posterior frontal cortex as well as in multiple layers of the dentate gyrus. They also showed elevated GFAP levels in the ipsilateral frontal cortices of the two swine tested [94]. With the very limited swine studies, much of the knowledge related to blast induced astroglial changes comes from several rodent blast studies [90,100,103, 111, 127-129]. For example, Svetlov et al showed peak GFAP accumulation in the hippocampus seven days after blast exposure to 358 kPa that persisted for 30 days post-blast by western blot analysis with no significant accumulation in the cortex at any of the survival periods. They also showed significant serum and cerebrospinal GFAP levels at 24 hours and four days after blast respectively [32]. In a separate study that subjected rats either to composite or primary blast, prominent astrocytosis in the hippocampus was reported at 1 and 7 days after blast with elevated serum GFAP levels at 6 hours, 1 day and 7 days respectively following composite or primary blast [35]. Sajja et al using an established shock tube blast overpressure model, reported elevated GFAP levels 24 hours after exposure (117 kPa) but not after 48 hours [60]. Garman et al on the other hand, reported no prominent GFAP and Iba1 staining (although small number of reactive microglia was found in areas of neuronal death) in any of the survival periods studied (24 hours, 72 hours, 2 weeks) in rats subjected to head only exposed blast overpressure of 241 kPa [111]. Turner et al, using a tabletop shock tube, reported graded astrocytic reactivity in the corpus callosum based on the exposed peak overpressure [128] similar to our findings that showed an increased astrocyte count with increasing blast pressure. The histological observation of prominent GFAP in our study is further supported by high GFAP serum levels albeit insignificant in the high-pressure group. Taken together, these findings may support GFAP to be a candidate biomarker of blast induced neurotrauma. In a study of Yorkshire pigs, Gyorgy et al did not report injury changes by histology, but showed a time dependent increase in S100B and also reported high variability among animals [112]. Sevtlov et al showed a significant increase in blood GFAP levels by 24 hours with levels in CSF showing a decline and accumulation in a time dependent manner in rats [100].

Another striking observation from our study is the significant increase in the number of microglia in the medium blast overpressure swine sections compared to high blast overpressure and sham groups. This type of differential expression of microglia and astrocytes in swine blast has never been reported. In our study, microglia were observed in both the cortical and white matter regions with no preferential localization. However, de Lanerolle et al although reported no difference in the distribution of microglia in the superior frontal cortex and hippocampus between blast and controls, but observed prominently activated microglia in the central white matter and corpus callosum with no additional quantitative data in swine that survived for 2 weeks after blast [105]. The extent of microglial response at chronic time periods after open field blast is yet to be fully studied. Similar to astrocytes, much of the knowledge related to blast induced microglial changes comes from rodent studies using blast wave [106,109] and impulse noise [107]. Sajja et al in their recent report on pathological changes after low (69 kPa), moderate (97 kPa) and high (165 kPa) shock tube overpressures reported a differential expression of microglia and astrocytes seven-days post-blast survival period, a finding very similar to our observations. They reported significant increase in microglial reactivity in low pressure group alone with increase in astrocytes with increasing pressure [130]. This is different from Turner et al who reported an increase in the number of corpus callosum microglia with increasing pressure (217, 350, and 497 kPa) [104] with Garman et al previously reporting only slight evidence for microglial activation in rats subjected to 241 kPa blast overpressure [95]. On the other hand, Kaur et al reported microglial cells in close association with some darkened dendrites in rats subjected to single non-penetrating blast [106]. A putative pathological implication for microglia comes from studies by Kane et al that showed an increased expression of microglial genes related to immune function and inflammatory responses in cultured microglia subjected to overpressure [112]. Despite several important findings, our study is marked by certain limitations such as lack of functional assessment of the animals following blast exposure and unbiased stereology in histological assessment. Although there was evidence of increasing serum biomarkers levels in the blast groups compared to sham, no significant differences were observed which may be related to wide variations and limited samples size.

What are the potential implications of the observed astrocytic and microglial activation in the frontal lobes of the brain? One implication is their potential role in neurodegeneration. It was recently shown that transforming growth factor beta from immature astrocytes could initiate synaptic elimination in post-natal thalamus by regulating the expression of C1q, a subcomponent of C1 complex of complement activation in the retinal ganglion cells [64]. C1q can trigger classic complement pathway that can lead to tagging of the supernumerary synapses with C3b fragment derived from complement activation and their ultimate elimination by microglia [65,66]. There may also be a bidirectional relationship between the activation of astrocytes and that of microglia. For example, the attenuation of reactive gliosis in a model of AD led to a high number of microglia in the vicinity of plaques and cortex [134]. Whereas the attenuation of astrocytic activation in a mouse model of Batten disease was shown to be accompanied by increased number of microglia in the brain [135]. What could be the potential implication of differential astrocytic and microglial response as observed in

this study? Does it mean that at lower pressures, cellular injury changes may be more discrete and modulated by microglia with high pressures leading to activation of both microglia and astrocytes with the latter playing a dominant role? It is very likely that astrocytes may serve as markers of injury severity. As their number increases with increasing pressure, there may be an array of neuronal and inflammatory injury changes as well as potential blood brain barrier permeability disruptions as indicated by their apparent high serum concentrations. Furthermore, the presence of astrocytes almost exclusively delineating white matter tracts may be an indication of the extensive white matter injury following blast exposure. In addition, it is also possible that mechanical perturbations in the tissue trigger astrocyte derived adenosine triphosphate release which may lead to rapid recruitment of microglia to the site of injury and can lead to both microglial and astrocytic reactivity responses [136]. The role of microglia and astrocytes contributing to the release of various inflammatory mediators has been well reported. For that matter, studies by Bauman et al and others have shown increased levels of tumor necrosis factor, interleukin 1 beta, and interferon-γ in cerebrospinal fluid and serum following blast [92,103] lending support also to the inflammatory nature of blast pathology.

Conclusions

In conclusion, our investigation of a gyrencephalic brain three days after open field blast exposure supports the presence of a robust neuronal injury accompanied by extensive astrocytic and microglial activation in the frontal lobes. The severity of the observed neuronal and astrocytic changes appeared to be proportional to the level of blast exposure. The microglial response appears to be differential with high numbers at medium blast overpressure and low numbers at high blast pressure. Whether these injury changes extend to more posterior aspects and brainstem parts is a major aspect of our ongoing investigations. The functional implication of these observed changes may be related to neuronal, axonal and dendritic degeneration combined with a cascade of inflammatory mediator release.

References for Task I

1. Airoldi L, Beghi E, Bogliun G, Crespi V, Frattola L. Rational use of EEG in adults in clinical practice. J Clin Neurophysiol 1999;16(5):456-61.
2. Gaetz M, Bernstein DM. The current status of electrophysiologic procedures for the assessment of mild traumatic brain injury. J Head Trauma Rehabil 2001;16(4):386-405.
3. Nuwer M. Assessment of digital EEG, quantitative EEG, and EEG brain mapping: report of the American Academy of Neurology and the American Clinical Neurophysiology Society. Neurology 1997;49(1):277-92.
4. Nuwer MR, Hovda DA, Schrader LM, Vespa PM. Routine and quantitative EEG in mild traumatic brain injury. Clin Neurophysiol 2005;116(9):2001-25.
5. Jordan KG. Emergency EEG and continuous EEG monitoring in acute ischemic stroke. J Clin Neurophysiol 2004;21(5):341-52.

6. Thatcher RW, Walker RA, Gerson I, Geisler FH. EEG discriminant analyses of mild head trauma. Electroencephalogr Clin Neurophysiol 1989;73(2):94-106.
7. Geets W, Louette N. Early EEG in 300 cerebral concussions. Rev Electroencephalogr Neurophysiol Clin 1985;14(4):333-8.
8. Thatcher RW, Moore N, John ER, Duffy F, Hughes JR, Krieger M. QEEG and traumatic brain injury: rebuttal of the American Academy of Neurology 1997 report by the EEG and Clinical Neuroscience Society. Clin Electroencephalogr 1999;30(3):94-8.
9. Thatcher RW, North DM, Curtin RT, Walker RA, Biver CJ, Gomez JF, Salazar AM. An EEG severity index of traumatic brain injury. J Neuropsychiatry Clin Neurosci 2001;13(1):77-87.
10. Trudeau DL, Anderson J, Hansen LM, Shagalov DN, Schmoller J, Nugent S, Barton S. Findings of mild traumatic brain injury in combat veterans with PTSD and a history of blast concussion. J Neuropsychiatry Clin Neurosci 1998;10(3):308-13.
11. Cernak I, Savic J, Ignjatovic D, Jevtic M. Blast injury from explosive munitions. J Trauma 1999;47(1):96-103; discussion 103-4.
12. Sponheim SR, McGuire KA, Kang SS, Davenport ND, Aviyente S, Bernat EM, Lim KO. Evidence of disrupted functional connectivity in the brain after combat-related blast injury. Neuroimage 2011;54 Suppl 1:S21-9.
13. Li BC, Li Y, Xu C, Wang J, Chen Z, Li G, Zhang J, Hu S, Wang L, Feng H. Blast-induced traumatic brain injury of goats in confined space. Neurol Res 2014;36(11):974-82.
14. Axelsson H, Hjelmqvist H, Medin A, Persson JK, Suneson A. Physiological changes in pigs exposed to a blast wave from a detonating high-explosive charge. Mil Med 2000;165(2):119-26.
15. Weenink RP, Vrijdag XC, van Putten MJ, Hollmann MW, Stevens MF, van Gulik TM, van Hulst RA. Quantitative electroencephalography in a swine model of cerebral arterial gas embolism. Clin Neurophysiol 2012;123(2):411-7.
16. Lee SJ, Hatran DP, Tomimatsu T, Pena JP, McAuley G, Longo LD. Fetal cerebral blood flow, electrocorticographic activity, and oxygenation: responses to acute hypoxia. J Physiol 2009;587(Pt 9):2033-47.
17. Bir C, Measuring blast-related intracranial pressure within the human head, DTIC Document, 2011.
18. Chavko M, Koller WA, Prusaczyk WK, McCarron RM, Measurement of blast wave by a miniature fiber optic pressure transducer in the rat brain. J Neurosci Methods 159:277-281, 2007.
19. Leonardi AD, Bir CA, Ritzel DV, VandeVord PJ, Intracranial pressure increases during exposure to a shock wave. Journal of Neurotrauma 28:85-94, 2011.
20. Huber, BR, Meabon JS, Martin TJ, P.D. Mourad, Bennett R, Kraemer BC, Cernak I, Petrie EC, Emery MJ, Swenson ER, Mayer C, Mehic E, Peskind ER, Cook DG, Blast exposure causes early and persistent aberrant phospho- and cleaved-tau expression in a murine model of mild blast-induced traumatic brain injury. Journal of Alzheimer's Disease. 37:309-323, 2013.
21. Gullotti DM, Beamer M, Panzer MB, Chen YC, Patel TP, Yu A, Jaumard N, Winkelstein B, Bass CR, Morrison B, Meaney DF, Significant head accelerations can influence immediate neurological impairments in a murine model of blast-

induced traumatic brain injury. Journal of Biomechanical Engineering 136:091004, 2014.

22. Goldstein LE, Fisher AM, Tagge CA, Zhang XL, Velisek L, Sullivan JA, Upreti C, Kracht JM, Ericsson M, Wojnarowicz MW, Goletiani CJ, Maglakelidze GM, Casey N, Moncaster JA, Minaeva O, Moir RD, Nowinski CJ, Stern RA, Cantu RC, Geiling J, Blusztajn JK, Wolozin BL, Ikezu T, Stein TD, Budson AE, Kowall NW, Chargin D, Sharon A, Saman S, Hall GF, Moss WC, Cleveland RO, Tanzi RE, Stanton PK, McKee AC, Chronic traumatic encephalopathy in blast-exposed military veterans and a blast neurotrauma mouse model. Science Translational Medicine 4,134ra60, 2012.

23. Bauman RA, Ling G, Tong L, Januszkiewicz A, Agoston D, de Lanerolle Kim NY, Ritzel D, Bell Ecklund RJ, Armonda R, Bandak F, Parks S, An introductory characterization of a combat-casualty-care relevant swine model of closed head injury resulting from exposure to explosive blast. Journal of neurotrauma 26:841-860, 2009.

24. Shridharani JK, Wood GW, Panzer MB, Capehart BP, Nyein MK, Radovitzky RA, Bass CR, Porcine head response to blast. Frontiers in Neurology Vol. 3, Article 70, 2012.

25. Saljo A, Arrhen F, Bolouri H, Mayorga M, Hamberger A, Neuropathology and pressure in the pig brain resulting from low-impulse noise exposure. Journal of Neurotrauma 25:1397-1406, 2008.

26. Zhu F, Skelton P, Chou CC, Mao H, Yang KH, King AI, Biomechanical responses of a pig head under blast loading: a computational simulation. Int J Numer Method Biomed Eng 29:392-407, 2013.

27. Needham CE, Ritzel D, Rule GT, Wiri S, Young L, Blast testing issues and TBI: Experimental models that lead to wrong conclusions. Frontiers in Neurology 6:72, 2015.

28. Skotak M, Wang F, Alai A, Holmberg A, Harris S, Switzer RC, Chandra N, Rat injury model under controlled field-relevant primary blast conditions: acute response to a wide range of peak overpressures. Journal of Neurotrauma 30:1147-1160, 2013.

29. Zhang L, Makwana R, Sharma S, Brain response to primary blast wave using validated finite element models of human head and advanced combat helmet. Frontiers in Neurology 4:88, 2013.

30. Chafi MS, Karami G, Ziejewski M, Biomechanical assessment of brain dynamic responses due to blast pressure waves. Annals of Biomedical Engineering 38:490-504, 2010.

31. Moore DF, Jerusalem A, Nyein M, Noels L, Jaffee MS, Radovitzky RA, Computational biology - modeling of primary blast effects on the central nervous system. NeuroImage 47 Suppl 2, T10-20, 2009.

32. Zhu F, Mao H, Cengio Leonardi AD, Wagner C, Chou C, Jin X, Bir C, Vandevord P, Yang KH, King AI, Development of an FE model of the rat head subjected to air shock loading. Stapp Car Crash Journal 54:211-225, 2010.

33. Taylor PA, Ford CC, Simulation of blast-induced early-time intracranial wave physics leading to traumatic brain injury. J Biomech Eng 131:061007, 2009.

34. Meyers MA, Dynamic behavior of materials, Wiley, New York, 1994.

35. Slobounov S, Gay M, Johnson B, Zhang K. Concussion in athletics: ongoing clinical and brain imaging research controversies. Brain Imaging Behav 2012;6(2):224-43.
36. Slobounov S, Cao C, Sebastianelli W. Differential effect of first versus second concussive episodes on wavelet information quality of EEG. Clin Neurophysiol 2009;120(5):862-7.
37. Cao C, Slobounov S. Application of a novel measure of EEG non-stationarity as 'Shannon- entropy of the peak frequency shifting' for detecting residual abnormalities in concussed individuals. Clin Neurophysiol 2011;122(7):1314-21.
38. Cao C, Tutwiler RL, Slobounov S. Automatic classification of athletes with residual functional deficits following concussion by means of EEG signal using support vector machine. IEEE Trans Neural Syst Rehabil Eng 2008;16(4):327-35.
39. Fraga FJ, Falk TH, Kanda PA, Anghinah R. Characterizing Alzheimer's disease severity via resting-awake EEG amplitude modulation analysis. PLoS One 2013;8(8):e72240.
40. Babiloni C, Frisoni G, Steriade M, Bresciani L, Binetti G, Del Percio C, Geroldi C, Miniussi C, Nobili F, Rodriguez G, Zappasodi F, Carfagna T, Rossini PM. Frontal white matter volume and delta EEG sources negatively correlate in awake subjects with mild cognitive impairment and Alzheimer's disease. Clin Neurophysiol 2006;117(5):1113-29.
41. Barr WB, Prichep LS, Chabot R, Powell MR, McCrea M. Measuring brain electrical activity to track recovery from sport-related concussion. Brain Inj 2012;26(1):58-66.
42. McCrea M, Prichep L, Powell MR, Chabot R, Barr WB. Acute effects and recovery after sport-related concussion: a neurocognitive and quantitative brain electrical activity study. J Head Trauma Rehabil 2010;25(4):283-92.
43. McClelland RJ, Fenton GW, Rutherford W. The postconcussional syndrome revisited. J R Soc Med 1994;87(9):508-10.
44. Tebano MT, Cameroni M, Gallozzi G, Loizzo A, Palazzino G, Pezzini G, Ricci GF. EEG spectral analysis after minor head injury in man. Electroencephalogr Clin Neurophysiol 1988;70(2):185-9.
45. Zhang L, Kallakuri S, Desai A, Mathei J, Dawe L, Feng K, Chen C, Cavanaugh J, King A. Open Field Primary Blast Exposure Induces Neuronal and Glial Alternations in Frontal Cortex Journal of Neurotrauma 2015; 32(A-1-A-152):Page B2-12.
46. Chen XP, Tao LY, Chen AC. Electroencephalogram and evoked potential parameters examined in Chinese mild head injury patients for forensic medicine. Neurosci Bull 2006;22(3):165-70.
47. Gosselin N, Lassonde M, Petit D, Leclerc S, Mongrain V, Collie A, Montplaisir J. Sleep following sport-related concussions. Sleep Med 2009;10(1):35-46.
48. Korn A, Golan H, Melamed I, Pascual-Marqui R, Friedman A. Focal cortical dysfunction and blood-brain barrier disruption in patients with Postconcussion syndrome. J Clin Neurophysiol 2005;22(1):1-9.
49. Fenton G, McClelland R, Montgomery A, MacFlynn G, Rutherford W. The postconcussional syndrome: social antecedents and psychological sequelae. Br J Psychiatry 1993;162:493-7.

50. Watson MR, Fenton GW, McClelland RJ, Lumsden J, Headley M, Rutherford WH. The post-concussional state: neurophysiological aspects. Br J Psychiatry 1995;167(4):514-21.

51. Claassen J, Hirsch LJ, Kreiter KT, Du EY, Connolly ES, Emerson RG, Mayer SA. Quantitative continuous EEG for detecting delayed cerebral ischemia in patients with poor-grade subarachnoid hemorrhage. Clin Neurophysiol 2004;115(12):2699-710.

52. Fischer BL, Parsons M, Durgerian S, Reece C, Mourany L, Lowe MJ, Beall EB, Koenig KA, Jones SE, Newsome MR, Scheibel RS, Wilde EA, Troyanskaya M, Merkley TL, Walker M, Levin HS, Rao SM.. Neural activation during response inhibition differentiates blast from mechanical causes of mild to moderate traumatic brain injury. J Neurotrauma 2014;31(2):169-79.

53. Garman RH, Jenkins LW, Switzer RC, 3rd, Bauman RA, Tong LC, Swauger PV, Parks SA, Ritzel DV, Dixon CE, Clark RS, Bayir H, Kagan V, Jackson EK, Kochanek PM.. Blast exposure in rats with body shielding is characterized primarily by diffuse axonal injury. J Neurotrauma 2011;28(6):947-59.

54. Sanborn B, Nie X, Chen W, Weerasooriya T. Inertia effects on characterization of dynamic response of brain tissue. J Biomech 2012;45(3):434-9.

55. Chen YC, Smith DH, Meaney DF. In-vitro approaches for studying blast-induced traumatic brain injury. J Neurotrauma 2009;26(6):861-76.

56. Hua Y, Lin S, Gu L. Relevance of Blood Vessel Networks in Blast-Induced Traumatic Brain Injury. Comput Math Methods Med 2015;2015:928236.

57. Hue CD, Cho FS, Cao S, Nicholls RE, Vogel Iii EW, Sibindi C, Arancio O, Bass C, Meaney D, Morrison Iii B, 3rd. Time Course and Size of Blood-Brain Barrier Opening in a Mouse Model of Blast-Induced Traumatic Brain Injury. J Neurotrauma 2016;33(13):1202-11.

58. Kabu S, Jaffer H, Petro M, Dudzinski D, Stewart D, Courtney A, Courtney M, Labhasetwar V. Blast-Associated Shock Waves Result in Increased Brain Vascular Leakage and Elevated ROS Levels in a Rat Model of Traumatic Brain Injury. PLoS One 2015;10(5):e0127971.

59. Bir C, Vandevord P, Shen Y, Raza W, Haacke EM. Effects of variable blast pressures on blood flow and oxygen saturation in rat brain as evidenced using MRI. Magn Reson Imaging 2012;30(4):527-34.

60. Koliatsos VE, Cernak I, Xu L, Song Y, Savonenko A, Crain BJ, Eberhart CG, Frangakis CE, Melnikova T, Kim H, Lee D.. A mouse model of blast injury to brain: initial pathological, neuropathological, and behavioral characterization. J Neuropathol Exp Neurol 2011;70(5):399-416.

61. Saljo A, Svensson B, Mayorga M, Hamberger A, Bolouri H. Low-level blasts raise intracranial pressure and impair cognitive function in rats. J Neurotrauma 2009;26(8):1345-52.

62. Kan EM, Ling EA, Lu J. Microenvironment changes in mild traumatic brain injury. Brain Res Bull 2012;87(4-5):359-72.

63. Zhang L, Feng K, Chen C, Jin X, Kallakuri S, Cavanaugh JM, King AI. Mechanical Response of Swine Exposed to Free-Filed Blasts. Journal of Neurotrauma 2015;32(A1-A152):A105.

64. Zhu F, Skelton P, Chou CC, Mao H, Yang KH, King AI. Biomechanical responses of a pig head under blast loading: a computational simulation. Int J Numer Method Biomed Eng 2013;29(3):392-407.

65. Brown L, van de Molengraft J, Yazicioglu RF, Torfs T, Penders J, Van Hoof C. A low-power, wireless, 8-channel EEG monitoring headset. Conf Proc IEEE Eng Med Biol Soc 2010;2010:4197-200.

66. Sloan TB. Anesthetic effects on electrophysiologic recordings. J Clin Neurophysiol 1998;15(3):217-26.

67. Herregods L, Rolly G, Mortier E, Bogaert M, Mergaert C. EEG and SEMG monitoring during induction and maintenance of anesthesia with propofol. Int J Clin Monit Comput 1989;6(2):67-73.

68. Bojak I, Day HC, Liley DT. Ketamine, Propofol, and the EEG: A Neural Field Analysis of HCN1-Mediated Interactions. Front Comput Neurosci 2013;7:22.

69. Snell FI, Halter MJ (2010) A signature wound of war: mild traumatic brain injury. J Psychosoc Nurs Ment Health Serv 48: 22-28.

70. Eskridge SL, Macera CA, Galarneau MR, Holbrook TL, Woodruff SI, Mac Gregor AJ, et al. (2012) Injuries from combat explosions in Iraq: injury type, location, and severity. Injury 43: 1678-1682.

71. Jones E, Fear NT, Wessely S (2007) Shell shock and mild traumatic brain injury: a historical review. Am J Psychiatry 164: 1641-1645.

72. Hoge CW, McGurk D, Thomas JL, Cox AL, Engel CC, Castro CA. (2008) Mild traumatic brain injury in U.S. Soldiers returning from Iraq. N Engl J Med 358: 453-463.

73. Neipert L, Pastorek NJ, Troyanskaya M, Scheibel RS, Petersen NJ, Levin HSl. (2014) Effect of clinical characteristics on cognitive performance in service members and veterans with histories of blast-related mild traumatic brain injury. Brain Inj 28: 1667-1674.

74. Troyanskaya M, Pastorek NJ, Scheibel RS, Petersen NJ, McCulloch K, Wilde EA, et al. (2015) Combat Exposure, PTSD Symptoms, and Cognition Following Blast-Related Traumatic Brain Injury in OEF/OIF/OND Service Members and Veterans. Mil Med 180: 285-289.

75. Reid MW, Miller KJ, Lange RT, Cooper DB, Tate DF, Bailie J, et al. (2014) A multisite study of the relationships between blast exposures and symptom reporting in a post-deployment active duty military population with mild traumatic brain injury. J Neurotrauma 31: 1899-1906.

76. Wilkinson CW, Pagulayan KF, Petrie EC, Mayer CL, Colasurdo EA, Shofer JB, et al. (2012) High prevalence of chronic pituitary and target-organ hormone abnormalities after blast-related mild traumatic brain injury. Front Neurol 3: 11.

77. Magone MT, Kwon E, Shin SY (2014) Chronic visual dysfunction after blast-induced mild traumatic brain injury. J Rehabil Res Dev 51: 71-80.

78. Lemke S, Cockerham GC, Glynn-Milley C, Cockerham KP (2013) Visual quality of life in veterans with blast-induced traumatic brain injury. JAMA Ophthalmol 131: 1602-1609.

79. Pogoda TK, Hendricks AM, Iverson KM, Stolzmann KL, Krengel MH, Baker E, et al. (2012) Multisensory impairment reported by veterans with and without mild traumatic brain injury history. J Rehabil Res Dev 49: 971-984.

80. Chen LL, Baca CB, Choe J, Chen JW, Ayad ME, Cheng EM. (2014) Posttraumatic epilepsy in operation enduring freedom/operation iraqi freedom veterans. Mil Med 179: 492-496.
81. Mac Donald CL, Johnson AM, Wierzechowski L, Kassner E, Stewart T, Nelson EC, et al. (2014) Prospectively assessed clinical outcomes in concussive blast vs nonblast traumatic brain injury among evacuated US military personnel. JAMA Neurol 71: 994-1002.
82. Davenport ND, Lim KO, Armstrong MT, Sponheim SR (2012) Diffuse and spatially variable white matter disruptions are associated with blast-related mild traumatic brain injury. Neuroimage 59: 2017-2024.
83. Mac Donald C, Johnson A, Cooper D, Malone T, Sorrell J, Shimony J, et al. (2013) Cerebellar white matter abnormalities following primary blast injury in US military personnel. PLoS One 8: e55823.
84. de Lanerolle NC, Hamid H, Kulas J, Pan JW, Czlapinski R, Rinaldi A, et al. (2014) Concussive brain injury from explosive blast. Ann Clin Transl Neurol 1: 692-702.
85. Heldt SA, Elberger AJ, Deng Y, Guley NH, Del Mar N, Rogers J, et al. (2014) A novel closed-head model of mild traumatic brain injury caused by primary overpressure blast to the cranium produces sustained emotional deficits in mice. Front Neurol 5: 2.
86. Budde MD, Shah A, McCrea M, Cullinan WE, Pintar FA, Stemper BD. (2013) Primary blast traumatic brain injury in the rat: relating diffusion tensor imaging and behavior. Front Neurol 4: 154.
87. Huber BR, Meabon JS, Martin TJ, Mourad PD, Bennett R, Kraemer BC, et al. (2013) Blast exposure causes early and persistent aberrant phospho- and cleaved-tau expression in a murine model of mild blast-induced traumatic brain injury. J Alzheimers Dis 37: 309-323.
88. Park E, Eisen R, Kinio A, Baker AJ (2013) Electrophysiological white matter dysfunction and association with neurobehavioral deficits following low-level primary blast trauma. Neurobiol Dis 52: 150-159.
89. Rubovitch V, Ten-Bosch M, Zohar O, Harrison CR, Tempel-Brami C, Stein E, et al. (2011) A mouse model of blast-induced mild traumatic brain injury. Exp Neurol 232: 280-289.
90. Pun PB, Kan EM, Salim A, Li Z, Ng KC, Moochhala SM, et al. (2011) Low level primary blast injury in rodent brain. Front Neurol 2: 19.
91. Koliatsos VE, Cernak I, Xu L, Song Y, Savonenko A, Crain BJ, et al. (2011) A mouse model of blast injury to brain: initial pathological, neuropathological, and behavioral characterization. J Neuropathol Exp Neurol 70: 399-416.
92. Cernak I, Wang Z, Jiang J, Bian X, Savic J (2001) Ultrastructural and functional characteristics of blast injury-induced neurotrauma. J Trauma 50: 695-706.
93. Saljo A, Bao F, Haglid KG, Hansson HA (2000) Blast exposure causes redistribution of phosphorylated neurofilament subunits in neurons of the adult rat brain. J Neurotrauma 17: 719-726.
94. Bauman RA, Ling G, Tong L, Januszkiewicz A, Agoston D, Delanerolle N, et al. (2009) An introductory characterization of a combat-casualty-care relevant swine model of closed head injury resulting from exposure to explosive blast. J Neurotrauma 26: 841-860.

95. Garman RH, Jenkins LW, Switzer Iii RC, Bauman RA, Tong LC, Swauger PV, et al. (2011) Blast exposure in rats with body shielding is characterized by diffuse axonal injury. Journal of neurotrauma.

96. Macgregor AJ, Dougherty AL, Galarneau MR (2010) Injury-Specific Correlates of Combat-Related Traumatic Brain Injury in Operation Iraqi Freedom. J Head Trauma Rehabil 26: 312-318.

97. Stone JR, Okonkwo DO, Dialo AO, Rubin DG, Mutlu LK, Povlishock JT, et al. (2004) Impaired axonal transport and altered axolemmal permeability occur in distinct populations of damaged axons following traumatic brain injury. Exp Neurol 190: 59-69.

98. Yaghmai A, Povlishock J (1992) Traumatically induced reactive change as visualized through the use of monoclonal antibodies targeted to neurofilament subunits. J Neuropathol Exp Neurol 51: 158-176.

99. Vandevord PJ, Leung LY, Hardy W, Mason M, Yang KH, King AI. (2008) Up-regulation of reactivity and survival genes in astrocytes after exposure to short duration overpressure. Neurosci Lett 434: 247-252.

100. Svetlov SI, Prima V, Kirk DR, Gutierrez H, Curley KC, Hayes RL, et al. (2010) Morphologic and biochemical characterization of brain injury in a model of controlled blast overpressure exposure. The Journal of trauma 69: 795-804.

101. Ahmed F, Gyorgy A, Kamnaksh A, Ling G, Tong L, Parks S, et al. (2012) Time-dependent changes of protein biomarker levels in the cerebrospinal fluid after blast traumatic brain injury. Electrophoresis 33: 3705-3711.

102. Vandevord PJ, Bolander R, Sajja VS, Hay K, Bir CA (2011) Mild Neurotrauma Indicates a Range-Specific Pressure Response to Low Level Shock Wave Exposure. Annals of biomedical engineering.

103. Svetlov SI, Prima V, Glushakova O, Svetlov A, Kirk DR, Gutierrez H, et al. (2012) Neuro-glial and systemic mechanisms of pathological responses in rat models of primary blast overpressure compared to "composite" blast. Frontiers in neurology 3: 15.

104. Turner RC, Naser ZJ, Logsdon AF, DiPasquale KH, Jackson GJ, Robson MJ, et al. (2013) Modeling clinically relevant blast parameters based on scaling principles produces functional & histological deficits in rats. Experimental neurology 248: 520-529.

105. de Lanerolle NC, Bandak F, Kang D, Li AY, Du F, Swauger P, et al. (2011) Characteristics of an explosive blast-induced brain injury in an experimental model. J Neuropathol Exp Neurol 70: 1046-1057.

106. Kaur C, Singh J, Lim MK, Ng BL, Yap EP, Ling EA. (1995) The response of neurons and microglia to blast injury in the rat brain. Neuropathol Appl Neurobiol 21: 369-377.

107. Saljo A, Bao F, Hamberger A, Haglid KG, Hansson HA (2001) Exposure to short-lasting impulse noise causes microglial and astroglial cell activation in the adult rat brain. Pathophysiology 8: 105-111.

108. Hicks RR, Fertig SJ, Desrocher RE, Koroshetz WJ, Pancrazio JJ (2010) Neurological effects of blast injury. J Trauma 68: 1257-1263.

109. Readnower RD, Chavko M, Adeeb S, Conroy MD, Pauly JR, McCarron RM, et al. (2010) Increase in blood-brain barrier permeability, oxidative stress, and

activated microglia in a rat model of blast-induced traumatic brain injury. Journal of neuroscience research 88: 3530-3539.

110. Pun PB, Kan EM, Salim A, Li Z, Ng KC, Moochhala SM, et al. (2011) Low level primary blast injury in rodent brain. Frontiers in neurology 2: 19.

111. Garman RH, Jenkins LW, Switzer RC, 3rd, Bauman RA, Tong LC, Swauger PV, et al. (2011) Blast exposure in rats with body shielding is characterized primarily by diffuse axonal injury. Journal of Neurotrauma 28: 947-959.

112. Kane MJ, Angoa-Perez M, Francescutti DM, Sykes CE, Briggs DI, Leung Y, et al. (2012) Altered gene expression in cultured microglia in response to simulated blast overpressure: possible role of pulse duration. Neuroscience letters 522: 47-51.

113. Sajja VS, Ereifej ES, Vandevord PJ (2014) Hippocampal vulnerability and subacute response following varied blast magnitudes. Neuroscience letters 570C: 33-37.

114. Gyorgy A, Ling G, Wingo D, Walker J, Tong L, Parks S, et al. (2011) Time-dependent changes in serum biomarker levels after blast traumatic brain injury. J Neurotrauma 28: 1121-1126.

115. Axelsson H, Hjelmqvist H, Medin A, Persson JK, Suneson A (2000) Physiological changes in pigs exposed to a blast wave from a detonating high-explosive charge. Mil Med 165: 119-126.

116. Saljo A, Arrhen F, Bolouri H, Mayorga M, Hamberger A (2008) Neuropathology and pressure in the pig brain resulting from low-impulse noise exposure. J Neurotrauma 25: 1397-1406.

117. Saljo A, Mayorga M, Bolouri H, Svensson B, Hamberger A (2011) Mechanisms and pathophysiology of the low-level blast brain injury in animal models. Neuroimage 54 Suppl 1: S83-88.

118. Kallakuri S, Li Y, Zhou R, Bandaru S, Zakaria N, Zhang L, et al. (2012) Impaired axoplasmic transport is the dominant injury induced by an impact acceleration injury device: An analysis of traumatic axonal injury in pyramidal tract and corpus callosum of rats. Brain research 1452: 29-38.

119. Itoh T, Satou T, Nishida S, Tsubaki M, Hashimoto S, Ito H. (2009) Expression of amyloid precursor protein after rat traumatic brain injury. Neurol Res 31: 103-109.

120. Kilbourne M, Kuehn R, Tosun C, Caridi J, Keledjian K, Bochicchio G, et al. (2009) Novel model of frontal impact closed head injury in the rat. J Neurotrauma 26: 2233-2243.

121. Kuehn R, Simard PF, Driscoll I, Keledjian K, Ivanova S, Tosun C, et al. (2011) Rodent model of direct cranial blast injury. J Neurotrauma 28: 2155-2169.

122. Ryu J, Horkayne-Szakaly I, Xu L, Pletnikova O, Leri F, Eberhart C, et al. (2014) The problem of axonal injury in the brains of veterans with histories of blast exposure. Acta Neuropathol Commun 2: 153.

123. Povlishock JT (1993) Pathobiology of traumatically induced axonal injury in animals and man. Ann Emerg Med 22: 980-986.

124. Stone JR, Singleton RH, Povlishock JT (2001) Intra-axonal neurofilament compaction does not evoke local axonal swelling in all traumatically injured axons. Exp Neurol 172: 320-331.

125. Marmarou CR, Walker SA, Davis CL, Povlishock JT (2005) Quantitative analysis of the relationship between intra- axonal neurofilament compaction and impaired axonal transport following diffuse traumatic brain injury. J Neurotrauma 22: 1066-1080.
126. Koliatsos VE, Cernak I, Xu L, Song Y, Savonenko A, Crain BJ, et al. (2011) A mouse model of blast injury to brain: initial pathological, neuropathological, and behavioral characterization. Journal of neuropathology and experimental neurology 70: 399-416.
127. Sajja VS, Galloway MP, Ghoddoussi F, Thiruthalinathan D, Kepsel A, Hay K, et al. (2012) Blast-induced neurotrauma leads to neurochemical changes and neuronal degeneration in the rat hippocampus. NMR in biomedicine 25: 1331-1339.
128. Turner RC, Naser ZJ, Logsdon AF, DiPasquale KH, Jackson GJ, Robson MJ, et al. (2013) Modeling clinically relevant blast parameters based on scaling principles produces functional & histological deficits in rats. Exp Neurol 248: 520-529.
129. Risling M, Plantman S, Angeria M, Rostami E, Bellander BM, Kirkegaard M, et al. (2011) Mechanisms of blast induced brain injuries, experimental studies in rats. Neuroimage 54 Suppl 1: S89-97.
130. Sajja VS, Perrine SA, Ghoddoussi F, Hall CS, Galloway MP, Vandeord PJ. (2014) Blast neurotrauma impairs working memory and disrupts prefrontal myo-inositol levels in rats. Molecular and cellular neurosciences 59: 119-126.
131. Bialas AR, Stevens B (2013) TGF-beta signaling regulates neuronal C1q expression and developmental synaptic refinement. Nat Neurosci 16: 1773-1782.
132. Schafer DP, Lehrman EK, Kautzman AG, Koyama R, Mardinly AR, Yamasaki R, et al. (2012) Microglia sculpt postnatal neural circuits in an activity and complement-dependent manner. Neuron 74: 691-705.
133. Stevens B, Allen NJ, Vazquez LE, Howell GR, Christopherson KS, Nouri N, et al. (2007) The classical complement cascade mediates CNS synapse elimination. Cell 131: 1164-1178.
134. Kraft AW, Hu X, Yoon H, Yan P, Xiao Q, Wang Y, et al. (2013) Attenuating astrocyte activation accelerates plaque pathogenesis in APP/PS1 mice. FASEB J 27: 187-198.
135. Macauley SL, Pekny M, Sands MS (2011) The role of attenuated astrocyte activation in infantile neuronal ceroid lipofuscinosis. J Neurosci 31: 15575-15585.
136. Burda JE, Bernstein AM, Sofroniew MV (2015) Astrocyte roles in traumatic brain injury. Exp Neurol.

TASK II REPORT

Task II – Perform open field blast testing on 6 unembalmed post-mortem human
subjects (PMHS) also known as cadavers to obtain biomechanical data

Summary Report

PMHS blast tests were conducted on six cadavers (five males and one female) for this
project. The bodies arrived in the lab about five days after death and they were tested
within ten days after death. Also, during the post-mortem period prior to
instrumentation, the specimens were kept at 4 °C. Relevant biological data on the
specimens are provided in Table 1.

Table 1. PMHS Data

MHS ID	Sex	Age (Yrs.)	Height (m)	Weight (kg)	Test Date
BRC13102001	Male	72	1.68	66.7	10/18/13
UM34869	Female	32	1.52	47.6	05/21/15
WSU 34930	Male	87	1.78	63.5	09/24/15
UM 35133	Male	73	1.73	77.1	09/28/16
UM 35153	Male	87	1.60	63.5	11/04/16
UM 35162	Male	79	1.68	74.4	11/18/16

PMHS Preparation
Six intracranial pressure sensors were instrumented on frontal, parietal, left/right
temporal, and occipital region of the skull. The detail description of location is shown in
Table 2. An accelerometer block, containing 3 linear accelerometers and 3 angular rate
sensors, was mounted on the apex of the skull surface (see Figure 1).

Table 2. Intracranial pressure sensor locations (X: A-P direction; Y: L-R direction)

|	
Frontal	X: 50 mm anterior to the Bregma Y: 20 mm lateral from mid-sagittal plane
Parietal	X: 20 mm posterior to the Bregma Y: 20 mm lateral from mid-sagittal plane
Temporal	X: 20 mm posterior to the Bregma Y: 40 mm superior to the auditory canal
Occipital	X: 20 mm anterior to the Lambda Y: 20 mm lateral from mid-sagittal plane
All sensors were located 5 mm deep into cortex, except for that in the central brain which was 50 mm below the cortex.	
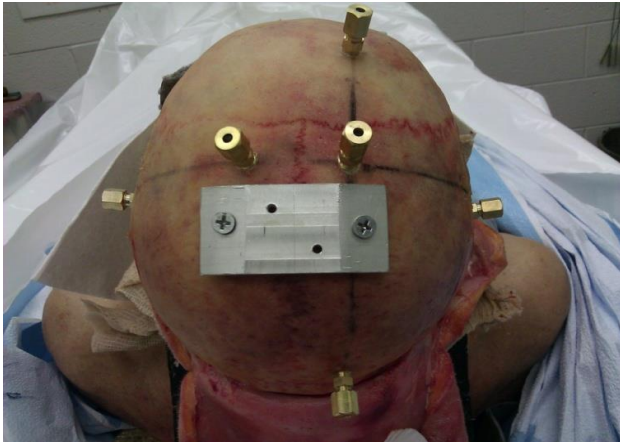
Figure 1. Location of ICP sensors and accelerometer block

PMHS blast tests were conducted at ARES, Inc. in Port Clinton, OH. For each cadaver, nine tests were conducted at three pre-determined nominal peak pressure levels of 150, 300 and 400 kPa. Perfusion was performed (Cadaver No.2-No.6) prior to each blast. The test subject was hung upside down at the knee on the A-frame, as shown in Figure 2 so that it can be easily turned to accomplish frontal lateral and rear blasts. A T-frame was fixed to the cadaver back using a five-point harness system. Sand bags and straps were attached to the T-frame to limit the motion of the upper body of the cadaver.

Figure 2 The cadaver was suspended upside down at the knees

Summary of Results

Intracranial pressure (ICP) and linear accelerometer data were filtered at CFC 6000 and angular rate data were filtered at CFC 3000. All six cadaveric testing results have been processed and reported separately in previous reports. The ICP data for all six cadaver tests at each region were summarized into one plot for model validation purposes. Sample plots at frontal region are provided in this report. We will submit a manuscript on the cadaver blast test for possible journal publication.

Table 3. Summary of ICP results or frontal region
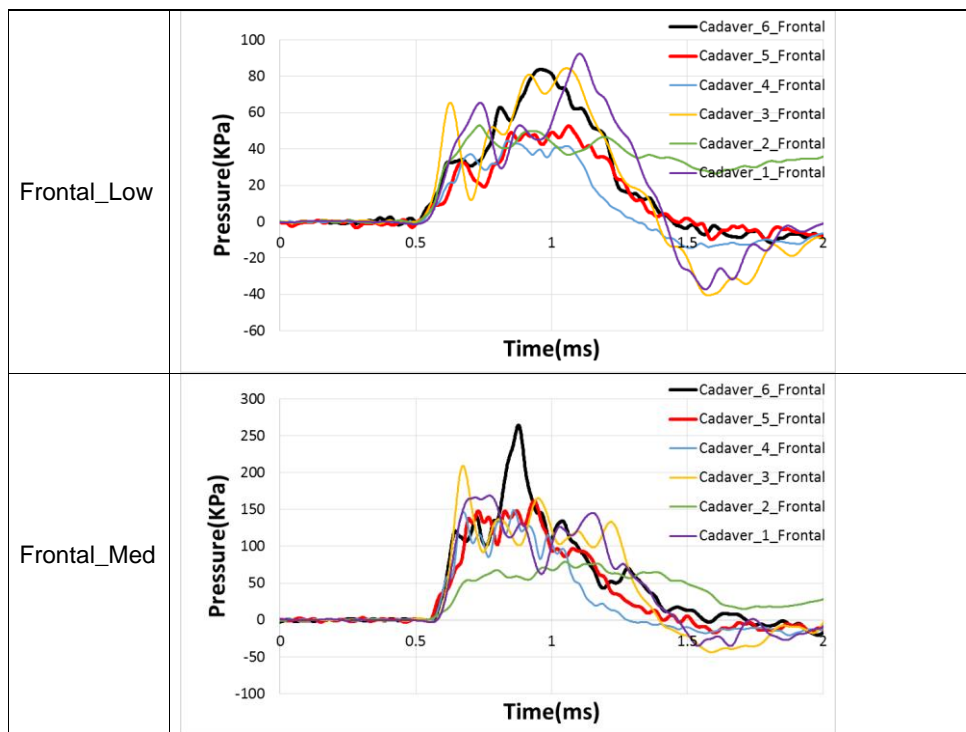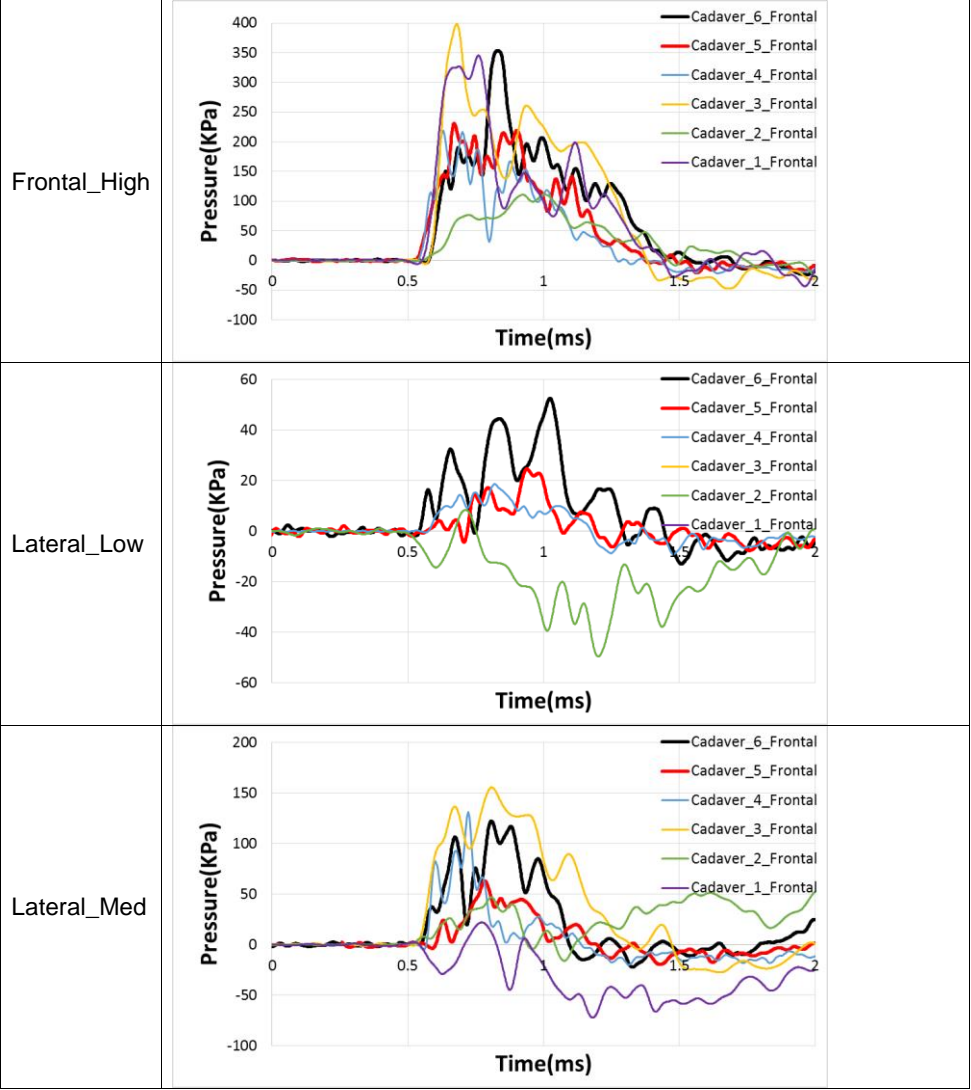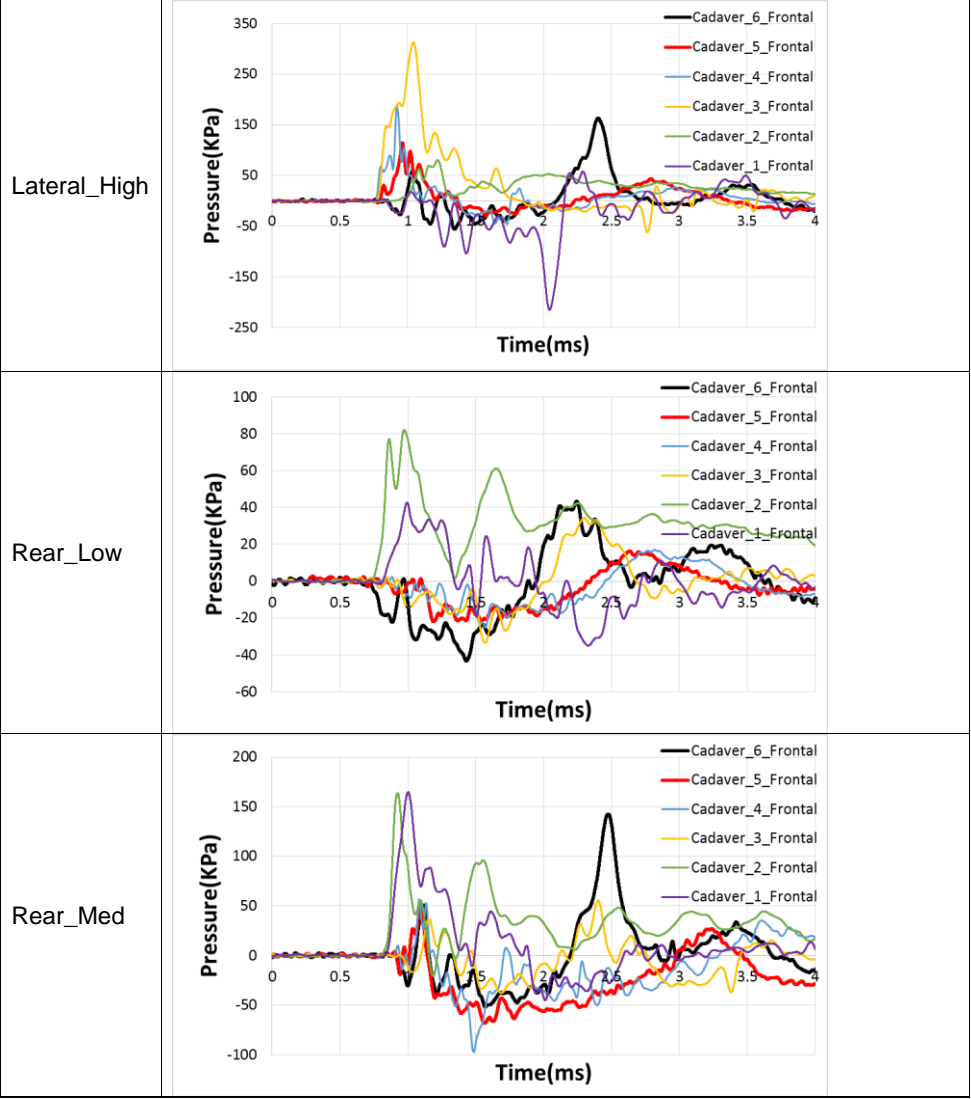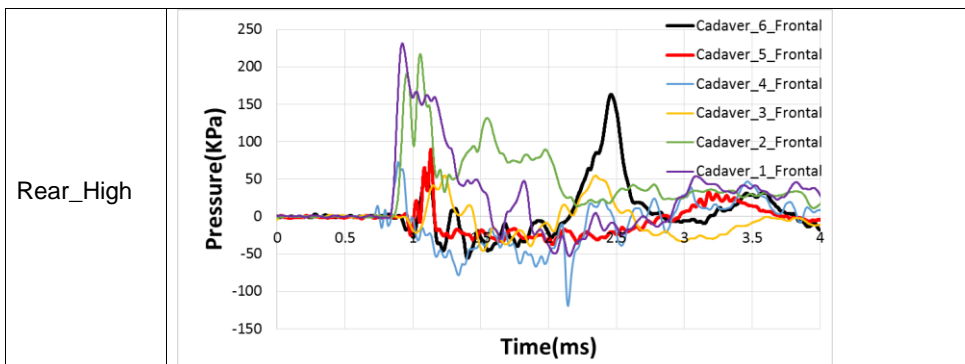
Frontal_Low	
Frontal_Med	

60

Frontal_High	
Lateral_Low	
Lateral_Med	

Lateral_High	
Rear_Low	
Rear_Med	

Rear_High	

Publications

Since the blast testing of cadavers was completed shortly before the end of the contract, we have just started preparing a manuscript for journal publication. The paper will acknowledge the support of MRMC

TASK III REPORT

Task III - Develop and validate a computer model of the pig brain simulating the effects of a blast over-pressure

1. Introduction

Many researchers [1,2-4] have performed computational simulations by generating blast waves using various FE codes to correlate the injuries in the brain to intracranial biomechanical responses, such as the peak pressure, stress, and strain in the brain. However, the output of these models was primarily compared with blunt impact data [5, 6] while the validation of these models against blast related experimental data was limited. For those researchers who validated their FE surrogate models against pressure data obtained from blast related experimental studies [7-10], they all use data obtained from shock tubes. Although the magnitude of the peak incident pressure in shock tube experiments could be similar to open field tests, the durations in some of shock tubes are longer [11, 12]. For those shock tubes that produced short blast durations [13, 14] which are comparable to open field blasts, the allowable animal size is generally limited to rats. To acquire data from bigger size surrogates, such as the anesthetized pig or human cadaver, the diameter of shock tube has to be increased significantly. However, the cost of doing a large diameter shock tube test was comparable to open field test. Yet, limitations related to running a shock tube test remain. Therefore, it is more appropriate to validate the surrogate models in open field blast conditions so that the true relationship between the input parameters (such as incident pressure) and the biomechanical responses (such as intracranial pressure (ICP)) can be studied.

Singh et al. [15] used an FE model, which was validated against cadaveric data obtained from shock tube loading conditions [16], to simulate the intracranial responses due to an open field blast. The input conditions were taken from those measured using a Hybrid III dummy subjected to an open field test [17]. The intracranial responses reported in the Singh's study were not directly compared with those obtained from open field blast tests. For this reason, it can be stated that no FE models have been directly validated against open field blast tests data. The main reason might be related to a lack of published biomechanical responses obtained from open field blasts.

Recently, researchers at Wayne State University (WSU) performed open field blast tests on 5 instrumented miniature Yucatan pigs (age 6-8 months, weight 50-60 kg). Before, during, and after the blast test, each pig was anesthetized and monitored carefully by certified veterinarians. Each pig was instrumented with six intracranial pressure sensors (Kulite, CA, XCL-072-100A) at different locations in the brain. During the test, the pigs were oriented in a front to back direction and the snout of the pigs were supported by two webbing straps to minimize the head motion. The incident pressure in the air was measured using pencil transducers (PCB Piezotronics, 137B22B) located at the same distance from the charge as the surrogate's head. All data were recorded using a DEWETRON (DEWETRON Inc, RI, USA) data acquisition

system at a sampling frequency of 1 megahertz using the DEWEsoft (SIRIUS, Dewe Soft LLC., OH) software. The data were further filtered at 10 kHz, using a low pass filter. Further details of the experimental study can be found in another publication [18].

Eight pounds (3.6 kg) of C4 were used to produce the incident shock wave with an abrupt pressure rise and exponential-like decay Friedlander wave. To minimize the effect of ground reflection, the height of the triple point for this 3.6-kg charge was calculated, in accordance to that reported by De Rosa et al. [19], to be between 0.8 and 0.9 m. As such, the height of the test subjects and charge weight was both set at 0.9 m. To achieve the three nominal peak incident pressure levels of 150, 300, and 400 kPa, the standoff distance for each pressure level was calculated to be 4.6, 3.6, and 3.1 m, respectively.

The purposes of this study were to develop a FE model of the head of an average weight Yucatan pig and to validate the biomechanical responses obtained from the numerical model against measured data obtained from open field blast experiments.

2.   Materials and Methods

Development of an FE model of a Pig Head

MRI images of the head of a 55-kg anesthetized Yucatan swine were obtained from the WSU medical school imaging center under a research protocol that was reviewed and approved by the Institutional Animal Care and Use Committee at WSU and the USAMRMC ACURO. The image resolution was 1.5 X 1.5 X 1.0 mm. The entire data processing procedure (shown in Figure 1) consisted of the following steps: image registration, image processing, three-dimensional (3-D) geometry generation, 3-D geometric shaping, and FE mesh development. The images were imported into MIMICS (version 13.0., Materialise, Leuven, Belgium) for co-registration in order to translate the images from different modalities into the same global coordinate system. After this step, the geometries of interest were isolated through a combination of thresholding techniques for certain densities of bone or soft tissues using the image pixel value (intensity). This operation was repeated layer by layer until the 3-D geometry of the whole pig head was obtained. Different colors were assigned to each anatomical part such as the skull, brain, or spinal cord in the pig brain, which are called masks as shown in Figure 1. Once the initial geometric modeling was completed, a re-shaping technique was used to ensure that the model surface could meet the meshing criteria. Three-dimensional geometric shaping primarily involves the process of smoothing a surface in an effort to create an ideal surface for automated meshing algorithms, which use mesh projection-based methods. The smoothing algorithm (the 3-matic module within Mimics) ensures that the total volume loss between smoothed and original version was less than 5%, and there were no visible changes in the geometry observed after applying the smoothing algorithm. Finally, the smoothed surface was imported into ANSYS ICEM CFD (Dassaults Systems, USA), a pre-processor based on a multi-block meshing scheme aimed at hexahedral mesh generation. The multi-block technique [20] is based on rules for geometrical grid-subdivisions (i.e. 'blocks') and mapping techniques, producing hexahedral elements in the 3-D space. Further, the element

quality of the generated mesh was refined through Hypermesh 12.0 (Altair, Troy, MI). The whole model consisted of 252,836 hexahedral solid elements. The average size of
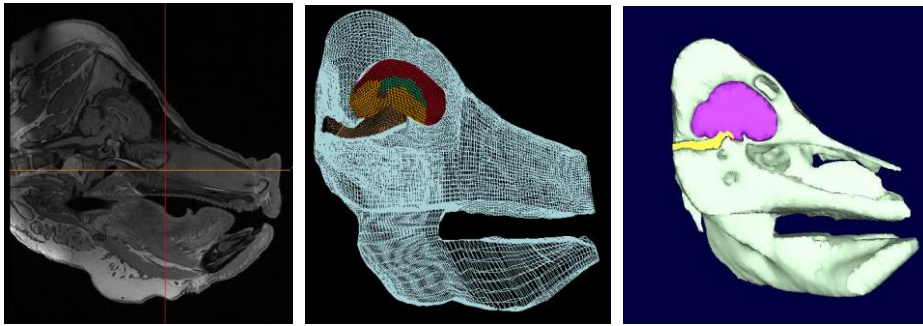
(a)   (b)   (c)
Figure 1. Image processing seqence for the development of the pig head model: Image registration (a), CAD model generation (b), and FE mesh generation (c).

the mesh of the elements was found to be 1-2 mm. Different adjacent tissues within the pig brain, such as the cortex, corpus callosum, mid brain, skull, etc. were modeled with elements sharing the common nodes.

Material properties of the pig skull and brain tissues were taken from published modeling literature [21, 8] and are shown in Table 1. The skull was modeled with one point reduced integration elements with elastic properties, while different parts of the brain, such as the corpus callosum, pineal gland, etc., were modeled with the same type of elements having the same viscoelastic properties.

Table 1 Material model parameters for different parts of a pig head

Part	Bulk modulus (GPa)	Shear Modulus (kPa)		Time decay constant (/s)
		Short term	Long term	
White matter	2.19	10.4	2.9	50
Grey matter	2.19	8	2.9	50
	Density (kg/m^3)	Elastic modulus (GPa)		Poisson's ratio
Skull	2000	12		0.22

Modeling of Open Field Blasts

The physics of blast waves is well known and has been successfully incorporated into general purpose non-linear FE codes such as LS-DYNA (LSTC, Livermore, CA). An

ideal blast wave, often termed a Friedlander wave, is characterized in part by the absence of wave reflections from the surrounding. These blast waves can be modeled using tools such as CONWEP (CONventionalWEaPons) or MMALE (multi-material arbitrary Lagrangian-Eulerian) in LS-DYNA. Many researchers [9,15, 22, 23] have used this technique for modeling blast waves and fluid-structure interactions with the help of explicit codes.

Complex equations of state (EOS) are used to represent different explosives [24]. To model the 3-D air space between the explosive and the pig's head requires a large number of 3-D elements and to model the propagation of the blast wave in 3-D through air is computationally time consuming, rendering the model very costly to run. A less costly method would be to model the transit of the shock wave in air in 2-D first using ALE2D elements for both the air and the explosive before mapping the 2-D information to 3-D. The air domain was modeled with *NULL material and the simple polynomial equation of state (EOS). The C4 explosive was modeled with *MAT_HIGH_EXPLOSIVE_BURN and the JONES_WILKINS_LEE (JWL) EOS. The simulation setup for the 2-D air domain is shown in Figure 2.
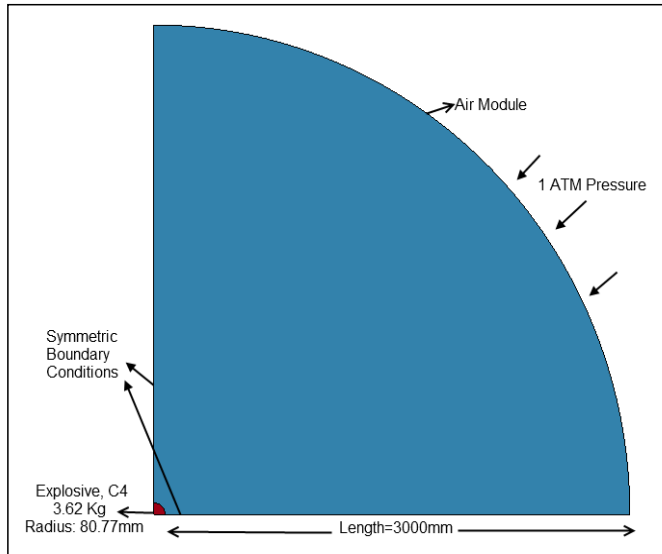
Figure 2. Simulation setup of the 2-D air domain

In this study, a linear polynomial EOS was used to model the behavior of air. Using this method, the pressure P is defined as a function of internal energy per unit volume, E,

$$P = C_0 + C_1\mu + C_2\mu^2 + C_3\mu^3 + (C_4 + C_5\mu + C_6\mu^2)E,$$

where C_0, C_1, C_2, C_3, C_4, C_5 and C_6 are constants, and

$$\mu = \frac{\rho}{\rho_0} - 1,$$

where, ρ=current density and ρ_0= initial density.

The JWL EOS defines the pressure P as a function of the relative volume V, and internal energy per unit volume E, which can be written as

$$P = A\left(1 - \frac{\omega}{R_1 V}\right)\exp(-R_1 V) + B\left(1 - \frac{\omega}{R_2 \omega}\right)\exp(-R_2 V) + \frac{\omega}{V}E$$

where A, B, R_1 and R_2 are the constants that depend upon the characteristics of the explosive used.
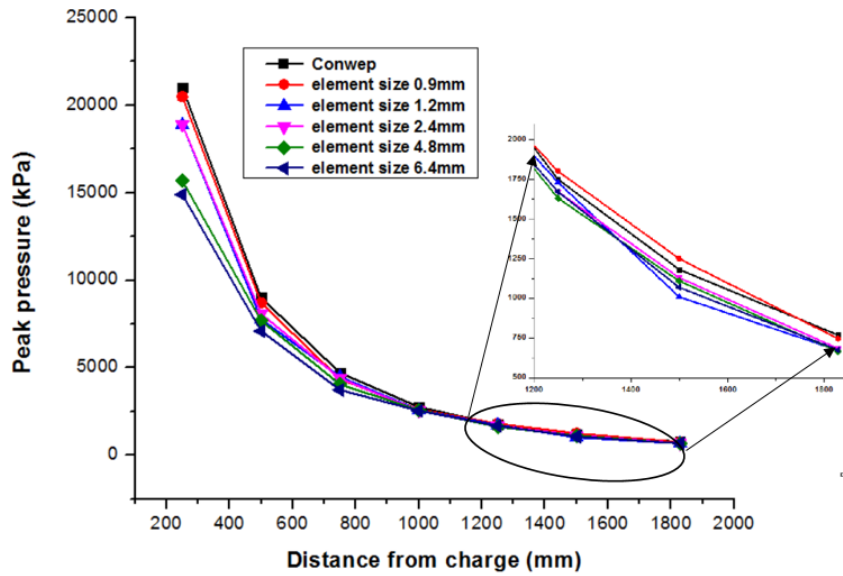
Figure 3. Comparison of the simulation results and CONWEP calculated peak pressures at associated distances for different mesh size FE models

A mesh sensitivity study was performed to determine the minimal size of the elements in the air domain needed to match the model predictions with the theoretical calculation using CONWEP. Figure 3 shows the pressure-distance curves when different mesh

sizes (6.4, 4.8, 2.4, 1.2, and 0.9 mm) FE models were used. From this sensitivity study, the element size of 0.9 mm was found to be suitable for modeling peak pressures from 0.2 to 1.85 m. The peak static overpressure and the duration are in good agreement with the theoretically calculated blast incident pressure from CONWEP at the end of 2-D mapping. The pressure wave transmission in the 2-D air domain is shown in a sequence of images taken at different times in Figure 4.
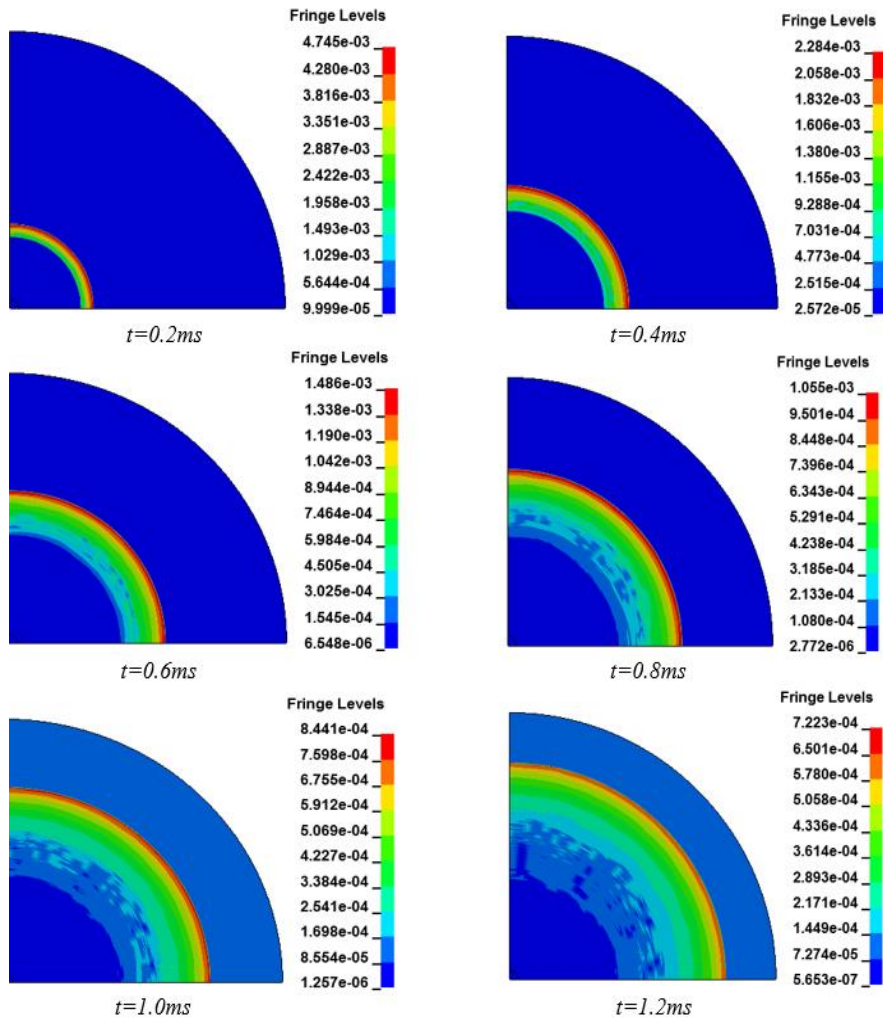
Figure 4. Pressure contour of the blast wave in the air domain at different time points.

In the LS-DYNA FE solver, the keyword *INITIAL_DETONATION defines the location where the explosive is detonated. Different values selected for parameters needed to model the EOSs of the air and explosive were taken from the published literature [25], as shown in Table 2. After verifying the 2-D model against theoretical results, a 2-D to 3-D mapping technique was used to form the 3-D air mesh. Figure 5 shows the 2-D and 3-D air pressure domains at the end of this air transit phase.

Table 2: Material models and EOS for explosive and air from LS-DYNA cards

Component	UNIT SYSTEM (kg, mm, ms)						
Air	*MAT_NULL						
	RO	PC	MU	TEROD	CEROD	YM	PR
	1.13E-09	0	0	0	0	0	0
	*EOS_LINEAR_POLYNOMIAL						
	C0	C1	C2	C3	C4	C5	C6
	0	0	0	0	0.4	0.4	0
	Eo	VO					
	2.50E-04	1					
Explosive	*MAT_HIGH_EXPLOSIVE_BURN						
	RO	D	PCJ	BETA	K	G	SIGY
	1.60E-06	8193	28	0	0	0	0
	*EOS_JWL						
	A	B	R1	R2	OMEG	E0	VO
	609.772	12.95	4.5	1.4	0.25	9	1

Where *RO* =Density, *PC = Pressure cutoff, MU = Viscosity coefficient, TEROD = Relative volume for erosion in tension, CEROD = Relative volume for erosion in compression, YM = Young's modulus, PR=Poisson's ratio, C0- C6= Equation of state coefficients, Eo = Internal energy, VO=Initial relative volume, D=Detonation velocity, PCJ=Chapman-Jougat pressure, BETA= Burning factor, K = Bulk Modulus, G=Shear modulus, SIGY=Yield stress, A, B, R1, R2,OMEG- Equation of state coefficient, E0= Detonation energy per unit volume,*
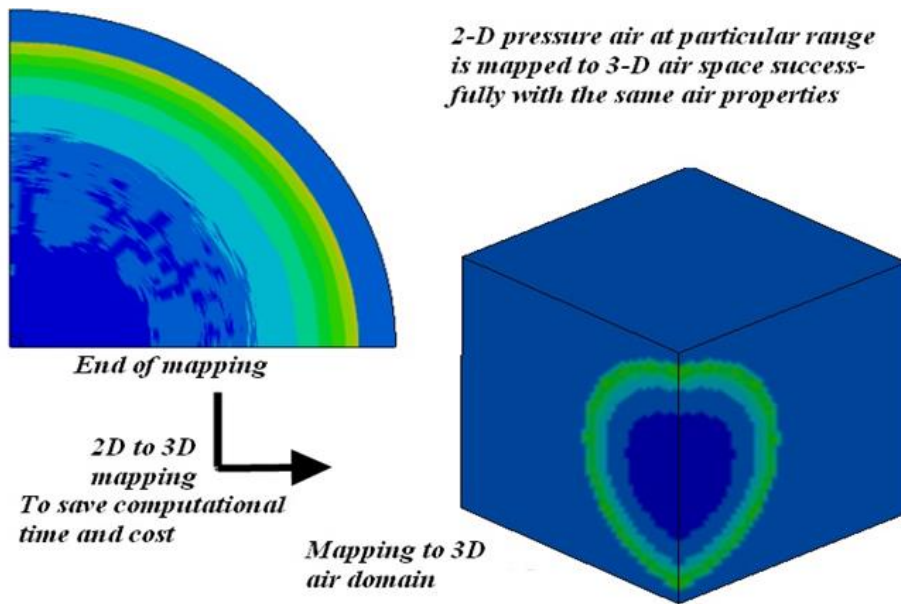
Integration of the Air Domain and Pig Head Model

The developed FE swine head model was integrated with the 3-D air domain mesh and the shock wave interaction with the swine head model was achieved through a fluid/solid coupling algorithm. The *CONSTRAINED_LAGRANGE_IN_SOLID formulation available in LS-DYNA was used to model the coupling between the shock wave and the simulated pig head. The same boundary conditions as defined by the

experiments were simulated (Figure 6). In the numerical simulations, ground reflections were not considered. This simplification was based on the fact that the placement of the explosive was carefully chosen in accordance with theoretical calculations that aimed at minimizing the ground reflection by adjusting the height of burst and the range. The locations where intracranial pressure sensors were present in the experiments were identified in the FE model and are shown in Figure 7. Four elements surrounding the pressure sensor locations were selected to calculate the intracranial responses from the simulations for comparison with experimental data.

Figure 5. 2-D to 3-D mapping

Integration of the Air Domain and Pig Head Model

The developed FE swine head model was integrated with the 3-D air domain mesh and the shock wave interaction with the swine head model was achieved through a fluid/solid coupling algorithm. The *CONSTRAINED_LAGRANGE_IN_SOLID formulation available in LS-DYNA was used to model the coupling between the shock wave and the simulated pig head. The same boundary conditions as defined by the experiments were simulated (Figure 6). In the numerical simulations, ground reflections were not considered, based on the reasons given in the previous section. The locations where intracranial pressure sensors were present in the experiments were identified in the FE model and are shown in Figure 7. Four elements surrounding the pressure sensor locations were selected to calculate the intracranial responses from the simulations for comparison with experimental data.
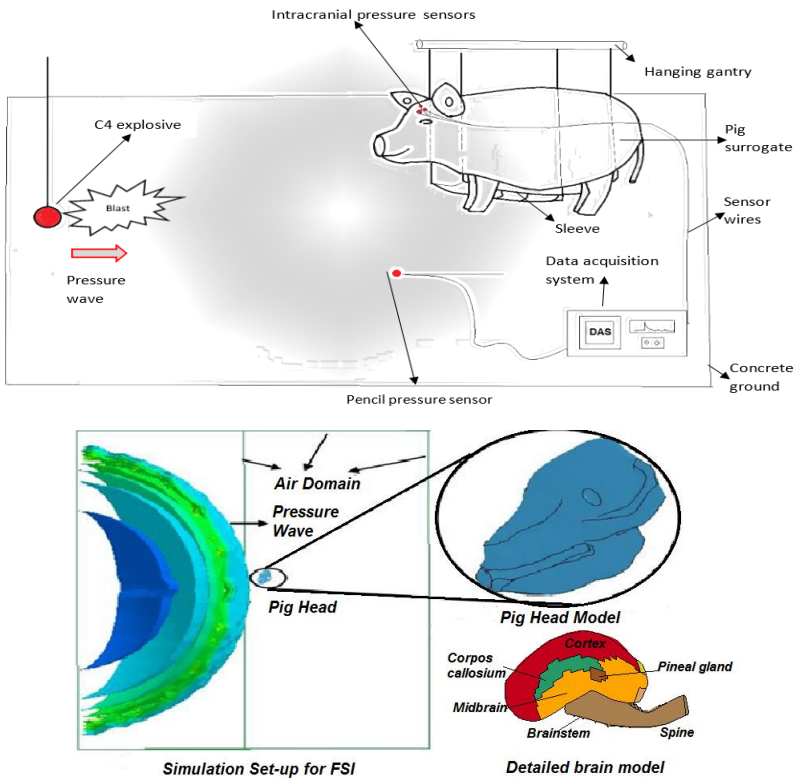
Figure 6. Experimental Setup (Top) and Simulation Setup (Bottom)
Please note the C4 explosive, pighead and pencil pressure sensor are at the same
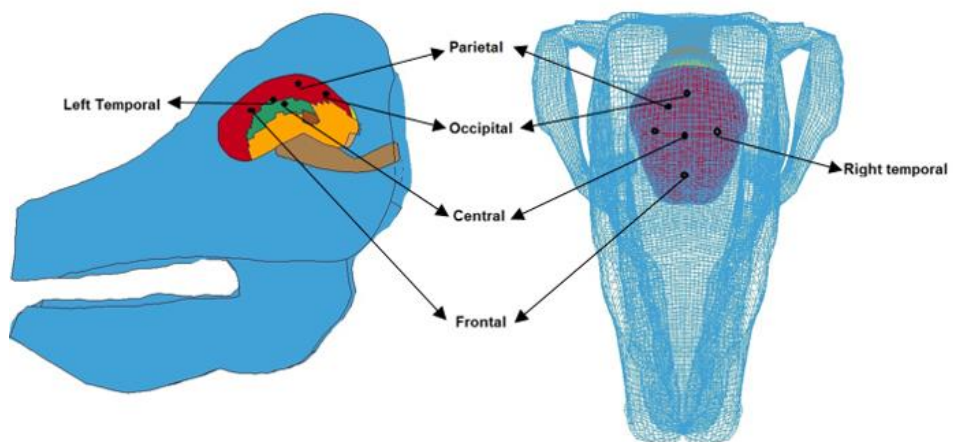height from the ground in the perspective view for the experimental setup (top figure)

Figure 7. Sensor locations inside the pig brain in the numerical model

3.   Results

Comparison of Computed and Measured Intracranial Pressures

Aside from validating the pressure time histories obtained by the MMALE simulations against theoretical CONWEP calculations at the prescribed ranges (Figure 3), comparisons of the incident pressure measured in the experiments and from the simulations were also conducted to ensure that the numerical surrogate experienced a similar incident pressure during numerical simulations. The incident pressure time histories for the simulations as well as those measured from the PCB air pressure sensor during the experiments are shown in Figure 8. The incident pressure in numerical studies for the high (Figure 8 (a)), medium (Figure 8 (b)), and low (Figure 8 (c)) pressure levels matched well against the experimental pressure profiles at the same three pressure levels, respectively. There were some small reflections presented in the experimental data as shown in Figure 8, while the simulation results did not have any of these reflections due to the lack of explicit modeling of surrounding infrastructures, such as the metal frames, etc. Table 3 compares the average peak incident pressures measured experimentally and that calculated from the simulation. All differences were less than 2.2%.

The model predictions, in terms of incident pressures and intracranial pressures (ICPs) at the frontal, central, occipital, right temporal, left temporal, and left parietal locations, are shown in Figures 9(a), 9(b) and 9(c) at different pressure levels using the same sampling rate as that used iexperimentally. In all simulations, the incident pressure exhibited a typical Friedlander waveform. Also, the peak ICP at the frontal location was

Table 3 Comparison of the experimentally measured and simulation results of incident pressures at the three preset pressure levels

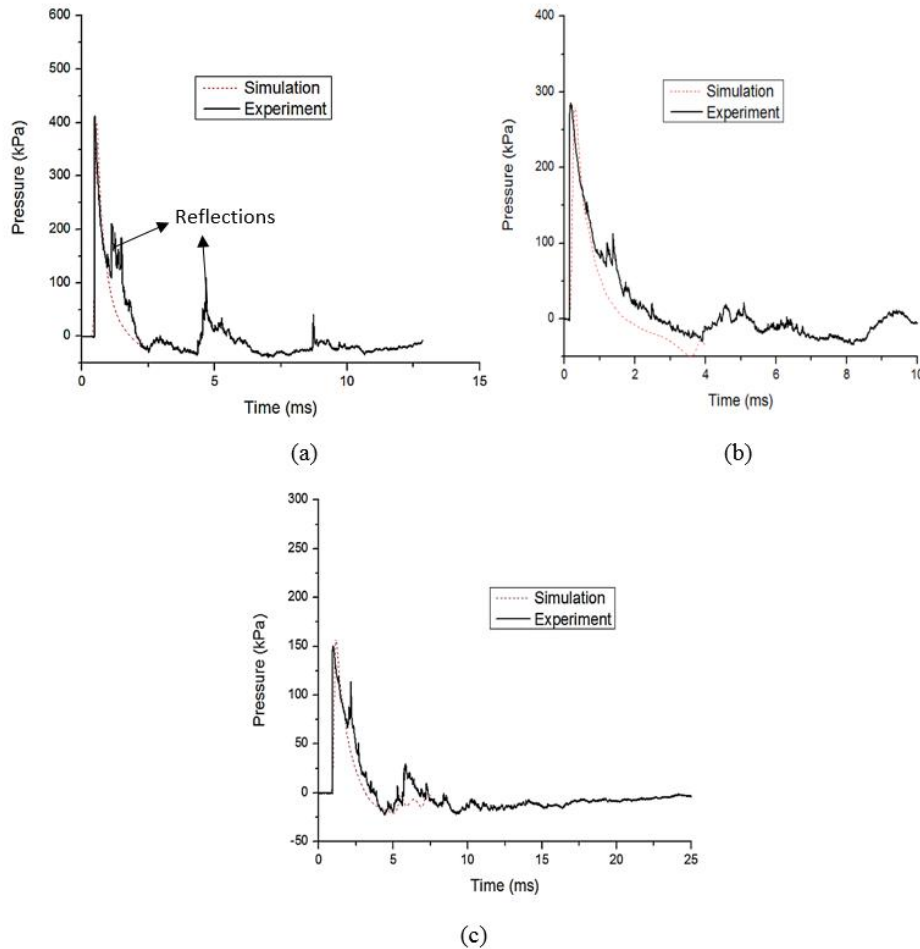| Incident pressure (kPa)			
Pressure Level	Experiment (Mean±SE)	Simulation	% Difference
Low	150.2±0.9	150	0.1
Medium	278.2±13.9	280	-0.6
High	409.2±18.9	400	2.2

Figure 8. Comparison of simulation results and experimentally measured incident pressure for the high level (400 kPa) (a), medium level (300 kPa) (b), and low level (150 kPa) (c) of blast.

always higher than the peak incident pressure for all simulations. Contrary to theoretical solutions, the experimentally measured ICP at the occipital location did not become negative. This is probably due to the technical difficulties of inserting the occipital sensor into the pig brain at its interface with the occipital bone because of the relatively thick skull and neck at the posterior region of a pig head. As a result, this sensor was placed within the occipital lobe but not at the posterior edge of the occipital lobe.
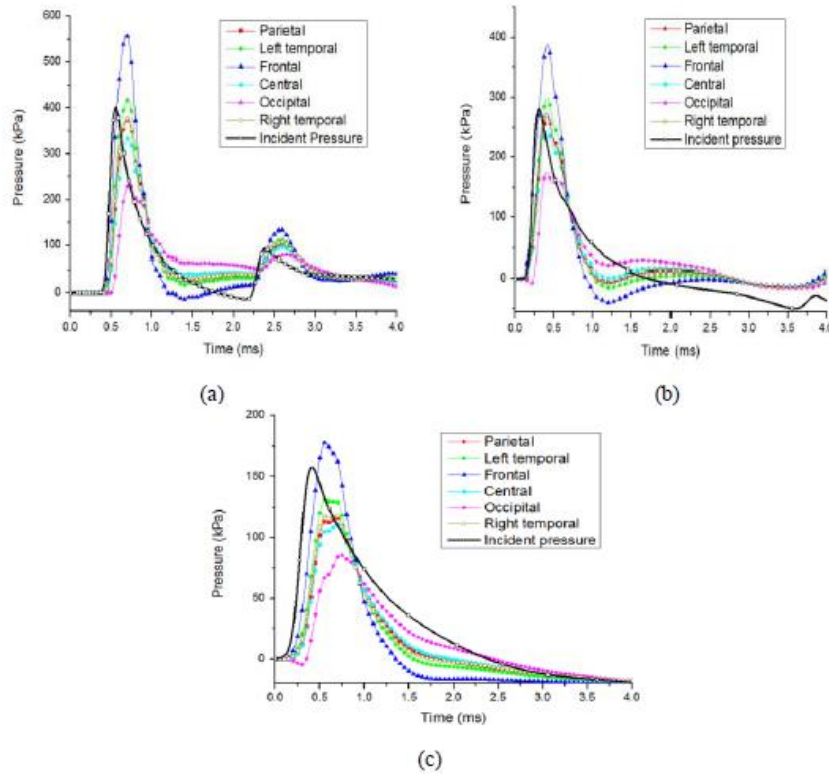
Figure 9. Simulation intracranial pressure results at different sensor locations for the high level (400 kPa) (a), medium level (300 kPa) (b), and low level (150 kPa) (c) of blasts

The intracranial pressure histories from the simulations were further compared with experimental measurements. The comparison of intracranial pressure time histories at the central, frontal, right temporal, left temporal, parietal, and occipital locations for the medium level of blast is shown in Figure 10. Although not shown, similar simulation results and experimentally measured pressure time histories were obtained for the high as well as low levels of incident pressure. Additionally, the peak simulation results and the experimentally measured ICPs at the frontal, parietal, central, right temporal, left temporal, and occipital locations for all three incident pressure levels are shown in Figure 11. The numerical simulations over predicted the frontal pressures while the ICPs at other locations seemed to have reasonable agreements with the test data for

76

the peak values, but not the decay phase. It was also observed that all simulated ICPs had a linear relationship with respect to the incident pressure with an R^2 value greater than 0.98. Quantitative comparisons between the experimentally measured and peak ICPs results from the simulations are shown in Table 4. Considering the large variations seen in experimentally obtained ICPs, it is believed that the peak ICP values obtained from the simulation agreed reasonably well with experimental data.
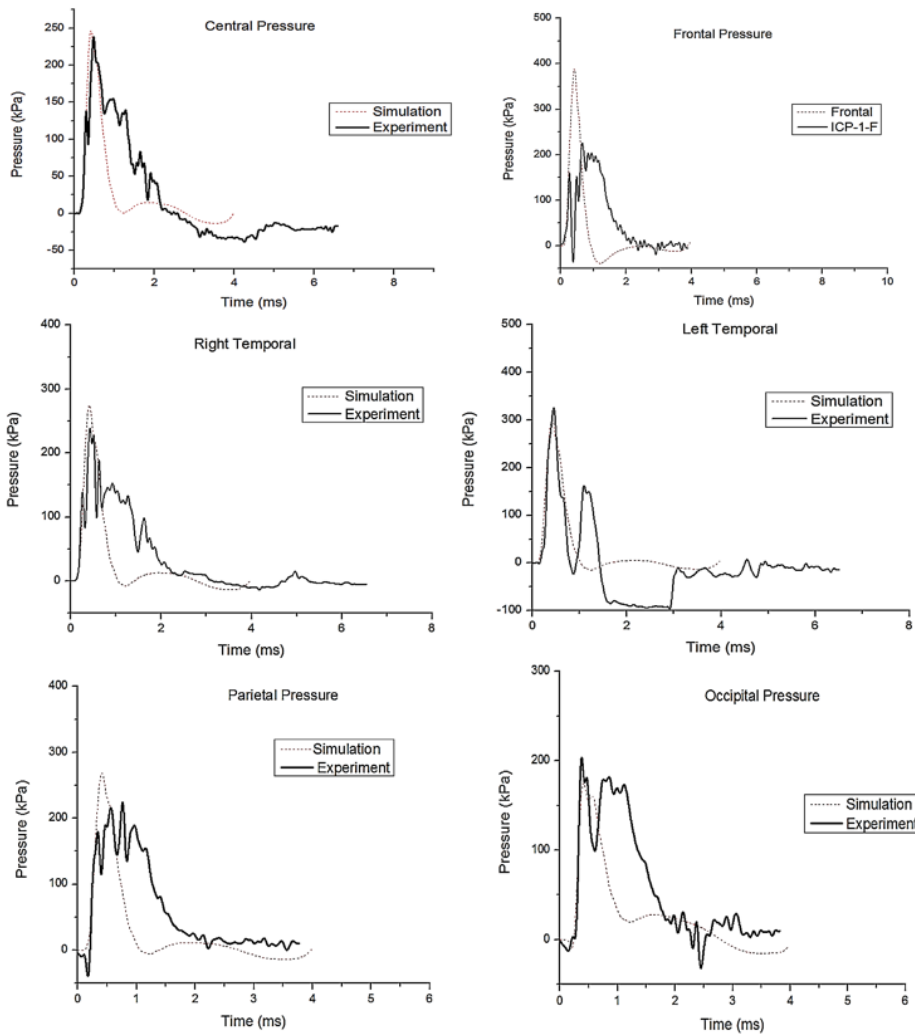

Figure 10. Comparison of simulation and experimentally obtained intracranial pressure time histories for the medium level (300 kPa) of blast

Table 4 Comparison between experimentally measured and peak intracranial pressure values obtained from simulation. All units are in kPa

Location	Central			Frontal			Right temporal		
Test	Experiment (Mean±SE)	Simulation	% Difference	Experiment (Mean±SE)	Simulation	% Difference	Experiment (Mean±SE)	Simulation	% Difference
Low	93.7±17.0	115	-22.7	97.6±19.7	182	-46.4	147.9±0.0	123	16.8
Medium	228.1±29.5	246	-7.8	236.5±30.7	389	-64.5	253.1±46.8	272	-7.5
High	327.2±17.0	334	-2.1	311.7±29.1	558	-79.0	325.5±8.6	376	-15.5

Location	Left temporal			Parietal			Occipital		
Test	Experiment (Mean±SE)	Simulation	% Difference	Experiment (Mean±SE)	Simulation	% Difference	Experiment (Mean±SE)	Simulation	% Difference
Low	142.8±0.0	137	4.1	144.2±18.0	121	16.1	78.9±13.4	90	-14.1
Medium	281.6±35.0	299	-6.2	276.0±62.4	268	2.9	209.1±34.5	175	16.3
High	386.4±7.1	417	-7.9	414.6±0.0	377	9.1	328.2±26.7	232	29.3
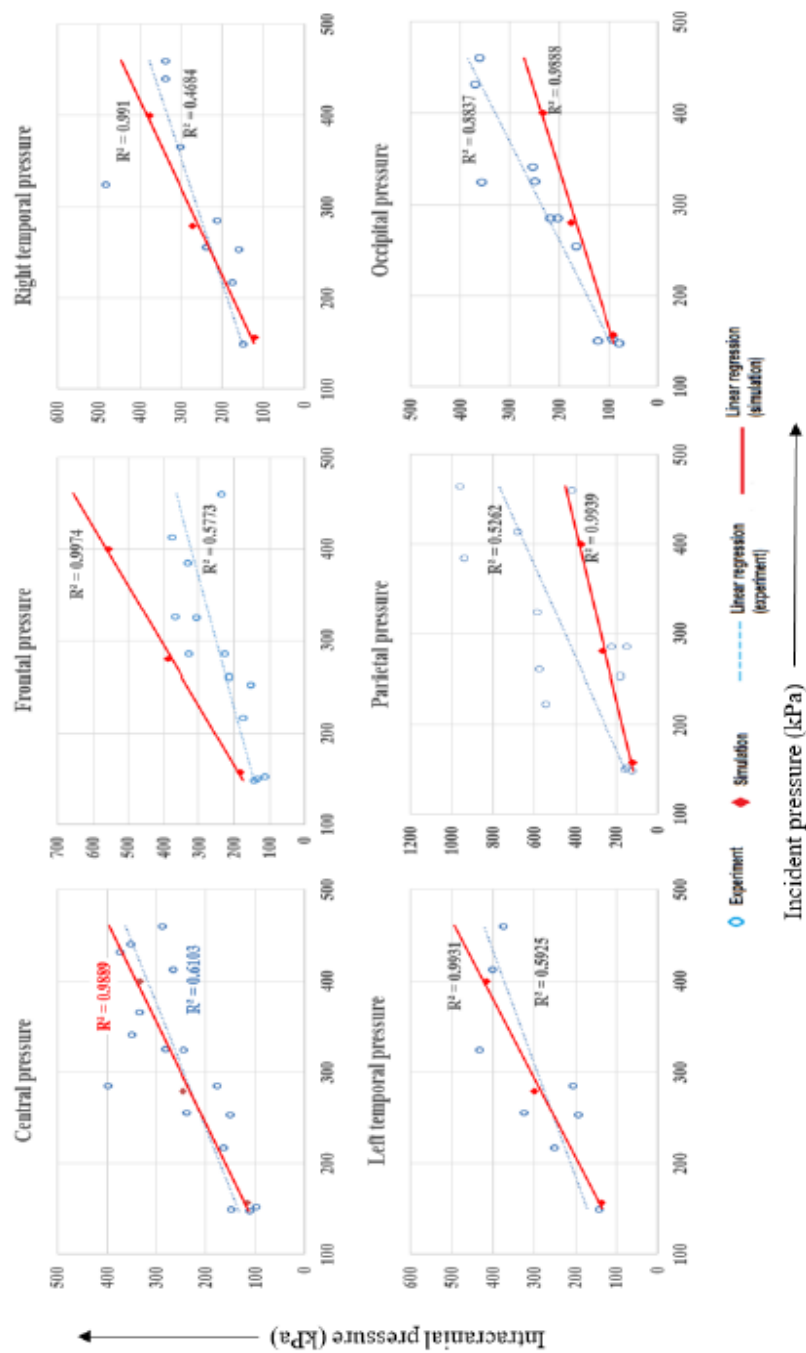
Figure 11 Peak ICP values obtained from simulation at different brain locations (diamond shaped) versus experimentally measured ICPs (empty circle) as a function of the incident pressure which is on the abscissa, in units of kPa.

79

Computed Strain Values in the Swine Brain

The swine model was used to compute the strains developed in the brain due to blast overpressure. The maximum values were found to be at the skull-brain interface. Inner elements in the brain were not highly strained and their values were limited to 0.5-3% from low preesure to higher pressure cases in these elements. The strain contours at a representative instant of time for the three pressure levels are shown in Figures 12-14. The main reason for higher strain to be on the brain outer boundary elements might be due to the nodal connection between the very stiff skull material and the relatively soft brain material. In the current model, the interface between brain and skull was simulated by a nodal connection which may not represent the physical nature of this connection. Further efforts are needed to simulate the connection between skull and brain in the numerical models.
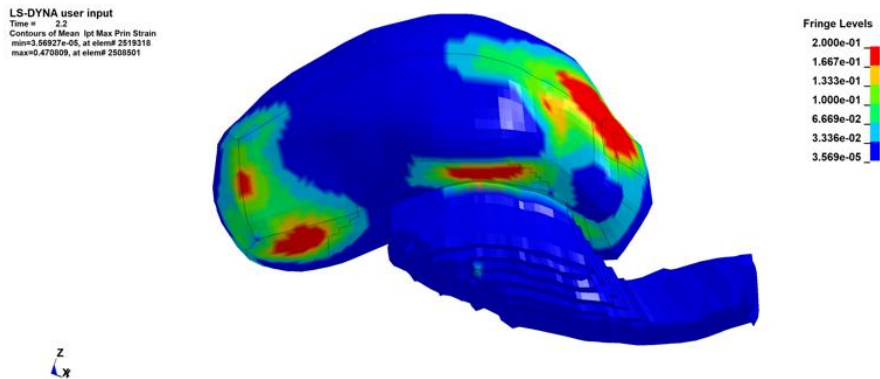
Figure 12. Maximum principal strain contour for the high pressure
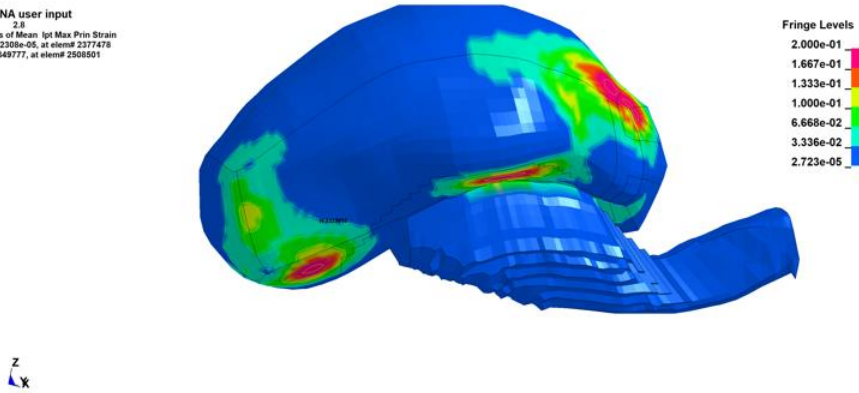
Figure 13. Maximum principal strain contour for the medium pressure
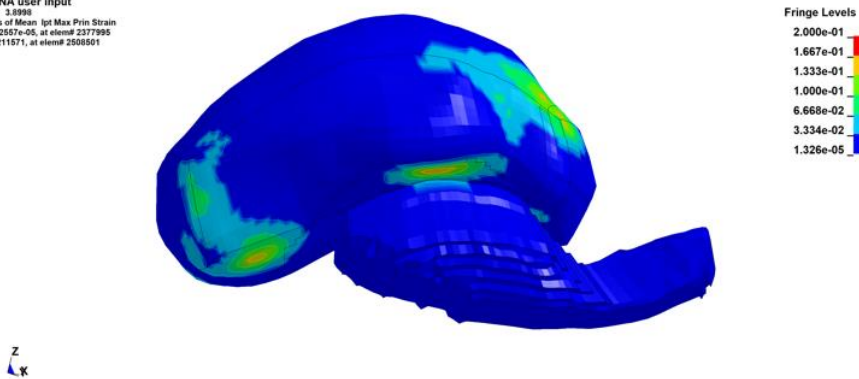

Figure 14. Maximum principal strain contour for the low pressure

Please note that in the contour plots for all pressure levels, the maximum strain threshold was taken as 0.2 or 20% and the corresponding dark red contours represent element strains above 16.67%. Further, the maximum strain histories at the corresponding element for each case are also plotted in Figure 15.
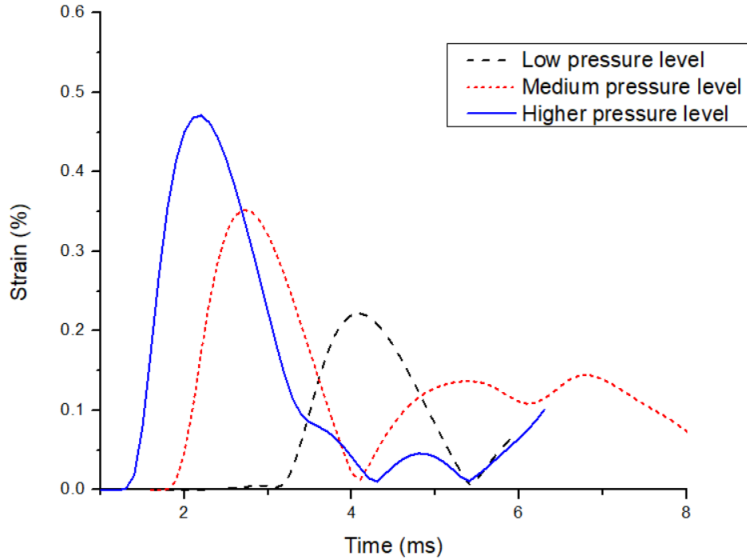
Figure 15. Maximum principal strain histories for highest strain element for each pressure level

4.   Discussion

Intracranial pressure showed an increasing trend with respect to the incident pressure in both the experimental data and the simulation results, as shown in Figure 15 The simulation results were highly linear with all coefficient of determination (R^2) greater than 0.98. This result is expected due to the use of a linear viscoelastic material law to represent the brain and an elastic material for simulating the skull. In reality, the behavior of the brain tissue is non-linear, strain rate dependent, and directionally variant in nature [26, 27]. Moreover, measuring ICPs with high accuracy might be problematic, because sealing of the skull after sensor insertion could never be as good as that for an intact skull. Additionally, simulation results are calculated from theoretical equations with the simplified boundary conditions. On the other hand, experimental results included those variations due to reflections from surrounding structures needed to support the pig that were not considered in the simulation. These reasons may explain the lack of reproducibility issues as seen in the experimentally measured peak values shown in Figure 11.

Also, the simulation results showed that the numerical simulations over predicted the peak ICP at the frontal location by 46%, 65%, and 79% for the low, medium, and high incident pressure levels, respectively. As the blast wave travels through the brain from the frontal to the occipital region, the peak pressure magnitude continues to decrease. The low experimentally measured frontal ICP could be due to the reasons listed below.

82

Multiple frontal sinus chambers are located within the frontal region of a pig's skull where the skull bones are the thinnest compared to other regions, and there is a significant downward slope present (Figure 16) [28]. Normally, the pressure in these air filled (or occasionally fluid filled) cavities is lower than that of the ICP. Unfortunately, the integrity of the skull needs to be compromised in order to install the ICP pressure sensor. As a result of this experimental preparation procedure, the measured ICP may be affected by two potential mechanisms. First, an air passageway is created between the brain and frontal sinuses. Although careful sealing of the skull is ensured, no attempt was made to seal the boundary between the brain and sinus chambers. Second, the fluid filled sinuses may entrap some air bubbles within the chambers. Both mechanisms could serve to lower the measured ICP.

To validate the existence of sinus cavity, a pig head was dissected from the neck with skin and muscles still intact. From this, an intact and clean skull was harvested by thoroughly removing the skin and the surrounding soft tissues. Further, a diamond saw was used to cut the skull along the mid sagittal plane as shown in Figure 17. The presence of a sinus cavity can be clearly seen to the left of the frontal sensor location (Figure 17B).

Therefore, a series of parametric studies was conducted with different boundary conditions at the central region of the pig head. Three cases were considered: (1) both the skull and brain were intact; (2) the skull had a small opening while the brain was intact; and (3) the brain had a small hole on the surface while the skull was intact. Case 2 was intended to study the effect of an unsealed hole in the skull at the sensor location at the nasal cavity location. Case 3 was used to simulate a trapped air bubble between the skull. The sketches of Cases 2 and 3 are shown in Figure 18. The holes were
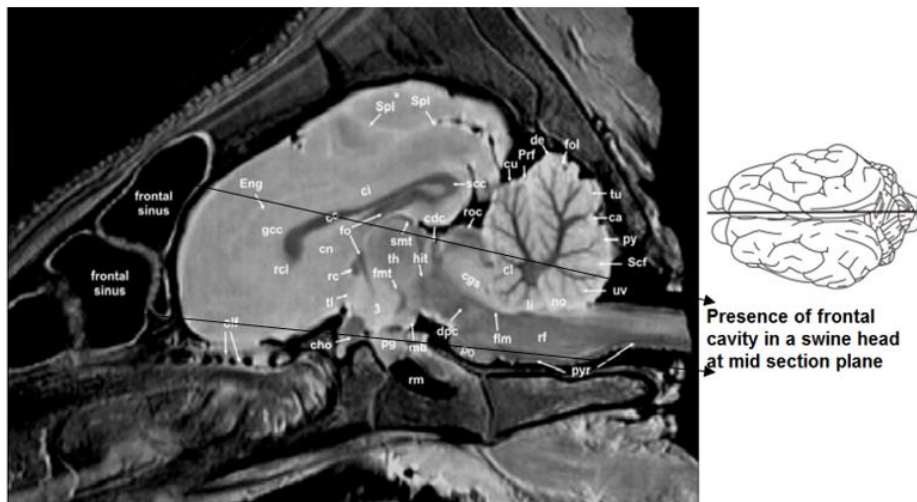

Figure 16 Lateral view of pig brain showing frontal sinus (Reproduced from Schmidt et al. (2014).

Figure 17 (A) A snapshot showing the locations of installed mounts for pressure transducer installation and (B) A sectional view of a skull which shows the frontal sinus cavity along with corresponding frontal sensor location.

simulated by removing some of the elements in the skull or brain. The peak pressures calculated from the simulations at the frontal sensor location of the brain for all three cases are plotted in Figure 19. It can be seen that in Case 1, the peak ICP at the central brain is higher than the peak incident pressure by about 25%. An opening on the skull (Case 2) slightly decreased the ICP, and a significant pressure drop could be observed when a bubble exists on the surface of the brain (Case 3). The low experimentally measured pressure of 311 kPa as shown in Table 4 for the frontal location is likely due to the presence of entrapped air bubbles.
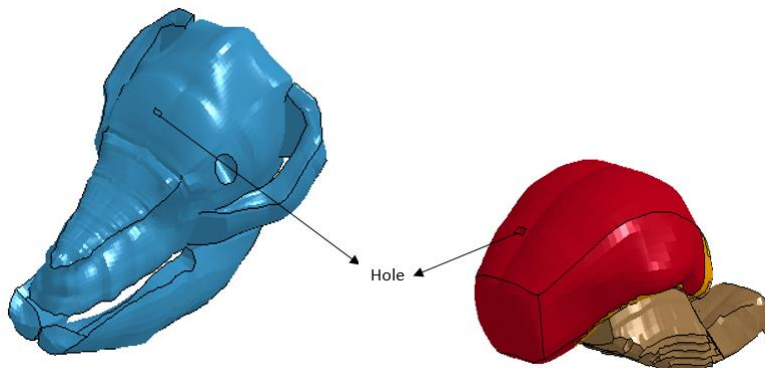

Figure 18 Simulations with openings on the skull and brain: (left) the skull has a small opening while the brain is intact; (right) the brain has a small hole on the surface while the skull (not shown) is intact
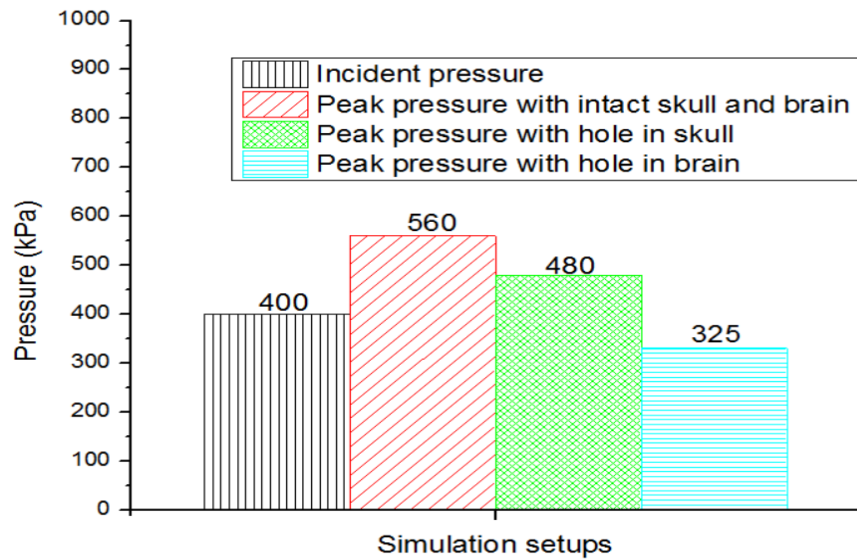
Figure 19 Comparison of ICP values obtained from the simulation in all three cases: 1) both the skull and brain are intact; (2) skull has a small opening while and brain is intact; and (3) brain has a small hole on the surface while the skull is intact

Upon reviewing Figure 8, it is seen that there are reflections in the experimental data that could not be simulated in the current setup. These reflections are more than likely due to interactions of the blast wave with the surrounding structures that were captured by the sensors. The simulation results matched very well the rising portion of the Friedlander wave as well as the peak value along with the initial decay in the curve. However, due to reflections in the later stage of the decay curve, the simulation curve partially deviated from the experimental curve. The corresponding reflections seen in the incident wave also affected the shape of the ICP curves as shown in Figure 10.

Similar to the incident pressure curve, the intracranial pressure curves at various locations inside the brain matched the initial rise and peak values, with the exception of those simulated at the frontal location. But the decay portion of the experimental curve had reflections which could not be simulated well. The reason for the mismatch in duration between the experimentally measured and simulation result shown in Figure 10 is unknown, although it is suspected that this phenomenon may be related to the reflections captured by the sensor. More research is needed in order to better understand the reasons for this mismatch.

It is worth noting that the sensor location plays a major role in intracranial pressure response measurement. For example, the sensor at the occipital location did not show

any negative pressure or contrecoup scenario during the experiment. One of the reasons is due to the difficulties in inserting the sensor into the rear edge of the brain near the skull, due to the thick neck and skull at the posterior end of the pig's head. While the blast instrumentation used in this study captured the majority of the blast energy transmitted into the test subjects, it is recognized that the best currently available sensors used in the experimental study may not be sufficient for capturing all parts of the blast data. We believe that this deficiency may explain part of the inconsistencies we observed in the experimental data. Although the results obtained from the current study are reasonably acceptable, future improvements in instrumentation and data acquisition system may provide better and more consistent data for model validation. Aside from instrumentation issues, variations in the specimen position and orientation, sensor mounting, sensor location, etc. may also cause inconsistent test results that are not addressed in our numerical simulations.

Because the experimental data varied significantly (Figure 11) due to the various reasons stated above, comparing the experimentally obtained time histories with model predictions cannot be easily done. Additionally, multiple losses of pressure sensor data were experienced during the testing due to the violent nature of the blast experiments. Therefore, to show the similarities and differences between the experimental and numerical results, the simulation responses were plotted against a single set of data (Figure 10) rather than average values or a corridor. The pressure time histories plots show the similar nature of responses retrieved through the numerical model as in experiments.

Additional computational studies were conducted to determine the effect of varying sensor locations. In these cases, the pressure sensors were moved to a very frontal location (near the front - approximately 10 mm anterior to the frontal sensor location in the experiments) and a very posterior location (rear end - approximately 10 mm posterior to the occipital sensor location in the experiments) as shown in Figure 20. The ICPs values obtained from these simulations demonstrated the coup and contrecoup phenomena (Figure 21), just like those seen in blunt impact conditions, within the first 2 ms after the shock wave reached the pig head. The ICP time history curves for all three blast levels at both extreme locations (A' and B') are shown in Figure 22. Further, comparisons of the simulated ICPs were made between sensor locations at A and A' and at B and B' as shown in Figures 23 and 24, respectively. From these figures, it is clear that a higher peak pressure is found at a frontal location near the brain-skull interface (corresponding to A' position) compared to the original location (A). On the other hand, the pressure at a far rear end location (B') is lower than the original sensor location (B). The higher pressure at the front end, close to the skull, was due to the impedance mismatch between the skull and brain. Because the speed of sound in the skull is much higher than that in the brain, the pressure is higher in the skull compared to that in the brain. Hence, the intracranial pressure near the skull-brain interface is higher than that calculated at the location that is away from the interface.

These results suggested that there is a greater possibility of sustaining injury in the region close to the skull-brain interface at the frontal location, because higher ICPs were correlated with elevated levels of bio-markers that are supposed to indicate BINT in another study [29]. Also, the lower negative pressure at the rear end position (corresponding to B' position) shows a contrecoup phenomenon at the rear end of the brain.

Along with pressure, researchers have used stress and/or strain as injury thresholds in BINT, but it was not possible to measure the stress or strain experimentally. Therefore, the calculated strain values were not validated. This is one of the major limitations of the current study. Although the pressure responses inside the pig brain were broadly validated, we can use the model to correlate different biomechanical parameters such as the shear stress, principal and shear strains, with injuries based on histological data. These tissue level biomechanical parameters have been previously proposed as relevant biomechanical indicators for coup-contrecoup injury and mild traumatic brain injury (mTBI) [30, 31] in automotive impacts. Future efforts will be made to correlate region-specific biomechanical response parameters with injured locations to be obtained from our histological study.
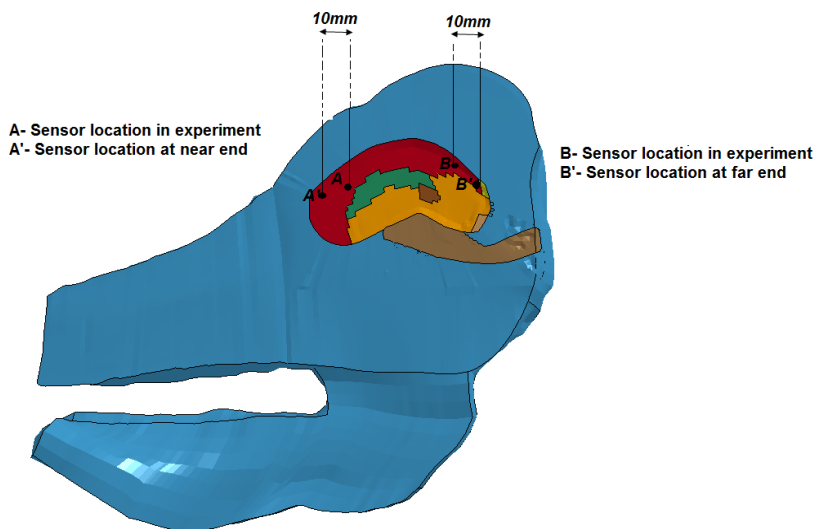

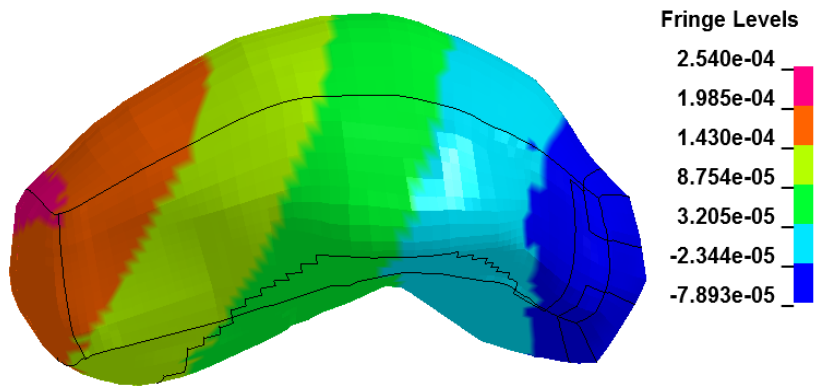Figure 20 Additional sensor locations selected to study the coup and contrecoup phenomena

Fringe Levels

2.540e-04	
1.985e-04	
1.430e-04	
8.754e-05	
3.205e-05	
-2.344e-05	
-7.893e-05	

Figure 21 Coup and contrecoup phenomena at the 400 kPa incident pressure level (The fringe units are in GPa)
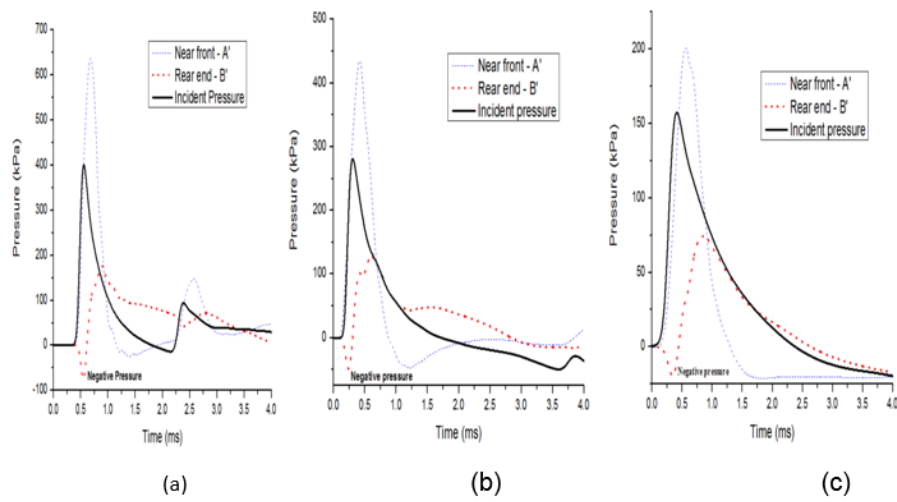

(a)   (b)   (c)

Figure 22 Intracranial pressures at the far front and rear ends of brain at the high incident pressure level (a), medium incident pressure level (b), and low incident pressure level (c)
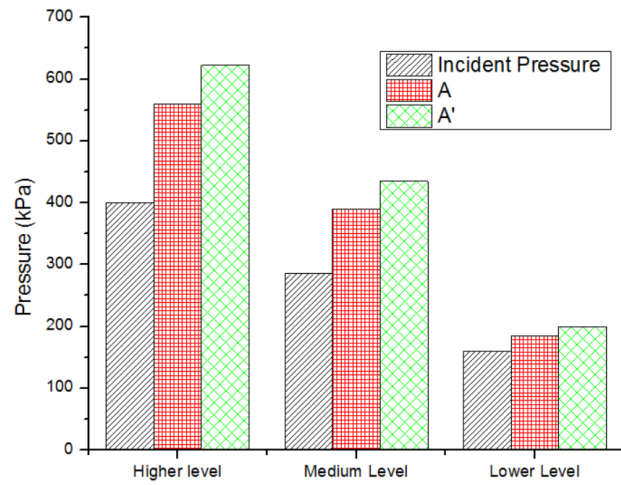
88

Figure 23 Comparison of the peak incident pressure and IOPs at the actual sensor location (A) and an assumed near front location (A') for frontal region at the three levels of blast.
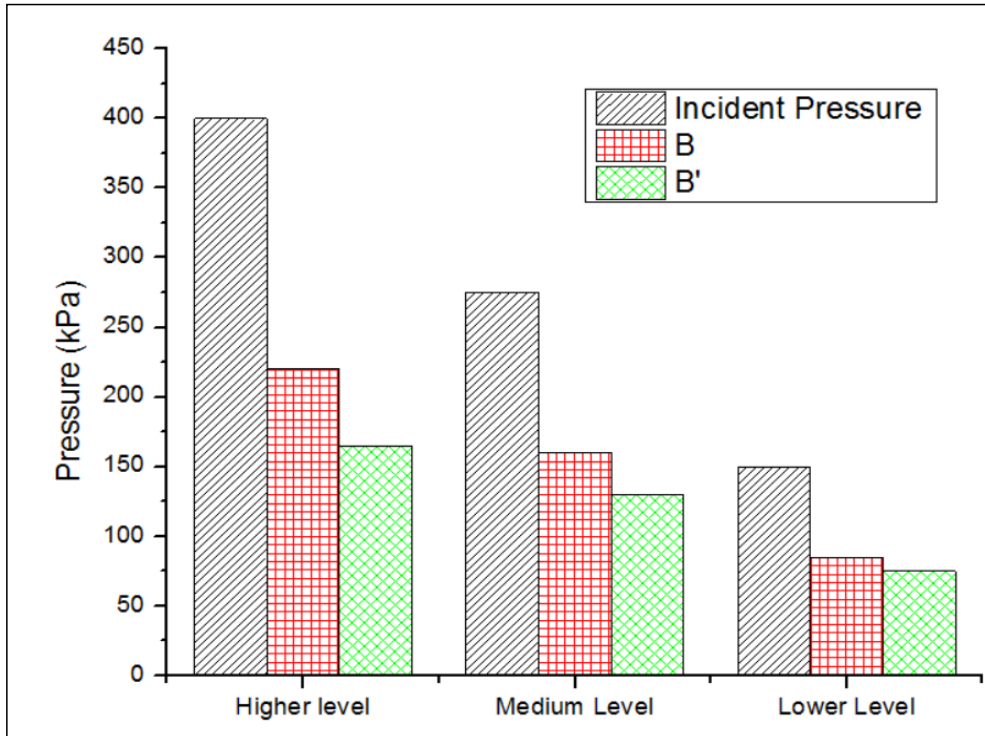
Figure 24. Comparison of the peak incident pressure and ICPs at the actual sensor location (B) and an assumed far rear end location (B') for occipital region at the three levels of blast

Also, the average element size for the current pig brain mesh is around 1.2 mm, whereas another study [15] has shown that 1 mm element size is necessary to resolve the transient waves seen in a sagittal brain model. In a full 3-D model, maintaining element size of 1 mm for hexahedral elements requires fine resolution scans. Additionally, it ends up having a higher number of elements in the model with such smaller element sizes. Despite the difference between the size for current 3-D model and aforementioned sagittal brain model, we believe that our model represents a reasonable approximation of the pig head, based on the similarity between the measured and simulated pressure wave forms.

5.   Conclusions

To conclude, a finite element model of the head of a 55-kg Yucatan pig was developed to simulate the biomechanical responses of the pig brain in an open field blast environment. Simulation results showed that the main characteristics, such as the peak

pressure and overall duration were replicated with the help of a 2-D to 3-D mapping technique using an MMALE formulation. The percentage differences in terms of the peak incident pressure between the experimental and the simulation results were found to be less than 2.2%. Further, the interaction between the shock wave and the pig head can be simulated with the help of a coupling algorithm available in a non-linear explicit FE code LS-DYNA. The measured peak pressure values at three levels of incident blast pressure magnitudes (low, medium, and high) were compared with the intracranial pressure values obtained from the simulations at the similar sensor locations. Reasonable agreements were found between the experimental and numerical results for the initial peak values, except at the frontal location. Results from the simulations showed a higher peak pressure at that location than the measured values. One possible reason might be related to air bubbles entrapped within the frontal fluid filled sinus cavity adjacent to the frontal ICP sensor. This argument is further supported by the parametric study using numerical models with holes at that location by removing some elements. In all simulations, it was found that the numerical technique stated above is capable of predicting the peak pressure with reasonable accuracy. Although the exponential decay is well simulated by the numerical model, some variations in the pressure magnitude during the decay phase seen in experiments could not be simulated well in the current study. Further studies will be aimed at correlating different biomechanical responses from the validated FE model with histological results, when they become available.

References for Task III

1. Chafi, M., Karami, G., Ziejewski, M.: Biomechanical assessment of brain dynamic responses due to blast pressure waves. Annals of biomedical engineering **38**(2), 490-504 (2010).
2. Moore, D.F., Jérusalem, A., Nyein, M., Noels, L., Jaffee, M.S., Radovitzky, R.A.: Computational biology—modeling of primary blast effects on the central nervous system. Neuroimage **47**, T10-T20 (2009).
3. Taylor, P.A., Ford, C.C.: Simulation of blast-induced early-time intracranial wave physics leading to traumatic brain injury. Journal of biomechanical engineering **131**(6), 061007 (2009).
4. Sundaramurthy, A., Alai, A., Ganpule, S., Holmberg, A., Plougonven, E., Chandra, N.: Blast-induced biomechanical loading of the rat: an experimental and anatomically accurate computational blast injury model. Journal of neurotrauma **29**(13), 2352-2364 (2012).
5. Nahum, A.M., Smith, R., Ward, C.C.: Intracranial pressure dynamics during head impact. In. SAE Technical Paper, No. 770922, (1977)
6. Hardy, W.N., Foster, C.D., Mason, M.J., Yang, K.H., King, A.I., Tashman, S.: Investigation of Head Injury Mechanisms Using Neutral Density Technology and High-Speed Biplanar X-ray. Stapp Car Crash Journal **45**, 337-368 (2001).
7. Zhu, F., Mao, H., Leonardi, A.D.C., Wagner, C., Chou, C., Jin, X., Bir, C., VandeVord, P., Yang, K.H., King, A.I.: Development of an FE model of the rat head subjected to air shock loading. Stapp car crash journal **54**, 211 (2010).

8. Zhu, F., Skelton, P., Chou, C.C., Mao, H., Yang, K.H., King, A.I.: Biomechanical responses of a pig head under blast loading: a computational simulation. International journal for numerical methods in biomedical engineering **29**(3), 392-407 (2013).

9. Ganpule, S., Alai, A., Plougonven, E., Chandra, N.: Mechanics of blast loading on the head models in the study of traumatic brain injury using experimental and computational approaches. Biomechanics and modeling in mechanobiology **12**(3), 511-531 (2013).

10. Huang, Y.: Simulation of Blast on Porcine Head. (No. ARL-TR-7340). Army research lab Aberdeen proving ground MD weapons and materials research directorate. (2015)

11. Reneer, D.V., Hisel, R.D., Hoffman, J.M., Kryscio, R.J., Lusk, B.T., Geddes, J.W.: A multi-mode shock tube for investigation of blast-induced traumatic brain injury. Journal of neurotrauma **28**(1), 95-104 (2011).

12. Sundaramurthy, A., Chandra, N.: A parametric approach to shape field-relevant blast wave profiles in compressed-gas-driven shock tube. Frontiers in neurology **5,** page 253 (2014).

13. Chavko, M., Koller, W.A., Prusaczyk, W.K., McCarron, R.M.: Measurement of blast wave by a miniature fiber optic pressure transducer in the rat brain. Journal of neuroscience methods **159**(2), 277-281 (2007).

14. Sawyer, T.W., Wang, Y., Ritzel, D.V., Josey, T., Villanueva, M., Shei, Y., Nelson, P., Hennes, G., Weiss, T., Vair, C.: High-Fidelity Simulation of Primary Blast: Direct Effects on the Head. Journal of Neurotrauma 33.13 (2015): 1181-1193.

15. Singh, D., Cronin, D.S., Haladuick, T.N.: Head and brain response to blast using sagittal and transverse finite element models. International journal for numerical methods in biomedical engineering **30**(4), 470-489 (2014).

16. Bir, C.: Measuring Blast-Related Intracranial Pressure Within the Human Head. Grant number W81XWH-09-1-0498 for U.S. Army Medical Research and Materiel Command (2011)

17. Lockhart, P., Cronin, D., Williams, K., Ouellet, S.: Investigation of head response to blast loading. Journal of Trauma and Acute Care Surgery **70**(2), E29-E36 (2011).

18. Feng, K., Zhang, L., Jin, X., Chen, C., Kallakuri, S., Saif, T., Cavanaugh, J., King, A.: Biomechanical responses of the brain in swine subject to free-field blasts. Frontiers in neurology **7**:179 (2016).

19. De Rosa, M., Fama, F., Palleschi, V., Singh, D., Vaselli, M.: Derivation of the critical angle for Mach reflection for strong shock waves. Physical Review A **45**(8), 6130 (1992).

20. Shivanna, K.H., Tadepalli, S.C., Grosland, N.M.: Feature-based multiblock finite element mesh generation. Computer-Aided Design **42**(12), 1108-1116 (2010).

21. Arbogast, K., Prange, M., Meaney, D., Margulies, S.: Properties of cerebral gray and white matter undergoing large deformation. Proceedings of Center for Disease Control, 33-39 (1997).

22. Grujicic, M., Bell, W., Pandurangan, B., Glomski, P.: Fluid/structure interaction computational investigation of blast-wave mitigation efficacy of the advanced combat helmet. Journal of Materials Engineering and Performance **20**(6), 877-893 (2011).

23. Panzer, M.B., Myers, B.S., Capehart, B.P., Bass, C.R.: Development of a finite element model for blast brain injury and the effects of CSF cavitation. Annals of biomedical engineering **40**(7), 1530-1544 (2012).
24. Slavik, T.P.: A coupling of empirical explosive blast loads to ALE air domains in LS-DYNA®. In: IOP Conference Series: Materials Science and Engineering 2010, vol. 1, p. 012146. IOP Publishing
25. Tabatabaei, Z.S., Volz, J.S.: A comparison between three different blast methods in LS-DYNA: LBE, MM-ALE, Coupling of LBE and MM-ALE. Proceedings of 12th International LS-DYNA Users Conference 2012, under session Blast/Impact3.
26. Kalra, A., Zhu, F., Chen, C., Yang, K.H.: A computational modeling of the biomechanical response of pig head under blast loading.Proceedings of 17th U.S. National Congress on Theoretical and Applied Mechanics 2014, p. 808. Michigan State University
27. Jin, X., Zhu, F., Mao, H., Shen, M., Yang, K.H.: A comprehensive experimental study on material properties of human brain tissue. Journal of biomechanics **46**(16), 2795-2801 (2013).
28. Schmidt, V.: Comparative anatomy of the pig brain: an integrative magnetic resonance imaging (MRI) study of the porcine brain with special emphasis on the external morphology of the cerebral cortex. Dissertation in Justus-Liebig-Universität Gießen, ISBN number 978-3-8359-6246-0 (2015).
29. Cernak, I., Merkle, A.C., Koliatsos, V.E., Bilik, J.M., Luong, Q.T., Mahota, T.M., Xu, L., Slack, N., Windle, D., Ahmed, F.A.: The pathobiology of blast injuries and blast-induced neurotrauma as identified using a new experimental model of injury in mice. Neurobiology of disease **41**(2), 538-551 (2011).
30. King, A.I., Yang, K.H., Zhang, L., Hardy, W., Viano, D.C.: Is head injury caused by linear or angular acceleration. proceedings of IRCOBI conference 2003, pp. 1-12
31. Zhang, L., Yang, K.H., King, A.I.: A proposed injury threshold for mild traumatic brain injury. Journal of biomechanical engineering **126**(2), 226-236 (2004).

TASK IV REPORT

Task IV - Develop and validate a computer model of the human brain simulating the effects of a blast over-pressure

1.   Introduction

The FE models simulating cadaveric brain responses in open filed blast experiments were developed. To validate the model, intracranial pressures (ICP) predicted by the model were compared with experimental results measured from ICP sensors placed at various locations in the brain. The model predicted responses for each blast condition were matched to the peak values and time history response-corridors in the form of the average and standard deviation of the experimental data from the six cadavers. The model predicted brain strain in the brain along with strain rate and product of the strain and strain rate were analyzed to understand the potential underlying mechanisms for blast induced mild TBI. The effect of different head orientations with respect to the oncoming wave front on resulting brain responses were also assessed and compared.

2.   Methods

FE models of explosive, air and the head

To simulate open-field blast test conditions, a 3.6-kg (8-lb) spherical C4 charge (diameter of 90 mm) was modeled with a 4.86 kg of trinitrotoluene (TNT) equivalent. The FE meshes of the charge and the surrounding air with the adequate dimension for simulating the range of the standoff distances were developed. A non-reflecting symmetric boundary condition was applied to 1/4th of the TNT and air to save computational time (Figure 1). The air and TNT charge were modeled as ALE elements in the LS-Dyna explicit solver (LSTC, CA).

The previously developed Wayne State University Head Injury Model (WSUHIM) is a high resolution, anatomically detailed finite element model simulating a 50th percentile adult male head. The entire head model is made up of over 330,000 elements and uses 15 different material properties for various tissues of the head (Figure 2a). The head model has been validated rigorously against intracranial pressures and brain/skull relative displacement data from cadaveric blunt impact experiments (Zhang et al, 2001, Viano et al. 2005) as well as the ICP data from cadaveric blast experiments using a shock tube (Sharma 2011).

For the current project, the head model has been further improved. The major improvements included the development of a detailed eye model, the segregation of the 4 brain lobes, the refinement of the major cerebral structures, and the differentiation of the cerebellar white matter from the gray matter (Figure 2b-d).
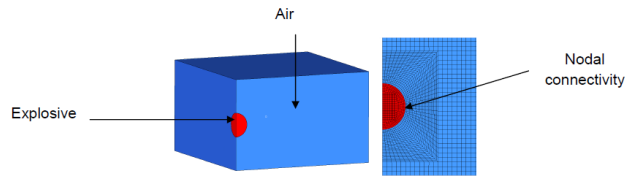
Figure 1: FE models of a sperical charge (8 lb of C4) and surrounding air.

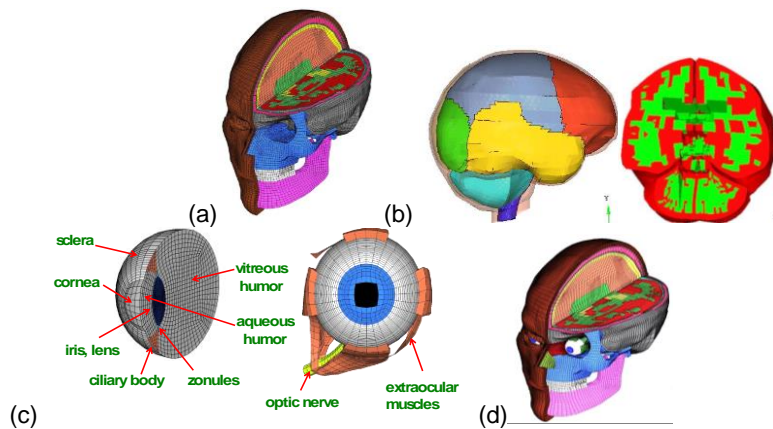

Figure 2: a) WSU Head Injury Model, b) segregation of the 4 lobes of the cerebrum (latral view) and differentiation of the gray and white matter in the cerebellum (coronal section), c) detailed eye model, d) integation of the eye model with the head model.

Simulation of open field blast experiment

To determine the model standoff distance at each of the three blast levels (high, medium and low), the incident overpressure (IOP) measured from a pencil probe placed next to the cadaver head was analyzed first (Figure 3). Figure 3 shows the average and 1 standard deviation (±SD) of IOP values measured from total 6 cadavers exposed to high, medium and low blast levels with the head oriented in forward, sideways and rearward directions to the wave front. Then, FE simulation of blast wave

propagation from the charge and air was performed to establish a relationship between the IOP level and the stand-off distance. As shown in Figure 4, the power function fitted very well to the data set (R^2 = 0.9986). Finally, the distance where IOP matched the average experimental value for each given blast level was used to position the head model (Table 1). Figure 5 shows the FE head model embedded in the air mesh for forward blast simulation. The blast wave propagation in air, interaction with the head model, and the subsequent structural response in the brain were simulated using the coupled multi- material Lagrangian–Eulerian, fluid-structural interface (FSI), and Lagrangian method in LS-DYNA 971 MPP R8.1 (LSTC, CA). The open-field blast simulation technique, method and algorithm were based on our previous blast simulation studies on human head and military helmet models (Zhang et al., 2013).

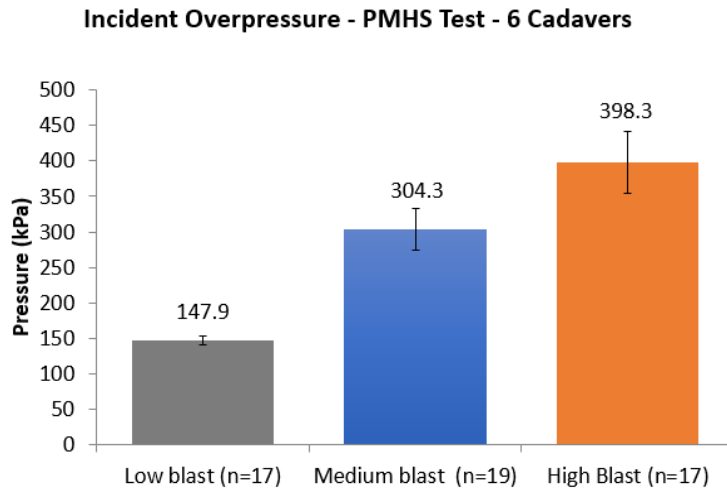**Incident Overpressure - PMHS Test - 6 Cadavers**

Figure 3: The IOP measurements from a pencil probe placed next to the 6 cadavers exposed to low, medium and high-level blasts.
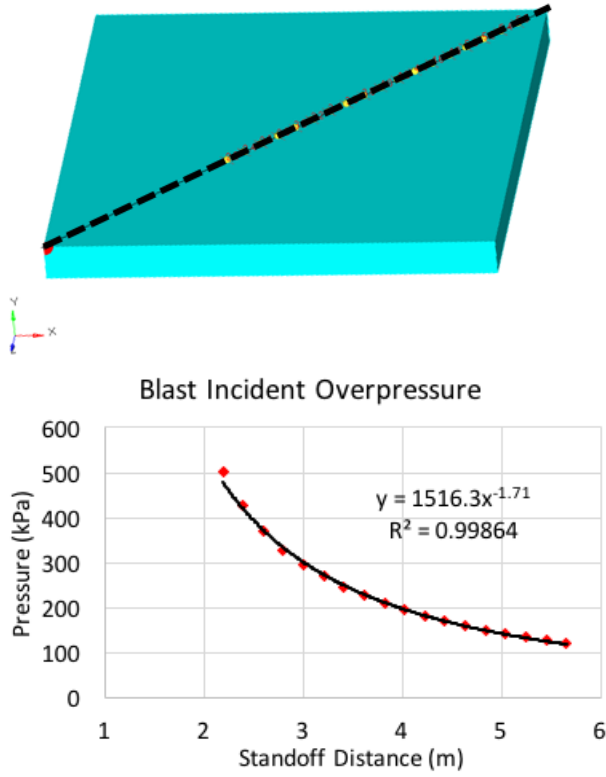
Figure 4: (a) The incident overpessure (side-on pressure) in air predicted along the wave direction at various locations from the center of the explosvie. (b) power function between the IOP and standoff distance

Table 1: The standoff distance where predicted model IOP matched experimental average IOP

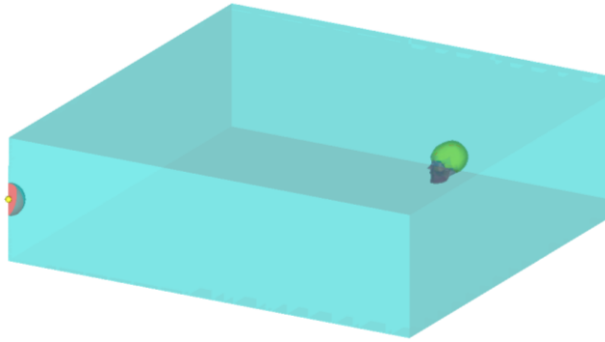| Blast Levels	Average Experimental IOP (kPa)	Standoff distance for FE model (m)
High	398 ± 43.2	2.5
Medium	304 ± 29.4	3.0
Low	148 ± 6.4	4.9

Figure 5: FE mesh of the TNT and air, and the head model embedded in the air mesh in forward blast condition

Material Properties used in the Model

The KELVIN-MAXWELL_VISCOELASTIC (MAT_61) material model in LS-Dyna was used to simulate viscoelastic behavior of the brain tissues under blast loading conditions. Based on the properties validated previously under blunt impact condition, the ICP rise time predicted by the model was much slower than that recorded from the ICP sensors. In order to match to the ICP sensor time-history profile including the peak ICP magnitude, the rise time and the total positive duration, the shear moduli of brain tissues and CSF were increased approximately one hundredfold relative to the values used for the blunt impact condition. The associated decay constant in shear modulus was reduced from 80 s^{-1} to 5 ms^{-1}. The final properties defined for the intracranial tissues are listed in Table 1. The skull bone was defined as an elastic-plastic material using a PIECEWISE LINEAR PLASTICITY (MAT_24) model. The properties were validated for blunt impact and were used in the blast model (see Table 2). The scalp/flesh was defined as a viscoelastic material with the shear moduli increased 20 times the values used under blunt impact conditions to simulate rate dependency of the viscoelastic materials at high rates of blast loading (Table 3).

Table 1. Properties of the viscoelastic materials defined for the brain tissues and CSF.

	Density (kg/mm^3)	Bulk modulus (GPa)	Short-term shear modulus (MPa)	Long-term shear modulus (MPa)	Decay constant (ms^{-1})
White matter	1.08e-6	2	1	0.15	5
Gray matter	1.02e-6	2	1.25	0.12	5
Brainstem	1.08e-6	2	1	0.24	5
Ventricles and CSF	1.02e-6	2	0.1	0.05	5

Table 2. Properties of the linear elastic-plastic material defined for the skull.

	Density (kg/mm^3)	Young's Modulus (GPa)	Poisson's ratio	Yield stress (GPa)	Tangent modulus (GPa)
Inner and outer table	2.2e-06	13.5	0.22	0.135	4.80
Diploe	1.2e-06	0.6	0.3	0.006	0.02

Table 3. Properties of the viscoelastic materials defined for the scalp and facial flesh

	Density (kg/mm^3)	Bulk modulus (GPa)	Short-term shear modulus (MPa)	Long-term shear modulus (MPa)	Decay constant (ms^{-1})
Scalp	1.6e-6	0.55	114	50	0.3

Analysis of ICP in the FE model

Intracranial pressures in the FE model were monitored and analyzed at various locations where ICPs were placed in the cadaver brain during the experiments. These ICP sensor locations were at the frontal, parietal, left temporal, right temporal, occipital and center regions of the brain. Figure 6 shows the element clusters defined to approximate the ICP sensors locations. The element clusters presenting the frontal, parietal, occipital and center ICP sensor locations were at the para-sagittal brain section, approximately 10-12 mm off the midline and 5-7 mm below the brain surface in the corresponding lobes or 10 cm below the surface in the center of the brain. The element cluster presenting the temporal sensor location was at 5-7 mm below the cortex at the temporal lobe. The responses from three elements at each region were averaged and compared to the ICP sensor readings.
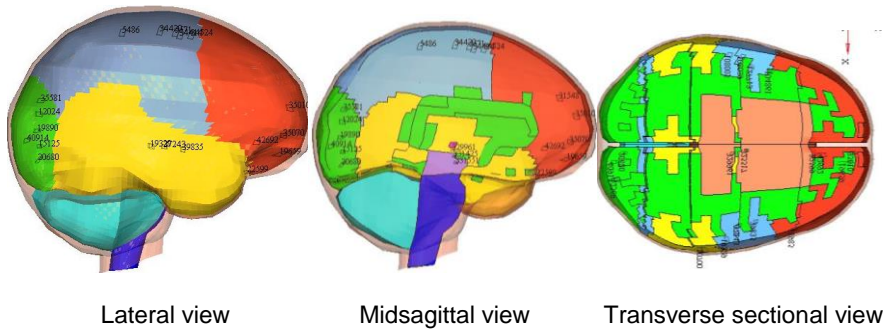
| Lateral view | Midsagittal view | Transverse sectional view |

Figure 6: The element clusters for ICP calcualtions approximate to the ICP sensor locations placed in the cadavers brain.

3.   Results

Experimental ICP corridors

To develop ICP-time history corridors for model validation, the test data from cadaver #3, 4, 5, and 6 out of a total of 6 cadavers were used. The data from the first two cadavers were excluded because the CSF and cerebral vasculature system of the specimens were either not pressurized or the pressure was not maintained throughout the tests. All ICP sensor data were filtered with SAE 10 kHz filter. Figure 7 shows the ICP values measured from the sensors in the frontal region for all four cadavers exposed to forward, sideways and rearward blast at the high IOP level. The peak ICP varied among the cadavers but the duration of positive pressure did not vary much for frontal blasts. Figure 7b shows the ICP values in the temporal region of the brain exposed to high level sideways blasts. The ICP response in terms of peak and duration from cadaver #4 deviated from the responses of the other three cadavers. To develop the corridors for the experimental data, the ICP rise times from all cadavers were aligned first. Then the average values along with standard deviation were calculated. Figure 8 shows an ICP corridor made up by the average+1sd and the average-1sd curves, representing the upper bound and lower bounds of the average ICP response, respectively in the coup regions (frontal for forward blast, temporal for sideways blast and occipital for rearward blast) due to high intensity blasts.
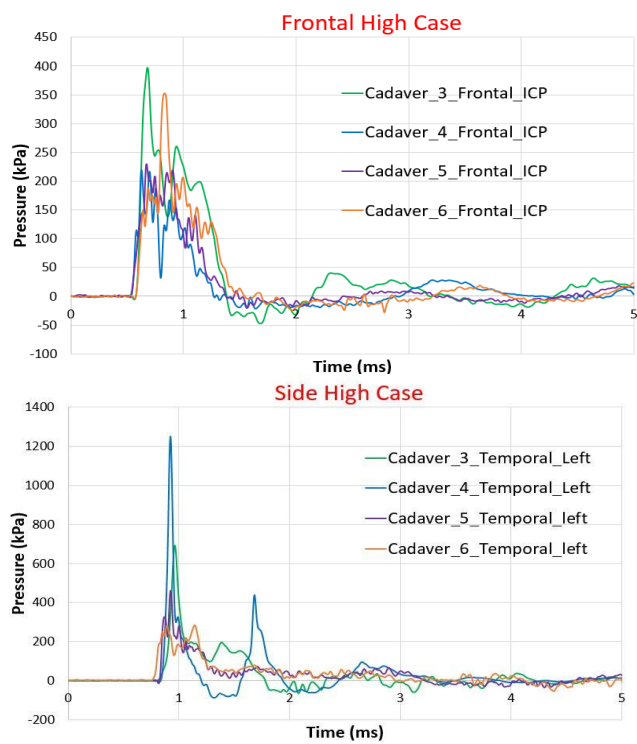
Figure 7: ICP measured from ICP sensors placed in the frontal and temporal brain regions from four cadavers due to high IOP exposure level
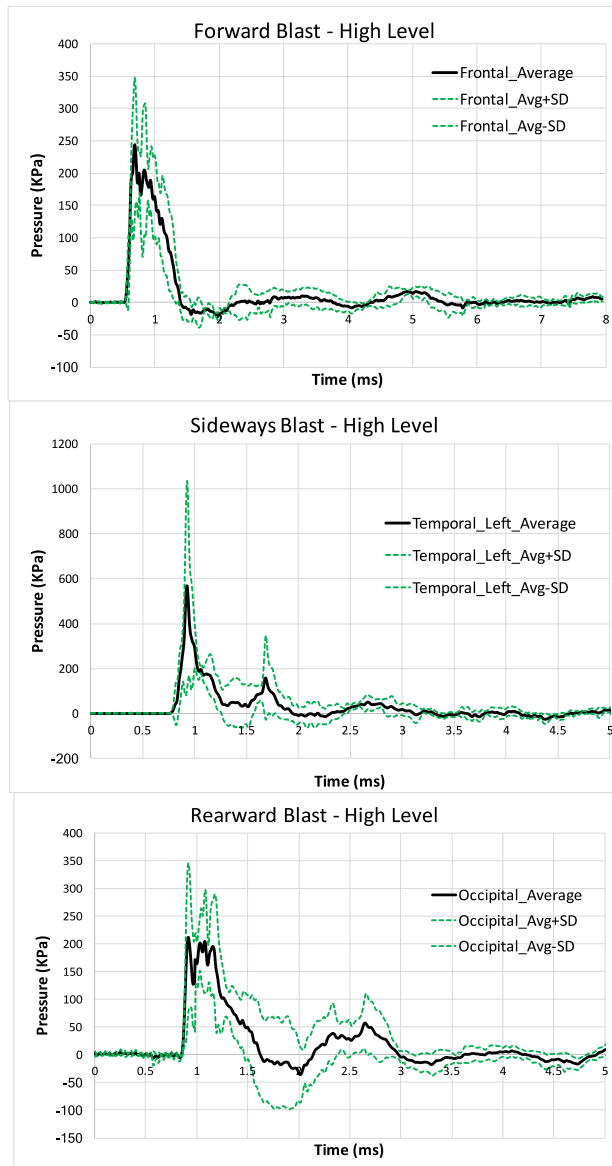
Figure 8: The ICP corridors of experimental data made up by the average+1 SD and average-1 SD curves, representing the upper and lower bounds of the average ICP, respectively in the coup regions for three blast directions at high intensity.

102

ICP Validation

Comparison of peak ICP

Figure 9 shows the comparison of the model predicted ICP responses at 6 locations from 9 blast conditions (three blast levels, three head orientations) to the experimental ICP response corridors. The FE model results fell within the range of the experimental values (average±1 SD) for most of the locations in all cases. The FE model overpredicted the ICP response at the coup sites, for the low-pressure level tests. That is, the predicted pressures were higher than the measured values at the frontal site for frontal blasts, at the lateral location facing the blast for sideways blasts and in the rear location for rear blasts. There was also some overprediction by the model at the contrecoup sites. This was likely due to the separation of the brain from the skull at the contrecoup site in the cadaver. Comparing the coup ICPs between the forward and sideways blast with comparable peak IOP values (428±17 vs. 428±46kPa), the sideways blasts produced a relatively higher pressure than the forward blast in the model consistent with experimental data. However, significant variation of ICP readings among cadavers was observed in sideways experiments.

Temporal response of ICP
In addition to the peak ICP validation, temporal responses of the model ICP at each sensor location were compared to the ICP corridors developed from the experimental data. The correlation from high blast level cases for forward and sideway blasts are shown in Figures 10 and 11. A frontal blast case is used as an example here to describe analysis and correlation

Figure 10 shows the model predicted ICP in the frontal, parietal, occipital and center locations against the experimental corridors due to frontal blast at an IOP of 398 kPa. The frontal ICP (coup site) response pattern fell reasonably well within the corridor. In the parietal and central brain regions, the duration of the positive ICP response lasted about 0.5 ms longer than the experimental data though the peak values were comparable. For the ICP response at the contrecoup site (occipital), the model predicted a higher peak negative pressure and a longer duration than the cadaver data. The overall comparison revealed that pressure rise rate was slower in the model than in the experimental data. The pressure rate calculated from average experimental ICP value and averaged over all sensor locations was approximately 2,200 Pa/s which was 2-3 times higher than the model responses. This may imply that the modeled brain tissue has greater damping effect than the cadaver brain tissue. Although, the shear properties of the brain were increased 100 times to account for the rate dependent effect of the viscoelastic materials, much stiffer properties may be required to properly simulate brain responses at blast loading rates. Other potential factors that may affect ICP measurement include the improper sealing of the ICP sensors at the skull and the presence of air bubbles around the sensor.
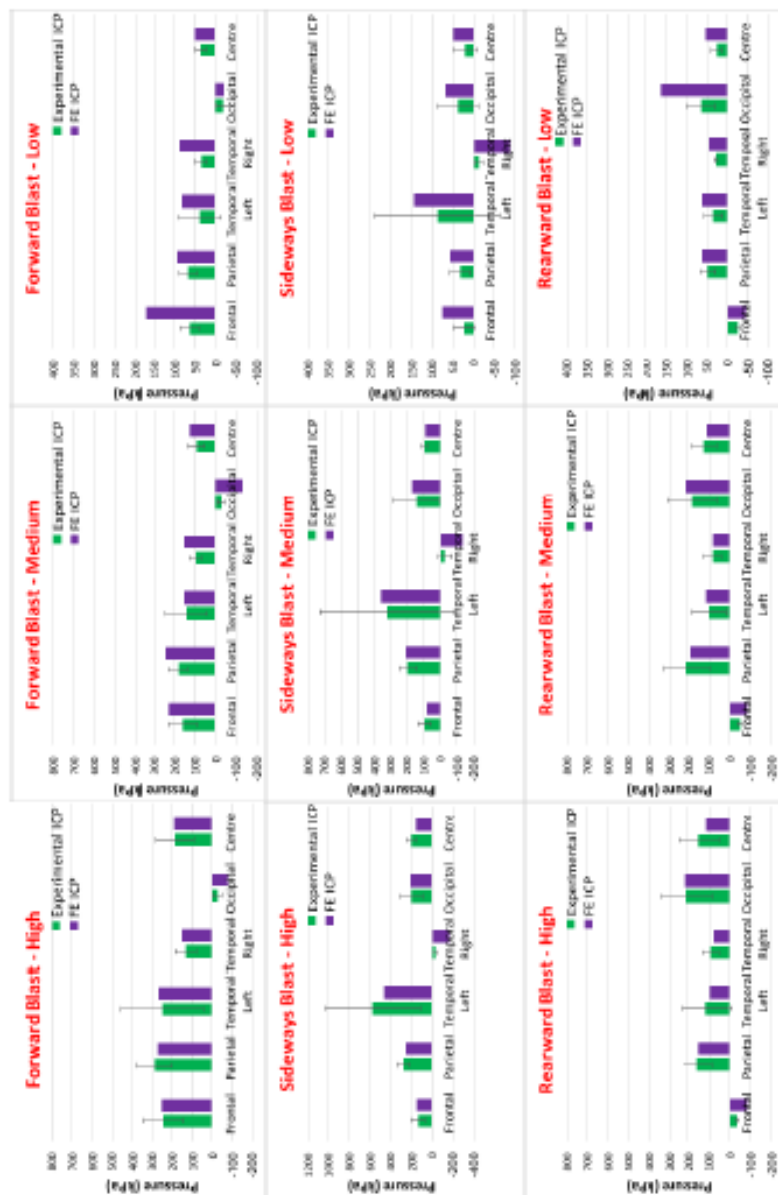
Figure 9: Comparison of the peak ICP predicted by the model to the peak ICP measured at various locations in the cadaver's brains
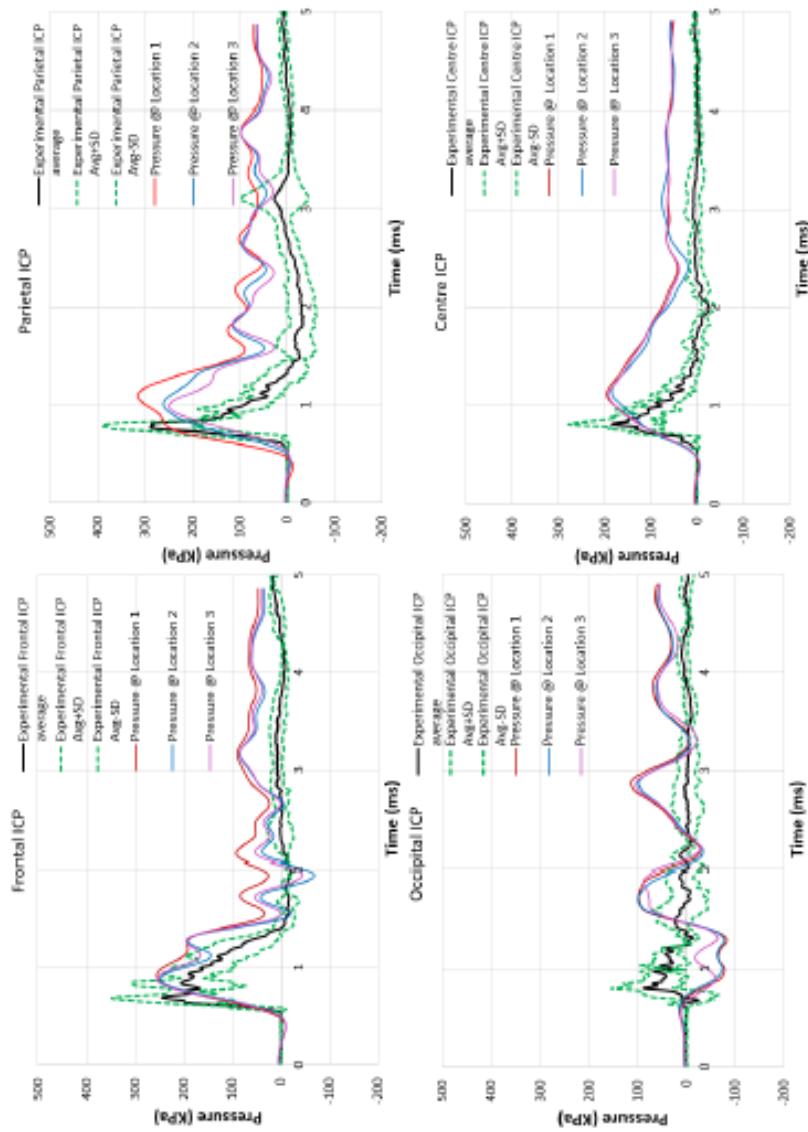
Figure 10: Forward blast the model-predicted ICP in comparsion with ICP corridors at various brain locations
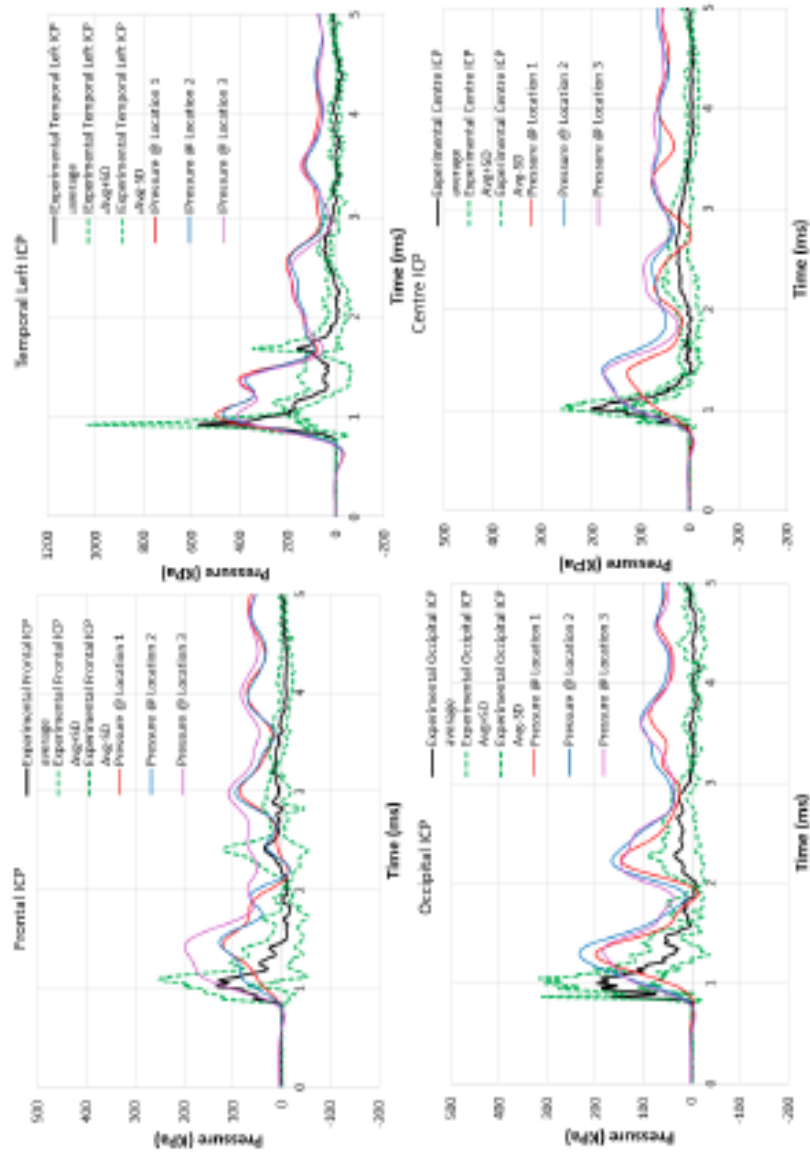
105

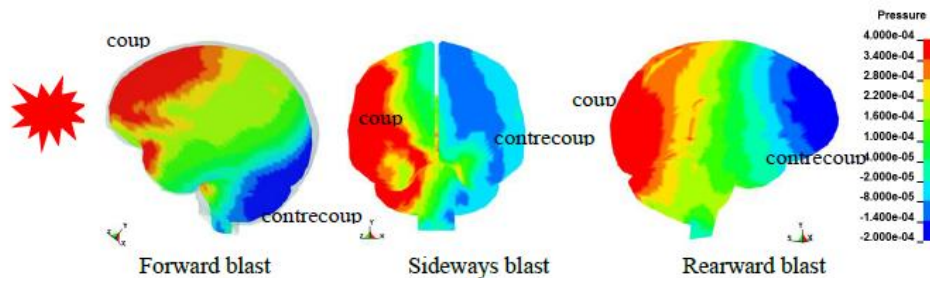Figure 11: Sideways blast the model-predicted ICP in comparsion with ICP corridors at various brain locations

Figure 12: The ICP response contour in the brain at the time when the ICP peaked

Model predicted brain strain and strain rate responses

High maximum principal strains (MPS) were predicted in the corpus callosum and midbrain or pons-medulla junction of the brain stem region (Figure 13a). This strain pattern differed from the ICP distribution pattern in the brains. The highest MPS was in the corpus callosum followed by the brainstem with peak values between 3 and 5% for all three loading directions. As for the time to peak for the MPS (Figure 13b), the MPS lagged behind the peak ICP time by approximately 4 ms. The strain delay was presumably related to the viscoelastic behavior of the brain tissue.
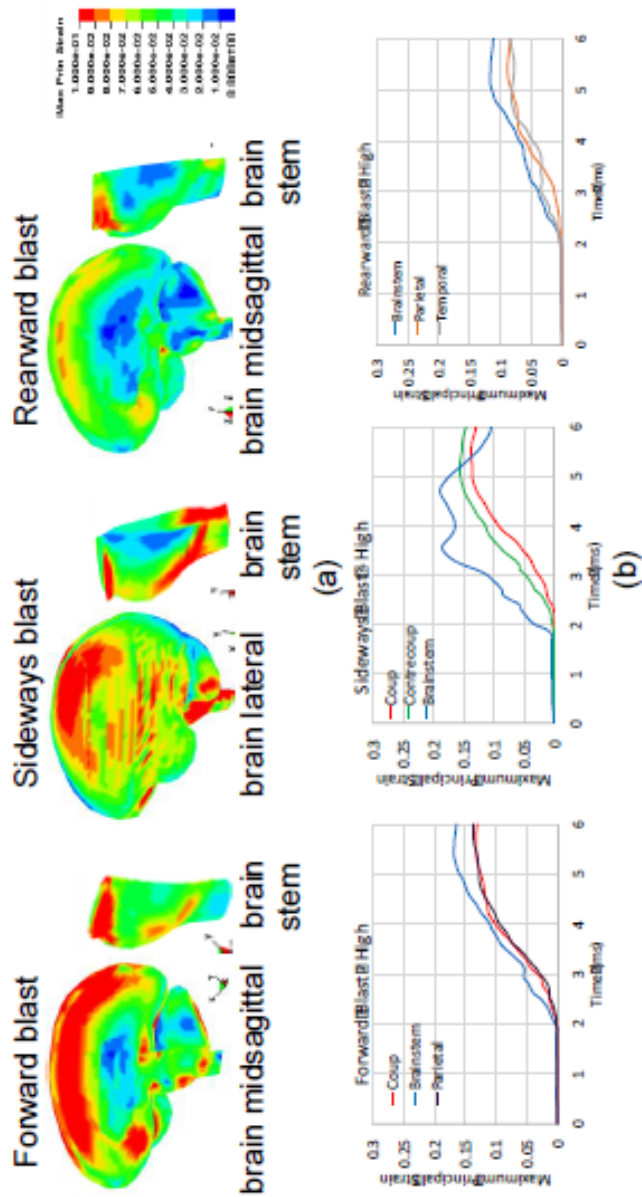
Figure 13: (a) Maximum principal strain contour in the brain at peaking time, (b) Maximum principal strain time histories
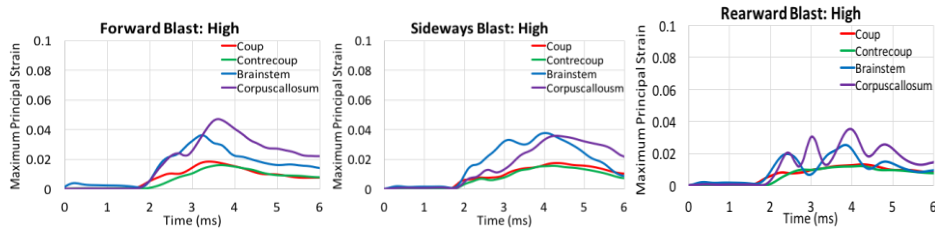
Figure 13: (b) Maximum principal strain time histories

Product of strain and strain Rate

The maximum principal strain rate (MPSR) is defined as the time derivative of the MPS history. The product of MPS and MPSR was also calculated. Table 4 summarizes the peak values of the MPS, MPSR and the product of MPS and MPSR predicted for the regions with high strain responses. The corpus callosum MPSR was the highest from rearward blast followed by sideways blast. The brainstem MPSR was the highest due to frontal blast followed by rearward blast. The highest MPS x MPSR was found in the corpus callosum due to frontal or rearward blasts. The overall high strain rate ranged from 27 to 86 1/s. The overall high product of strain and strain rate ranged from 0.6 to 1.6 1/s.

Table 4: High peak strain, strain rate and product of strain and strain rate

	Forward		Sideways		Rearward	
	Corpus callosum	Brainstem	Corpus callosum	Brainstem	Corpus callosum	Brainstem
MPS (.)	0.05	0.04	0.04	0.04	0.04	0.03
MPSR (1/s)	46	48	48	27	86	39
MPS x MPSR (1/s)	1.6	0.8	0.8	0.7	1.5	0.6

4.   Discussion

Overall, the model predicted a decrease in ICP as the pressure wave propagates across the brain. The pressure becomes negative (below the atmospheric pressure) at the contrecoup site. ICP sensor data from cadaver tests did confirm the existence of the pressure gradient and the coup-contrecoup phenomenon, the common brain injury mechanism often seen in blunt impact injuries. The model predicted peak ICP fell well within the range of the test data at most locations, except at the contrecoup site where negative pressure was overpredicted. The difference in contrecoup pressure may be attributable to the difference in coupling strength at the skull/brain interface between the model and cadaver. The cadavers (No. 4-6) were perfused to the normal ICP to simulate *in-vivo* condition and to assure brain-skull coupling. However, the fluid leakage observed during tests could decrease brain perfusion pressure level and

thereby cause a reduced coupling strength at the brain-skull interface. As a result, a reduced or even an absence of negative pressures could be expected in the cadaver brain in response to the dynamic pressure. In fact, the absence of the negative pressure was observed in a few cases from a few cadavers.

To simulate the cadaver brain at a reduced perfusion level, the bulk modulus of brain was reduced 100 times from 2 GPa to 20 MPa. We observed a reduced ICP magnitude but not a sufficient decrease in negative pressure. Currently, we are investigating the effect of a gap between the skull and brain on the pressure response to directly simulate the decoupling of an under-pressurized cadaver brain.

We observed a slower rise of the ICP in the model than the experimental data. This rate of ICP rise was likely associated with the damping effect of the viscoelastic properties of the brain which were valid for blunt impact conditions and at low blast overpressures (<100 kPa) generated from a shock tube. To account for rate dependent behaviors of brain tissue, the shear moduli defined in the original head model was increased by 100 times from 10 kPa to 1 MPa to simulate high rate open field blast loading. We observed a steeper ICP slope in the model and an improved model correlation to the experimental data in the coup region. However, the increase in rise rate of ICP in regions remote from the coup site was insufficient and still deviated from the experimental data. It was also noted the increase of brain shear moduli significantly reduced brain strain by 50%. The strain rate predicted by the current model ranged from 27 to 86 s^{-1}. For comparison, the strain-related injury data predicted by our finite element model for blunt impact is shown in Table 5 below:

Table 5. Predicted brain tolerance due to blunt impact
(Taken from Zhang et al, 2001)

BRAIN TOLERANCE FOR BLUNT IMPACT			
Predictor N= 58	Tolerance Levels for Probability of MTBI		
	25%	50%	75%
ε_{max}	0.29	0.40	0.48
$d\varepsilon/dt_{max}$ (s^{-1})	51	65	81
$\varepsilon \bullet d\varepsilon/dt_{max}$ (s^{-1})	20	24	27
Ar	63	81	99
Rr	4267	5488	6709
SI	178	298	417
HIC	143	240	336

By way of explanation, Table 5 was developed to study which of the injury parameters were the best predictors of mTBI due to blunt impact (in American football). It was found that the product of MPS and MPSR was the best predictor followed by strain rate. For blast-related impacts, strain and its derivatives do not play a part as a cause for injury because the blast duration is short and there is hardly any head motion.

Further investigation into the effect of the brain shear moduli on the resulting ICP, brain strain and strain rate along with the experimentally determined material behaviors of the brain tissue under blast loading (>500 s^{-1}) are required to improve model validation. Future work should translate the tissue level thresholds developed by the FE animal model with correlation to neurophysiopathological change following blast exposure to the human head model to improve the capability of the human model for predicting blast induced TBI.

5.   Conclusions

- The FE models incorporating a hybrid Lagrangian–Eulerian algorithm approach appeared to be useful tools for simulating blast wave phenomena, the interaction of the blast wave with the head and the subsequent internal brain responses to open-field blast loading.
- The model predicted an ICP gradient due to pressure wave propagation across the brain. It also predicted a negative pressure (below the atmospheric pressure) at the contrecoup site. The model predicted coup and contrecoup phenomena were consistent with the experimental measurements in various blast directions. The current FE model demonstrated a reasonable capability of predicting realistic pressure patterns as recoded by the sensor measurements.
- The simulated ICP results at five locations fell well within the average (±1 SD) of the peak ICP data measured by the sensors at corresponding locations in the cadaver brain for all three blast directions (forward, sideways and rearward) and three blast overpressure levels (high, medium and low).
- The model overpredicted ICP responses at the contrecoup site. The incomplete perfusion or leakage of the fluid in cadaver brain pressurization preparation may be responsible for low contrecoup pressure measured experimentally.
- The highest ICP was at the coup site (front for forward, temporal for sideways and occipital for rearward blast) with sideways blasts producing the highest ICP (470 kPa from the high blast level)
- The midbrain and pons-medulla junction of the brainstem experienced the highest maximum principal strain from all three blast directions.
- The highest predicted strain rate was 160 s^{-1} and the highest product of strain and strain rate was 21 s^{-1}.

111

Publications

Since the blast testing of cadavers was completed shortly before the end of the contract, we were only able to use the acquired cadaver data to validate the model. We have just started preparing a manuscript for journal publication. The paper will acknowledge the support of MRMC

References for Task IV

Sharma S and Zhang L. Biomechanical analysis of blast induced traumatic brain injury – A finite element modeling and validation study of blast effects on human brain. MS Thesis 2011. Wayne State University.

Viano DC, Casson IR, Pellman EJ, Zhang L, Yang KH, King AI. Concussion in professional football: Brain responses by finite element analysis - Part 9. Neurosurgery 2005;57(5):891-916.

Zhang L, Yang KH, Dwarampudi R, Omori K, Li T, Chang K, Hardy WN, Khalil TB, King AI. Recent advances in brain injury research: A new human head model development and validation. Stapp Car Crash J 2001;45:369-393.

Zhang L, Makwana R, Sharma S. Brain response to primary blast wave using validated finite element models of human head and advanced combat helmet. Frontier in Neurology 2013; 4:88. doi: 10.3389/fneur.2013.00088.

DISCUSSION AND CONCLUSIONS ON THE ENTIRE PROJECT

All objectives of the proposed research have been met. We completed all of the planned blast tests on swine and PMHS and have developed validated computer models of the pig and human brain subjected to blast overpressure

In terms of significant findings, we confirm from our swine study that blast overpressure indeed causes physical injury to the brain. The injury is not only limited to the white matter (axons) but is also seen in the gray matter (neurons). Other evidence of injury includes the proliferation of astrocytes In terms of the pressure threshold for injury, it appears that injury would occur at peak pressure levels of about 300 kPa (44.6 psi) in the swine. Human thresholds are as yet unknown but the 300 kPa level can be used as a guide.

The blast tests in this study were carried out in the open, as opposed to using a shock tube. These tests are a more realistic simulation of what happens in the field. In fact, there is a major difference between open field testing and shock tube testing. The duration of the blast is much shorter in the open field (3-5 ms) compared to that in a shock tube (>10 ms). The injury data and the biomechanical response data from shock tube testing is open to question. Furthermore, there are multiple reflected waves in shock tube testing that can also affect brain response and brain injury.

The computer model of the swine brain predicted very low strain levels as a result of the blast. This means that the observed injuries to both the gray and white matter were due to the transient pressure wave passing through the brain. That is, the brain cells are sensitive to pressure and are damaged by it. This result has significant implications in terms of interpreting the mechanisms of injury to the brain. Currently, most researchers believe that diffuse axonal injury in the brain is due to rotation of the head which causes the axons to stretch and break. That is, the retraction balls seen in injured axons were due to the high strains sustained by the axons. Now that we see axonal injury in brains exposed to blast overpressure and not subjected to large strains, we may have to reconsider the hypothesis of axonal disruption due to stretching and perhaps look into the breakdown of axons and neurons as a result of pressure waves This is not to say that the stretch mechanism does not play a role in axonal injury but that pressure can also be responsible for axonal and neuronal injury. One way to confirm this finding is to subject isolated brain cells to blast overpressure without applying any other kind of loading to them.

Our histological study is an ambitious attempt to study the entire porcine brain. This has never been done before for swine brains subjected to blast. We have already published a paper on the histological results for the frontal brain and have completed reviewing the slides of the midbrain. We are using volunteer students to read the slides since funding has already run out. We plan to publish our additional histological findings when the results have been analyzed.

We have arrived at the following conclusions:

1. Blast overpressure at and above 300 kPa (peak) is capable of causing mild traumatic brain injury to swine, based on our histological studies of the frontal brain. We found β-APP reactive zones in both the gray and white matter and proliferation of astrocytes and microglia.

2. There is confirmatory data from our quantitative electroencephalograph (qEEG) study that we see EEG evidence of brain injury almost immediately after the brain was exposed to blast overpressure.

3. Injury occurs in both the gray and white matter of the porcine brain and is likely due to the dynamic pressure pulse because the computed strains in brain were less than 3% while the estimated injury level due to strain is about 20%

4. Computed maximum brain strains due to blast, based on both the swine brain model and the human brain model, were found to be on the order of 5%. This level of strain is well below the injury level, based on what we know about brain strain is blunt impact.

5. Axonal injury in blast-exposed swine brain that is only subjected to very low strains requires reconsideration of the hypothesis that axonal stretch is the sole cause of diffuse axonal injury. Additional studies are recommended to determine the effect of pressure on brain cells, such as exposing isolated brain cells to blast.

6. Open field blasts have a much shorter duration that that in a shock tube and is thus a more realistic simulation of blast. Longer duration blasts can cause more severe injuries to the brain and the results of shock tube studies are open to question.

7. We have developed and partially validated computer models for both the swine and human brain. The validation was based on comparing the measured and computed pressures in various regions of the brain. Such models can be used to predict the response of the brain to a variety of blast scenarios.

Publications Resulting from this Award

Journal Publications

Chen C, Zhou C, Cavanaugh JM, Kallakuri S, Desai A, Zhang L and King AI (2016) Quantitative electroencephalography analysis of blast induced brain injury in a swine model. Brain Injury. doi: 10.1080/02699052.2016.1216603.

Feng K, Zhang L, Jin X, Chen C, Kallakuri S, Saif T, Cavanaugh, J and King A (2016) Biomechanical responses of the brain in swine subject to free-field blasts. Frontiers in Neurology, 7: 179, doi: 10.3389/fneur.2016.00179.

Kallakuri S, Desai, A, Feng K, Tummala S, Saif T, Chen C, Zhang L, Cavanaugh JM, King AI (2017) Neuronal injury and glial changes are hallmarks of open field blast exposure in swine frontal lobe. PLoS ONE, 12(1) e0169239. doi:10.1371/journal.pone.0169239.

Kalra A, Zhu F, Saif T, Kallakuri S, Jin X, Yang K, King A (2017) Development and validation of a numerical model of the swine head subjected to open field blasts. Shock Waves (In press).

Jin X et al (2017) Response of the PMHS (cadaver) brain to open-field blast overpressure. Journal manuscript in preparation.

Zhang L et al. (2017) Validation of Finite Element Human Head Model for Predicting Brain Injury Risk in Open-field Blast Exposure. Journal manuscript in preparation

Zhu F, Chou CC, Yang KH and King AI (2015) Development of a new biomechanical indicator for primary blast-induced brain injury. Chinese Journal of Traumatology, 18:10-12.

Zhu F, Chou CC, Yang KH and King AI (2014) A theoretical analysis of stress wave propagation in the head under primary blast loading, Journal of Engineering in Medicine, 228:439-445.

Zhu F, Gatti DL, Yang, KH (2016) Nodal versus total axonal strain and the role of cholesterol in traumatic brain injury. Journal of Neurotrauma, 33.859-870.

Zhu F, Kalra A, Saif T, Yang Z, Yang KH and King AI (2016) Parametric analysis of the biomechanical response of head subjected to the primary blast loading – a data mining approach. Computer Methods in Biomechanics and Biomedical Engineering, 19:1053-1059.

Zhu F, Skelton P, Chou CC, Mao H, Yang KH and King AI (2013) Biomechanical responses of a pig head under blast loading: a computational simulation. International Journal for Numerical Methods in Biomedical Engineering, 29:392-407.

Other Publications

Cavanaugh JM, Feng K, Zhang, L, Kallakuri S, Chen C, King AI (2014) Mechanical response and brain injury in swine subjected to free-field blast. Proc. 7th World Congress of Biomechanics, Boston, MA.

Chen C, Zhou C, Cavanaugh JM, Kallakuri S, Desai A, Zhang L, King AI (2015) Quantitative electroencephalography analysis of blast induced brain injury in a swine model. Proc. BMES Conference, Tampa, FL.

Dave K, Sharma S, Mukharjee S, Zhang L. Development and Validation of A detailed Finite Element Model of Human Eye for Predicting Ocular Trauma (2017). Injury Biomechanics Symposium Ohio State University, Columbus, OH.

Feng K, Kallakuri S, Jin X, Desai, A Chen, C, Saif T, Zhang L, Cavanaugh JM, King AI (2016) Free-field blast induced changes in the gyrencephalic brain: A biomechanical and histological study. MHSRS Military Health System Research Symposium. Ft. Lauderdale, FL.

Feng K, Jin X, Saif T, Chen C, Zhang L, Cavanaugh J, King A (2016) Rapid acquisition of multi-channel biomechanical data due to open field blasts. Proc. IEEE DSP Conference, Beijing, China.

Feng K, Kallakuri S, Jin X, Desai A, Chen C, Saif T, Zhang L, Cavanaugh J, King A (2015) Free-field blast induced mechanical response, axonal injury and glial changes in swine. Proc. BMES Annual Meeting, Tampa, FL.

Feng K, Zhang L, Chen C, Kallakuri S, Jin X, Saif T, Cavanaugh J, King A (2015) Biomechanical Response of Swine Exposed to Open-Field Blasts. Military Health System Research Symposium (MHSRS), Ft, Lauderdale, FL.

Kallakuri S, Zhang L, Desai A, Mathei J, Dawe E, Feng K, Cavanaugh. J, King A (2015) Open Field Primary Blast Exposure Induces Neuronal and Glial Alterations in the Brain - a Preliminary Investigation of Swine Frontal Cortex. Military Health System Research Symposium (MHSRS), Ft. Lauderdale, FL.

Sharma S, Makawana, R (2015) Biomechanical responses of the human head/brain to free field blast Military Health System Research Symposium (MHSRS), Ft. Lauderdale, FL.

Zhang L, Cavanaugh JM, Feng K, Kallakuri S, Jin X, King A (2017) Brain Response to Free-Field Blast: A biomechanical, histological and computational modeling study. MHSRS Military Health System Research Symposium, Kissimmee, FL.